IEEE Access
Multidisciplinary | Rapid Review | Open Access Journal

Received December 17, 2021, accepted December 24, 2021, date of publication December 28, 2021,
date of current version January 7, 2022.

Digital Object Identifier 10.1109/ACCESS.2021.3139200

Novel Deterministic Detection and Estimation Algorithms for Colocated Multiple-Input Multiple-Output Radars

PASQUALE DI VIESTI, (Graduate Student Member, IEEE), ALESSANDRO DAVOLI, (Graduate Student Member, IEEE), GIORGIO GUERZONI, AND GIORGIO M. VITETTA, (Senior Member, IEEE)

Department of Engineering "Enzo Ferrari," University of Modena and Reggio Emilia, 41125 Modena, Italy
Consorzio Nazionale Interuniversitario per le Telecomunicazioni (CNIT), 43124 Parma, Italy

Corresponding author: Pasquale Di Viesti (pasquale.diviesti@unimore.it)

This work was supported in part by the Case New Holland (CNH) Industrial Italia S.p.A., and in part by CNH Industrial Belgium NV.
The technical content of this manuscript is patent pending.

ABSTRACT In this manuscript, the problem of detecting multiple targets and estimating their spatial coordinates (namely, their *range* and the *direction of arrival* of their electromagnetic echoes) in a *colocated multiple-input multiple-output* radar system operating in a static or slowly changing two-dimensional or three-dimensional propagation scenario is investigated. Various solutions, collectively called *range & angle serial cancellation algorithms*, are developed for both frequency modulated continuous wave radars and stepped frequency continuous wave radars. Moreover, specific technical problems experienced in their implementation are discussed. Finally, the accuracy achieved by these algorithms in the presence of multiple targets is assessed on the basis of both synthetically generated data and of the measurements acquired through three different multiple-input multiple-output radars and is compared with that provided by other methods based on multidimensional Fourier analysis and multiple signal classification.

INDEX TERMS MIMO, direction of arrival estimation, radar signal processing, frequency estimation.

I. INTRODUCTION

In the last years, the advances in millimeter-wave semiconductor technology and the development of novel signal processing techniques have lead the way to the exploitation of *multiple-input multiple-output* (MIMO) radar systems in a number of fields. These systems can be divided in *statistical* MIMO radars [1], [2] and *colocated* MIMO radars [3] on the basis of the distance between their transmit array and their receive array; in the first case, transmit and receive antennas are widely separated, whereas, in the second one, they are closely spaced and, in particular, they are usually placed on the same shield. In this paper, we focus on colocated MIMO radars only; such systems play an important role in a number of applications, because of their limited cost, their small size and their ability to detect the presence of multiple targets. The performance achieved by any colocated MIMO radar system depends not only on some important characteristics of its hardware (e.g., the operating frequency, the number of transmit and receive antennas, the configuration of the transmit and receive arrays, etc.), but also on the techniques employed in the generation of its radiated waveforms and in the processing of the measurements acquired through its receive array. As far as the last issue is concerned, it is worth stressing that *optimal* (i.e., *maximum likelihood*, ML) techniques for the estimation of the overall number of targets and of their spatial coordinates cannot be employed in practice, since they require solving complicated multidimensional optimization problems and, consequently, entail a huge computational effort, even in the presence of a small number of targets [4]. This has motivated the development of various *sub-optimal* estimation techniques able to achieve good estimation accuracy at a manageable computational cost. A well known sub-optimal technique employed in real world radar systems is the one described in ref. [5] for *frequency modulated continuous wave* (FMCW) radar systems; this requires: a) the computation of a multidimensional *Fast Fourier Transform* (FFT) of the matrix collecting the time-domain samples of the signals acquired through the receive array of the employed radar device; b) the search for the peaks of the

The associate editor coordinating the review of this manuscript and approving it for publication was Jiayi Zhang.

resulting amplitude spectrum over a range-azimuth-elevation domain or a range-azimuth domain in *three-dimensional* (3D) and *two-dimensional* (2D) imaging, respectively. Despite the practical importance of this technique, the computational effort it requires is still significant, since it involves multi-dimensional spectral analysis of the acquired signals. Moreover, it suffers from the following relevant drawback: it can miss targets whose electromagnetic echoes are weaker than those generated by other spatially close targets; this is due to the fact the spectral contribution due to weak echoes is usually hidden by the leakage originating from stronger echoes. This drawback may substantially affect the overall quality of radar imaging in the presence of extended targets, since such targets can be usually modelled as a cluster of point targets characterized by different radar cross sections [6].

Alternative sub-optimal techniques available in the technical literature are based on the idea of turning a complicated multidimensional optimization problem into a series of simpler and interconnected optimization sub-problems, each of which involves a search for the local maxima of a specific cost function over a limited *one-dimensional* (1D) or 2D parameter space. Examples of this approach are offered by [7] and [8], and by [9], where range-azimuth estimators for FMCW MIMO radars and for *stepped frequency continuous wave* (SFCW) MIMO radars, respectively, are derived. More specifically, on the one hand, target delays are first estimated by applying the *multiple signal classification* (MUSIC) algorithm to a temporal auto-correlation matrix or by identifying the beat frequencies in the downconverted received signal through spectral analysis (in particular, through the FFT algorithm) in [7] and in [8], respectively; then, the acquired information are exploited to estimate the *direction of arrival* (DOA) of the echoes originating from detected targets. On the other hand, a different approach is proposed in [9], where various *iterative deterministic methods* applicable to a 2D propagation scenario are derived. These methods have the following relevant features: 1) they process a single snapshot of the received signal (acquired over the whole antenna array); 2) they estimate a new target in each iteration; 3) they do not require prior knowledge of the overall number of targets; 4) they involve 1D or 2D maximizations only; 5) they achieve a good accuracy at a reasonable computational cost; 6) the computational effort they require can be easily controlled by setting a threshold on the maximum number of targets to be detected.

In this manuscript, six new detection and estimation algorithms for 2D and 3D radar imaging are developed. They represent different versions of the same algorithm, called *range & angle serial cancellation algorithm* (RASCA), and can be interpreted as embodiments of a general approach to target detection and estimation. In addition, they share some important features with the detection and estimation techniques developed in [8] and [9]. In fact, similarly as the techniques illustrated in [9], they are deterministic, process a single snapshot, operate in an iterative fashion and are computationally efficient; the last feature can be related to the fact they require the evaluation of 1D FFTs only and the search for the global maximum of proper cost functions over 1D (frequency, azimuth or elevation) domains. Moreover, similarly as [8], they first extract the range of each detected target from the spectra of the received signals and, then, fuse the information originating from such spectra to extract DOA information. In addition, they exploit the iterative estimation techniques developed in [10] and based on a serial cancellation approach for evaluating the parameters of multiple overlapped sinusoids or multiple overlapped complex exponentials in the presence of additive noise. The devised algorithms are able to accurately detect and estimate multiple close targets, and to solve the problem of *merged measurements* or *unresolved measurements* [11]–[14], in the sense that targets generating merged measurements in the range domain are resolved in the estimation of their angular coordinates.

The remaining part of this manuscript is organized as follows. In Section II, the architecture of colocated FMCW/SFCW MIMO radars and the models adopted in our work for representing their received signals are analysed. The general approach to target detection and estimation on which our algorithms are based is illustrated in Section III, whereas the algorithms themselves are described in Sections IV and V, which are devoted to FMCW and SFCW radars, respectively. Various important details about these algorithms are provided in Section VI, whereas some technical limitations encountered in their implementation in real world radar systems are discussed in Section VII. A description of other FFT-based and MUSIC-based detection and estimation algorithms with which our algorithms are compared is provided in Section VIII. The computational cost of all the considered algorithms is illustrated in Section IX, whereas their performance is analysed in Section X, where various numerical results, based on both synthetically generated data and experimental measurements, are illustrated. Finally, some conclusions are offered in Section XI.

II. SIGNAL AND SYSTEM MODELS

This section is devoted to: a) describing the architecture of colocated and bistatic MIMO radar systems operating in *time division multiplexing* (TDM) [4] and at millimeter waves; b) analysing the model of their received signals in the cases of FMCW and SFCW transmissions. The considered radar systems share the following important characteristics:

1) They are equipped with a *transmit* (TX) and a *receive* (RX) antenna array, consisting of N_T and N_R elements, respectively.
2) These arrays allow to radiate *orthogonal waveforms* from different antennas and to receive distinct replicas of the electromagnetic echoes generated by multiple targets; moreover, the *orthogonality* of the transmitted waveforms is achieved by radiating them through distinct TX antennas over disjoint time intervals.
3) Their TX and RX arrays are made of distinct antenna elements, placed at different positions. However,

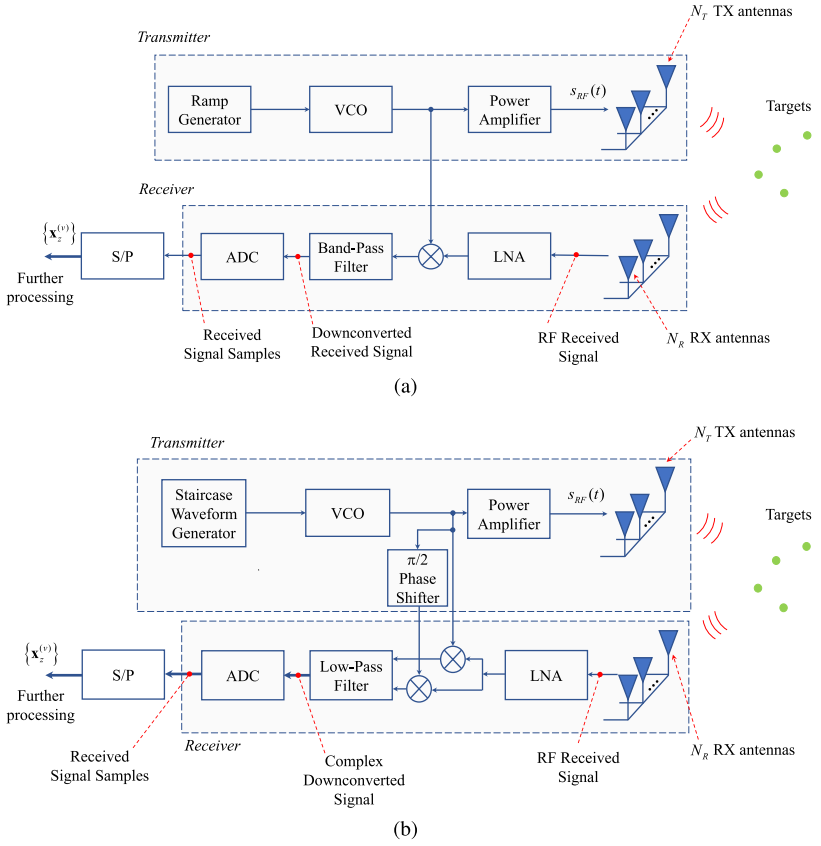

FIGURE 1. Transmitter (upper part) and receiver (lower part) of: a) a colocated MIMO FMCW radar system; b) a colocated MIMO SFCW radar system.

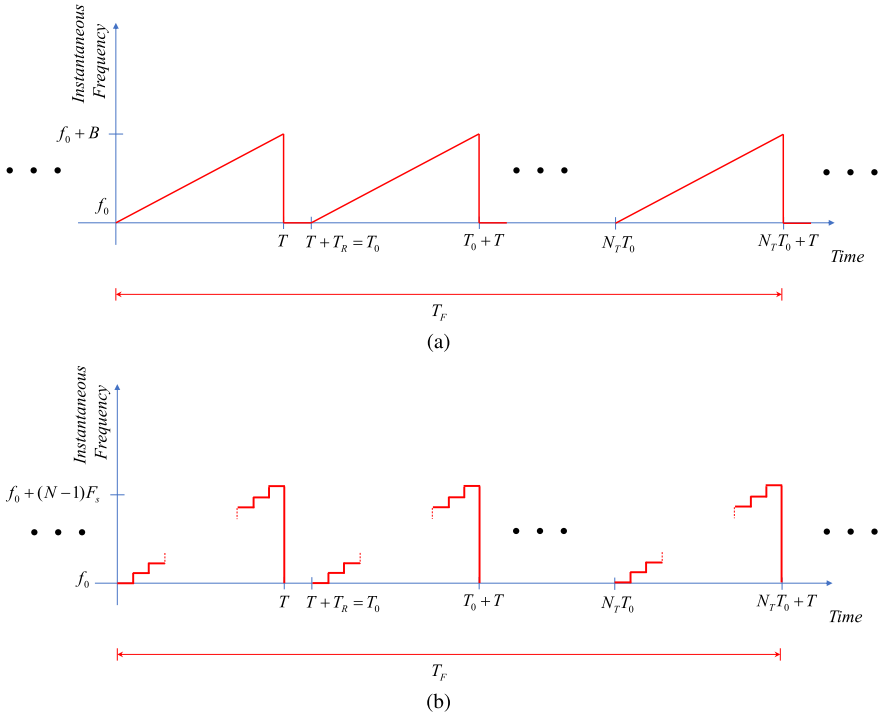

FIGURE 2. Representation of the instantaneous frequency of the RF signal generated by the VCO in: a) a FMCW radar system; b) a SFCW radar system.

TX antennas are close to the RX ones and, in particular, are usually placed on the same shield.

The architecture of the FMCW and SFCW radar systems which we always refer to in our work are illustrated in Figs. 1a and 1b, respectively. In both cases, the radar transmitter consists of a waveform generator feeding a *voltage controlled oscillator* (VCO), whose output signal is radiated by the TX array after power amplification. The radiated signal is reflected by multiple targets, whose echoes contribute to the signals acquired through the RX array; each received signal feeds a *low noise amplifier* (LNA), whose output undergoes downconversion, filtering and analog-to-digital conversion. Finally, the resulting stream of signal samples (i.e., of raw data) is processed for target detection and estimation.

Our derivation of the received signal model for the radar systems shown in Figs. 1a and 1b relies on the following assumptions:

a) The radar operates in a static or slowly time varying propagation environment.

b) The signal radiated by the radar transmitter is reflected by L *static point targets*, so that the useful part of the received signal consists of the superposition of L components, each originating from a distinct target.

c) All the TX and RX antennas belong to the same planar shield, so that a two-dimensional reference system lying on the physical antenna array can be defined.

d) Any couple of *physical* TX and RX antennas of the considered bistatic radar is replaced by a single *virtual antenna* of an equivalent *monostatic radar*. The abscissa x_v and the ordinate y_v of the v-th *virtual antenna* (VA) element associated with the p-th TX antenna and the q-th RX antenna (briefly, the (p, q) VA) are computed as[1]

$$x_v = \frac{x_p + x_q}{2} \tag{1}$$

and

$$y_v = \frac{y_p + y_q}{2}, \tag{2}$$

respectively, with $p = 0, 1, \ldots, N_T - 1$, $q = 0, 1, \ldots, N_R - 1$ and $v = 0, 1, \ldots, N_{\mathrm{VR}} - 1$; here, (x_p, y_p) ((x_q, y_q)) are the coordinates of the p-th TX (q -th RX) antenna and $N_{\mathrm{VR}} \triangleq N_T \cdot N_R$ represents the overall number of available VAs.

A. MIMO FMCW RADAR SYSTEM

Let us focus now on the FMCW radar shown in Fig. 1a. Its waveform generator produces a periodic sawtooth signal, so that the instantaneous frequency of the chirp frequency modulated signal available at the output of its VCO evolves periodically, as illustrated in Fig. 2a. In this figure, the parameters T, T_R and T_0 represent the *chirp interval*, the *reset time* and the *pulse period* (or *pulse repetition interval*), respectively [4], whereas the parameters f_0 and B are the *start frequency* and the *bandwidth*, respectively, of the transmitted signal. Note that, if all the available TX diversity is exploited and a time slot of T_0 s is assigned to each TX antenna, a single *transmission frame*, over which the transmission from the whole TX array is accomplished, lasts $T_F \triangleq N_T T_0$ s; in this interval, a single *snapshot* is acquired at the receive side. Let us focus now on a single chirp interval and, in particular, on the time interval $(0, T)$, and assume that, in that interval, the p-th TX antenna is employed by the considered radar system (with $p \in \{0, 1, \ldots, N_T - 1\}$); the signal radiated by that antenna can be expressed as

$$s_{RF}(t) = A_{RF}\, \Re\{s(t)\}, \tag{3}$$

where A_{RF} is its amplitude,

$$s(t) \triangleq \exp(j\theta(t)), \tag{4}$$

$$\theta(t) \triangleq 2\pi \left(f_0 t + \frac{\mu}{2} t^2\right) \tag{5}$$

and $\mu \triangleq B/T$ is the *chirp rate* (i.e., the steepness of the generated frequency chirp). It can be proved that, under the assumptions listed above, the n-th received signal sample acquired through the v-th VA element (with $v = 0, 1, \ldots, N_{\mathrm{VR}} - 1$) in the considered chirp interval is given by (e.g., see [16, Par. 4.6, eq. (4.27)])

$$\begin{aligned} x_{r,n}^{(v)} &= \sum_{l=0}^{L-1} a_l \cos\left(2\pi n F_l^{(v)} + \psi_l^{(v)}\right) + w_{r,n}^{(v)} \\ &= \sum_{l=0}^{L-1} \left[C_l^{(v)} \exp\left(j2\pi n F_l^{(v)}\right) \right. \\ &\qquad \left. + (C_l^{(v)})^* \exp\left(-j2\pi n F_l^{(v)}\right)\right] + w_{r,n}^{(v)}, \end{aligned} \tag{6}$$

with $n = 0, 1, \ldots, N - 1$; here, N is the overall number of samples acquired over each chirp period, a_l is the amplitude[2] of the l-th component of the useful signal,

$$C_l^{(v)} \triangleq \frac{1}{2} a_l \exp\left(j\psi_l^{(v)}\right) \tag{7}$$

represents the *complex amplitude* of the real tone appearing in the *right hand side* (RHS) of (6),

$$F_l^{(v)} \triangleq f_l^{(v)} T_s = f_l^{(v)} / f_s \tag{8}$$

is the normalised version of the frequency

$$f_l^{(v)} \triangleq \mu\, \tau_l^{(v)}, \tag{9}$$

[1] Note that this is not the only rule adopted in the technical literature to compute the coordinates of the (p, q) VA. For instance, in [15, Par. 4.3.1, pp. 159-161], the abscissa (ordinate) of this element is evaluated as $2x_v$ ($2y_v$), where x_v and y_v are expressed by (1) and (2), respectively. Keep in mind, however, that if the last rule is adopted, all the following formulas involving such coordinates must be changed accordingly.

[2] This amplitude quantifies the *radar cross section* (RCS) of the l-th target. It depends on both the range of this target and its reflectivity. Moreover, in this work, it is assumed to be independent of the virtual antenna index (i.e., of v), for simplicity.

characterizing the l-th target detected on the v-th virtual RX antenna, T_s (f_s) denotes the sampling period (frequency) of the employed *analog-to-digital converters* (ADCs),

$$\tau_l^{(v)} \triangleq \frac{2}{c}\left[R_l + x_v \cos(\phi_l)\sin(\theta_l) + y_v \sin(\phi_l)\right] \quad (10)$$

is the delay of the echo generated by the l-th target and observed on the v-th virtual channel, R_l, θ_l and ϕ_l denote the range of the l-th target, its azimuth and its elevation (all measured with respect to the center of the receive array), respectively,

$$\psi_l^{(v)} \cong 2\pi f_0 \tau_l^{(v)} \quad (11)$$

and $w_{r,n}^{(v)}$ is the n-th sample of the AWGN sequence affecting the received signal (this sample is modelled as a real Gaussian random variable having zero mean and variance σ^2 for any v). It is important to point out that: a) the real signal model (6) can be adopted in all the FMCW radar systems acquiring only the *in-phase* component of the signal captured by each RX antenna; b) some commercial MIMO radar devices provide both the *in-phase* and *quadrature* components of the received RF signals (e.g., see [17, Par 2.1 eq. (2.2)]). In the last case, the complex model

$$x_{c,n}^{(v)} = \sum_{l=0}^{L-1} A_l^{(v)} \exp\left(j2\pi n F_l^{(v)}\right) + w_{c,n}^{(v)}, \quad (12)$$

must be adopted in place of its real counterpart (6) for any n; here,

$$A_l^{(v)} \triangleq a_l \exp\left(j\psi_l^{(v)}\right) \quad (13)$$

for any v and l, and $w_{c,n}^{(v)}$ is the n-th sample of the AWGN sequence affecting the received signal (this sample is modelled as a complex Gaussian random variable having zero mean and variance σ^2 for any v).

B. MIMO SFCW RADAR SYSTEM

Let us take into consideration now the SFCW radar system shown in Fig. 1b. In this case, the VCO of its transmitter is fed by a *staircase generator*, so that the instantaneous frequency of the resulting RF signal takes on N_f distinct and uniformly spaced values in an interval lasting T s for each TX antenna, as shown in Fig. 2b; the n-th value of the instantaneous frequency is

$$f_n = f_0 + n\,\Delta f, \quad (14)$$

with $n = 0, 1, \ldots, N_f - 1$; here, f_0 is the minimum radiated frequency, Δf is the *frequency step size* and N_f is the overall number of transmitted frequencies. If the sampling frequency $f_s = \Delta f$ is assumed for analog-to-digital conversion at the receive side, the measurement acquired through the v-th virtual element at the n -th frequency can be expressed as (e.g., see [9, eq. (3), Sect. II.B])

$$x_{c,n}^{(v)} = \sum_{l=0}^{L-1} A_l^{(v)} \exp\left(-j2\pi n F_l^{(v)}\right) + w_{c,n}^{(v)}, \quad (15)$$

with $v = 0, 1, \ldots, N_{\mathrm{VR}} - 1$, $n = 0, 1, \ldots, N-1$ and $N = N_f$. Here,

$$A_l^{(v)} \triangleq a_l \exp\left(-j\psi_l^{(v)}\right) \quad (16)$$

and

$$F_l^{(v)} \triangleq \tau_l^{(v)}\,\Delta f \quad (17)$$

are the complex amplitude and the *normalised delay*, respectively, characterizing the l-th target and observed on the v-th virtual antenna; moreover, the parameters (a_l, $\tau_l^{(v)}$) and the random variable $w_{c,n}^{(v)}$ have exactly the same meaning as the one illustrated for the received signal model described by (12) and the phase $\psi_l^{(v)}$ is expressed by (11).

C. TARGET DETECTION AND ESTIMATION

In both the considered FMCW and SFCW radar systems, the useful component of the received signal observed on each virtual channel can be represented as a superposition of L real or complex oscillations; moreover, the value of the parameter L has to be considered *unknown*. In the following derivations, the real samples $\{x_{r,n}^{(v)};\, n = 0, 1, \ldots, N-1\}$ or their complex counterpart $\{x_{c,n}^{(v)};\, n = 0, 1, \ldots, N-1\}$ acquired on the v-th virtual channel are collected in the N-dimensional vector

$$\mathbf{x}_z^{(v)} \triangleq \left[x_{z,0}^{(v)}, x_{z,1}^{(v)}, \ldots, x_{z,N-1}^{(v)}\right]^T, \quad (18)$$

with[3] $z = r$ or c. This vector is processed by the next stages of the radar receiver for target detection and estimation. As it can be easily inferred from (6)–(9) ((12)–(13) and (15)–(17)), in the considered radar system, the problem of *target detection* and *range estimation* on the v-th virtual channel is equivalent to the classic problem of detecting multiple overlapped sinusoids (multiple overlapped complex exponentials) in the presence of AWGN and estimating their *frequencies* (*delays*) [18]. In fact, if, in a FMCW radar system, the l -th tone is found at the frequency $\hat{f}_l^{(v)}$, the presence of a target at the range (see (9) and (10))

$$\hat{R}_{v,l} = \frac{1}{2}\frac{c}{\mu}\hat{f}_l^{(v)} \quad (19)$$

is detected. Similarly, in a SFCW radar system, the normalised delay $\hat{F}_l^{(v)}$ estimated on the v-th virtual channel is associated with a target whose range is (see (10) and (17))

$$\hat{R}_{v,l} = \frac{1}{2}\frac{c}{\Delta f}\hat{F}_l^{(v)}. \quad (20)$$

Information about the angular coordinates (namely, the azimuth and the elevation) of this target, instead, can be acquired through the estimation of the set of N_{VR} phases $\{\psi_l^{(v)};\, v = 0, 1, \ldots, N_{\mathrm{VR}} - 1\}$ observed over the available virtual antennas. In fact, since (see (10) and (11))

$$\psi_l^{(v)} \cong \frac{4\pi}{\lambda}\left[R_l + x_v \cos(\phi_l)\sin(\theta_l) + y_v \sin(\phi_l)\right], \quad (21)$$

[3]In the following, when the letter z will be used in a subscript, it will be implicitly assumed, unless differently stated, that it can be equal to r or c.

where

$$\lambda \triangleq \frac{c}{f_0} \tag{22}$$

is the wavelength associated with the frequency f_0, the sequence $\{\psi_l^{(v)};\ v = 0, 1, \ldots, N_{\mathrm{VR}} - 1\}$ exhibits a periodic behavior characterized by the *normalised horizontal spatial frequency*

$$F_{\mathrm{H},l} \triangleq 2\frac{d_{\mathrm{H}}}{\lambda}\cos(\phi_l)\sin(\theta_l)\,, \tag{23}$$

if the considered virtual elements form an horizontal *uniform linear array* (ULA), whose adjacent elements are spaced d_{H} m apart. Dually, if a virtual vertical ULA is assumed, the periodic variations observed in the same sequence of phases are characterized by the *normalised vertical spatial frequency*

$$F_{\mathrm{V},l} \triangleq 2\frac{d_{\mathrm{V}}}{\lambda}\sin(\phi_l)\,, \tag{24}$$

where d_{V} denotes the distance between adjacent elements of the virtual array itself. Consequently, angle finding can be easily accomplished by *digital beamforming*, i.e. by performing a FFT on the estimated phases taken across multiple elements of the virtual array in a single frame interval [19], [20].

Finally, it is important to note that, in the development of detection and estimation algorithms for colocated MIMO radar systems operating at millimeter waves, the following technical issues need to be taken carefully into account:

1) These radar systems often operate at short ranges and in the presence of extended targets. Each radar image is a *cloud of point targets* whose mutual spacing can be very small [6]. For this reason, the accuracy of these images depends, first of all, on the frequency resolution (*delay* resolution) achieved by the detection and estimation algorithm employed on each virtual antenna in a FMCW (SFCW) radar system. In fact, this makes the radar receiver able to separate point targets characterized by similar ranges.
2) Distinct radar echoes can be characterized by substantially different *signal-to-noise ratios* (SNRs), because of relevant differences among the amplitudes of the L overlapped oscillations forming the useful component of the received signal (see (6), (12) and (15)).
3) The number N of samples acquired over each virtual channel usually ranges from few hundreds to few thousands.

The last two issues explain why significant attention must be paid to the accuracy achieved by the adopted detection and estimation algorithms at low SNRs and/or for relatively small values of N, since this can appreciably influence the quality of the generated radar image.

III. DESCRIPTION OF THE PROPOSED APPROACH TO THE DETECTION AND ESTIMATION OF MULTIPLE TARGETS

All the algorithms developed in the following section can be considered as specific instances of a general approach to target detection and estimation; this approach is described by the block diagram shown in Fig. 3. The processing accomplished by the blocks which this diagram consists of can be summarized as follows. Each vector of the set $\{\mathbf{x}_z^{(v)}\}$, collecting N_{VR} vectors (see (18)), undergoes FFT processing, so that, in a FMCW (SFCW) radar system, the analysis of the acquired measurements is moved from the time-domain (frequency-domain) to the frequency-domain (time-domain). The output of the FFT block is processed by the *range profile estimator* (RPE), that generates the so called *target range profile* (TRP), i.e. a collection of: a) the ranges at which the relevant echoes are detected; b) the associated energies. Note that the last quantities allow us to rank each range on the basis of its perceptual importance. The output of the FFT processing block and the target range profile are processed by the *spatial estimator* (SPE). This block detects all the targets associated with each range appearing in the TRP and estimates their angular parameters; moreover, it may generate a finer estimate of their range. The SPE output is represented by the set

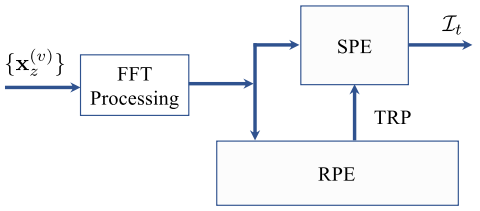

FIGURE 3. Block diagram describing the general approach to target detection and estimation adopted in our work.

$$\mathcal{I}_t \triangleq \left\{\left(\hat{R}_l, \hat{\theta}_l, \hat{\phi}_l, \left|\hat{C}_l\right|\right);\ l = 0, 1, \ldots, \hat{L} - 1\right\} \tag{25}$$

or the set

$$\mathcal{I}_t \triangleq \left\{\left(\hat{R}_l, \hat{\theta}_l, \left|\hat{C}_l\right|\right);\ l = 0, 1, \ldots, \hat{L} - 1\right\} \tag{26}$$

in the case of 3D and 2D imaging, respectively; here, $\hat{L}$ represents an estimate of the parameter L (i.e., of the overall number of point targets), whereas $\hat{R}_l$, $\hat{\theta}_l$, $\hat{\phi}_l$ and $|\hat{C}_l|$ represent an estimate of the range R_l, azimuth θ_l, elevation ϕ_l and amplitude $|C_l|$, respectively, of the l-th target (with $l = 0, 1, \ldots, \hat{L} - 1$).

It is important to point out that:

1) If this approach is adopted, range estimation is decoupled from angular estimation, so that a 3D (2D) detection and estimation problem is turned into a) a 1D detection/estimation problem involving the detection of multiple targets and the estimation of their ranges only plus b) a 2D (1D) estimation problem concerning the targets detected at the same range and the estimation of their azimuth and elevation (azimuth only). Consequently, the overall problem of detecting multiple targets and estimating their range and angles is turned into a couple of simpler detection and estimation problems.
2) The SPE exploits the range information generated by the RPE in order to *concentrate its computational effort*

on a set of well defined ranges; this allows to reduce the size of the search space involved in spatial estimation. This explains also why the processing accomplished by the SPE cannot start before that at a least a portion of the range/energy information (i.e., a portion of the TRP) generated by the RPE becomes available.

3) Various techniques can be exploited in the RPE and in the SPE to develop computationally efficient embodiments of the proposed approach.

As far as the last point is concerned, the following techniques can be adopted by the RPE to mitigate its complexity:

a) *Antenna selection* – This consists in feeding the RPE with a subset of the outputs of the FFT processing block; such outputs are generated on the basis of N_A of the N_{VR} VAs. Note that, on the one hand, a larger N_A allows to compute a more accurate TRP; on the other hand, selecting a smaller N_A results in a reduction of the overall effort required for the computation of the TRP.

b) *Antenna-by-antenna processing* – The measurements acquired through the selected N_A VAs can be efficiently processed by adopting a two-step procedure. In the first step, target range estimation is accomplished on each VA *independently of all the other* VAs, i.e. the acquired measurements are processed on an antenna-by-antenna basis; this is beneficial when parallel computing hardware is employed in the execution of the first step. In the second step, instead, the target range information extracted from each of the selected N_A VAs are fused to generate the TRP.

c) *Serial target cancellation in the range domain* – Target detection and range estimation on each VA represent a *multidimensional problem* since they aim at detecting multiple targets and estimating their ranges. In our method, this multidimensional problem is turned into a sequence of 2D estimation problems by adopting a *serial interference cancellation* (SIC) approach (e.g., see [9]). This means that the noisy signal observed on each VA is processed in an iterative fashion. In each iteration, a single (and, in particular, the strongest) target is detected, and its range and complex amplitude are estimated. Then, the contribution of this target to the received signal is estimated and subtracted from the signal itself (i.e., the detected target is treated as a form of *interference* to be cancelled), so generating a *residual signal*. The last signal represents the input of the next iteration. This procedure is repeated until the overall energy of the residual drops below a given threshold. Note also that the use of this SIC-based approach allows us to mitigate the impact of the spectral leakage due to strong targets, that can potentially hide weak targets having similar ranges.

d) *Alternating maximization* – The estimation of the normalised frequency (or delay) and the complex amplitude of a detected target requires searching for the maximum (or the minimum) of a proper cost function over a 2D domain. In our method, the *alternating maximization* (AM) technique is exploited to develop iterative algorithms that alternate the estimation of the normalised frequency (or delay) of a given target with that of its complex amplitude; for this reason, a 2D optimization problem is turned into a couple of interacting 1D optimization problems (e.g., see [21, Par. IV-A]).

In the SPE block, instead, the following techniques can be employed to reduce its overall computational complexity:

a) *Alternating maximization* – The AM technique is exploited to develop iterative algorithms that alternate the estimation of the elevation of a given target with that of its azimuth. This allows us to decouple the estimation of target elevation from that of its azimuth.

b) *Serial target cancellation in the angular domain* – Each of the ranges collected in the TRP is associated with an unknown number of targets; for this reason, the processing accomplished by the SPE aims at resolving all the targets associated with a given range and estimating their angular coordinates. In the technical literature about radar systems, the detection of an unknown number of targets characterized by the *same range* (or by ranges whose mutual differences are below the range resolution of the employed radar system) and the estimation of their angular parameters is known to be a difficult multidimensional problem (e.g., see [7, Par. III-C]). In our method, a SIC approach is exploited to turn this multidimensional problem into a sequence of 2D (1D) estimation problems in 3D (2D) imaging (see [9] and references therein). This means that the noisy data referring to a specific range and acquired on all the VAs are iteratively processed to detect a single (and, in particular, the strongest) target, and to estimate its angular coordinates and complex amplitude. Then, the contribution of this target to the outputs of the FFT processing block is estimated and subtracted from them, so generating a set of *residual data*. This *detection/estimation/cancellation* procedure is iteratively applied to the residual data until their overall energy drops below a given threshold. Moreover, in a 3D propagation scenario, this procedure is combined with the AM approach described in the previous point; this allows to detect and estimate the angular parameters of a single target (i.e., to solve a 2D optimization problem) by means of an iterative procedure alternating the estimation of its elevation with that of its azimuth (i.e., by means of

an algorithm solving a couple of 1D optimization problems). Note also that, once again, the use of a serial cancellation approach allows us to mitigate the impact of the spectral leakage due to strong targets, that can potentially hide weak targets having similar spatial coordinates.

c) *Parallel processing of the data associated with different ranges* – The detection and the estimation of the targets associated with distinct ranges of the TRP can be accomplished in a *parallel fashion* or in a *sequential fashion*. The first approach is more efficient than the second one if spatial estimation is executed on parallel computing hardware. In fact, in this case, multiple spatial estimation algorithms can be run *in parallel*, one for each of the ranges appearing in the TRP. Note, however, that the price to be paid for this is represented by the fact that the target information generated by all the parallel procedures need to be fused when they end. In fact, the analysis of the measurements referring to close ranges appearing in the TRP may lead to detecting the same target more than one time.

Based on the general approach outlined above and on the techniques listed for the RPE and the SPE, six specific algorithms, called *range & angle serial cancellation algorithms* (RASCAs) are developed in the following. Four of these algorithms apply to colocated MIMO FMCW radar systems, whereas the other two to colocated MIMO SFCW radar systems. The algorithms for FMCW radars are called RASCA-FR2 (RASCA-FC2) and RASCA-FR3 (RASCA-FC3), since they generate 2D and 3D radar images, respectively, on the basis of real (complex) measurements. The algorithms for SFCW radars, instead, are dubbed RASCA-S2 and RASCA-S3. In the description of these algorithms we assume, without loosing generality, that the available measurements are acquired through the $N_{\rm VH} \times N_{\rm VV}$ virtual *uniform rectangular array* (URA) represented in Fig. 4 in the case of 3D imaging and through an *horizontal* ULA (HULA), consisting of $N_{\rm VH}$ virtual antennas, in the case of 2D imaging. In the first case, the horizontal (vertical) spacing between adjacent antennas is denoted $d_{\rm VH}$ ($d_{\rm VV}$), whereas, in the second one, is denoted $d_{\rm VH}$. Moreover, in our considerations, we assume that a *reference* VA, identified by $(p, q) = (p_R, q_R)$ $(p = p_R)$ in the 3D (2D) case, is selected in the virtual array, as exemplified by Fig. 4.

In the following sections, all the RASCAs are described. In Section IV we first focus on the RASCA-FR3 and RASCA-FC3, i.e. on the algorithms to be employed in a MIMO FMCW radar system equipped with a 2D antenna array (in particular, with the URA shown in Fig. 4). Then, we show how to adapt these algorithms to the case in which this radar system is equipped with a 1D antenna array (in particular, with an ULA); this leads to the RASCA-FR2 and the RASCA-FC2. Then, in Section V we show how to adapt RASCA-FC3 and RASCA-FC2 algorithms to be employed in a MIMO SFCW radar system to obtain RASCA-S3 and RASCA-S2, respectively.

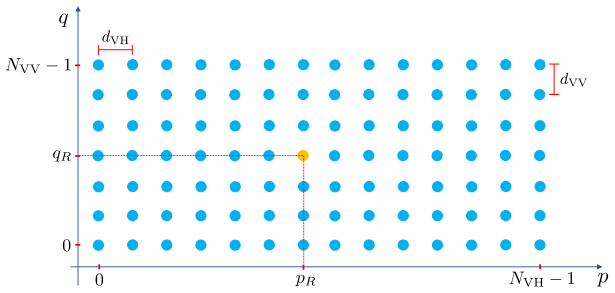

FIGURE 4. Virtual antenna array considered in the description of our detection and estimation algorithms. The reference VA selected in this case is identified by a yellow circle.

IV. RANGE & ANGLE SERIAL CANCELLATION ALGORITHMS FOR A FREQUENCY MODULATED CONTINUOUS WAVE RADAR SYSTEM

In this paragraph, we provide a short description of the architecture of the RASCAs for FMCW radar systems and comment on the method we developed for target detection and cancellation in the angular domain. Then, we illustrate RASCA-FR3 and RASCA-FC3 in detail. Finally, we show how to derive the RASCA-FR2 and RASCA-FC2 from them.

A. ARCHITECTURE OF THE RANGE & ANGLE SERIAL CANCELLATION ALGORITHMS FOR A FREQUENCY MODULATED CONTINUOUS WAVE RADAR SYSTEM

The inner structure of the RASCAs for an FMCW radar system is described by the block diagram shown in Fig. 5, whereas the meaning of the most relevant parameters, sets, vectors and matrices appearing in the description of this algorithm is summarised in Table 1.. The processing accomplished inside the blocks appearing in that figure can be summarized as follows. The FFT *processing* block turns the *time domain* information provided by the set of $N_{\rm VR}$ vectors $\{\mathbf{x}_z^{(v)}\}$ into the *frequency domain* information feeding both the RPE and the SPE blocks. This transformation requires the evaluation of $3N_{\rm VR}$ FFTs, all of order N_0. In fact, it consists in the evaluation of the triad $(\mathbf{X}_0^{(v)}, \mathbf{X}_1^{(v)}, \mathbf{X}_2^{(v)})$, collecting three N_0 -dimensional vectors, on the basis of $\mathbf{x}_z^{(v)}$, for $v = 0, 1, \ldots, N_{\rm VR} - 1$. For this reason, the output of the considered block is represented by the set

$$\mathcal{S}_{\rm FFT} \triangleq \left\{ \left(\mathbf{X}_0^{(v)}, \mathbf{X}_1^{(v)}, \mathbf{X}_2^{(v)} \right); v = 0, 1, \ldots, N_{\rm VR} - 1 \right\}, \quad (27)$$

consisting of $3 \cdot N_{\rm VR}$ N_0-dimensional vectors. Note that, however, a portion of this set is discarded by the RPE, since this block processes the information originating from N_A distinct VAs only. The triads selected by the RPE form the subset

$$\bar{\mathcal{S}}_{\rm FFT} \triangleq \left\{ \left(\mathbf{X}_0^{(v)}, \mathbf{X}_1^{(v)}, \mathbf{X}_2^{(v)} \right); v \in \mathcal{S}_A \right\}, \quad (28)$$

of $\mathcal{S}_{\rm FFT}$ (27); here,

$$\mathcal{S}_A \triangleq \left\{ v_0, v_1, \ldots, v_{N_A-1} \right\}, \quad (29)$$

TABLE 1. Most relevant parameters, sets, vectors and matrices appearing in our description of RASCA-FC3.

Parameter	Description
$\mathbf{x}_{0,\mathrm{ZP}}^{(v)}$	Zero-padded version of the vector $\{\mathbf{x}_z^{(v)}\}$.
$\mathbf{x}_{m,\mathrm{ZP}}^{(v)}$	Zero-padded version of the vector $\{\mathbf{x}_m^{(v)}\}$ (with $m = 1$ and 2).
$\mathbf{X}_m^{(v)}$	DFT of the vector $\mathbf{x}_{m,\mathrm{ZP}}^{(v)}$ (with $m = 0$, 1 and 2).
$\mathcal{S}_{\mathrm{FFT}}$	Set collecting the N_{VR} triads $(\mathbf{X}_0^{(v)}, \mathbf{X}_1^{(v)}, \mathbf{X}_2^{(v)})$ such that $v = 0, 1, \ldots, N_{\mathrm{VR}} - 1$.
N_A	Number of virtual antennas exploited by the RPE.
$\mathcal{S}_A$	Set collecting the N_A indices of the virtual antennas exploited by the RPE.
$\bar{\mathcal{S}}_{\mathrm{FFT}}$	Set collecting the N_A triads $(\mathbf{X}_0^{(v)}, \mathbf{X}_1^{(v)}, \mathbf{X}_2^{(v)})$ such that $v \in \mathcal{S}_A$.
T_{STDREC}	Threshold set in the STDREC algorithm to limit its overall number of iterations.
$\mathrm{X}_m^{(v_k)}[i]$	Residual spectrum available for the v_k-th antenna at the end of the $(i-1)$-th iteration of the STDREC algorithm.
$E_i^{(v_k)}$	Energy associated with the residual spectrum $\mathrm{X}_m^{(v_k)}[i]$ and computed by the STDREC algorithm for the v_k-th antenna at the end of its $(i-1)$-th iteration.
$\hat{C}_i^{(v_k)}$	Estimate of the complex amplitude $C_i^{(v_k)}$ computed for the v_k-th antenna in the i-th iteration of the STDREC algorithm.
$\hat{F}_i^{(v_k)}$	Estimate of the normalised frequency $F_i^{(v_k)}$ computed for the v_k-th antenna in the i-th iteration of the STDREC algorithm.
$\mathbf{C}_{X_m}^{(v_k)}[i]$	Estimate of the contribution given by the i-th target detected on the v_k-th antenna to the vector $\mathrm{X}_m^{(v_k)}[i]$ (with $m = 0$, 1 and 2).
$\mathcal{S}_{\mathrm{RPE}}$	Set collecting the information generated by the RPE and feeding to the SPE.
T_{STDAEC}	Threshold set in the STDAEC algorithm to limit its overall number of recursions.
$\mathbf{X}^{(i)}[l]$	Matrix representing the spectral contribution given by the l-th frequency bin and available at the beginning of the i-th iteration of the STDAEC algorithm.
$E^{(i)}[l]$	Energy associated with the residual spectrum $\mathbf{X}^{(i)}[l]$ made available by the STDAEC algorithm for the l-th frequency bin at the end of its $(i-1)$-th iteration.
$\mathbf{s}_{\mathrm{VULA},k}^{(i)}[l]$	k - th vector collecting the spectral information computed for the reference VULA and the l-th frequency bin in the i-th iteration of the STDAEC algorithm (with $k = 0$, 1 and 2).
$\hat{C}_{\mathrm{V},i}[l]$	Estimate of the complex amplitude $C_{\mathrm{V},i}[l]$ computed for the target detected in the l-th frequency bin within the i-th iteration of the STDAEC algorithm.
$\hat{F}_{\mathrm{V},i}[l]$	Estimate of the normalised vertical spatial frequency $F_{\mathrm{V},i}[l]$ computed for the target detected in the l-th frequency bin within the i-th iteration of the STDAEC algorithm.
$R_i^{(\mathrm{VF})}[l,q]$	Phase rotation factor computed for the q-th VULA and the l-th frequency bin within the i-th iteration of the STDAEC algorithm (vertical folding).
$\mathbf{X}_i^{(\mathrm{VF})}[l]$	Vertically folded spectrum computed for the l-th frequency bin within the i-th iteration of the STDAEC algorithm.
$\hat{C}_{\mathrm{H},i}[l]$	Estimate of the complex amplitude $C_{\mathrm{H},i}[l]$ computed on the basis of a vertically folded spectrum within the i-th iteration of the STDAEC algorithm for the l-th frequency bin.
$\hat{F}_{\mathrm{H},i}[l]$	Estimate of the normalised horizontal spatial frequency $F_{\mathrm{H},i}[l]$ computed on the basis of a vertically folded spectrum within the i-th iteration of the STDAEC algorithm.
$R_i^{(\mathrm{HF})}[l,p]$	Phase rotation factor computed for the p-th HULA and the l-th frequency bin within the i-th iteration of the STDAEC algorithm (horizontal folding).
$R_i^{(\mathrm{HV})}[l,p,q]$	Phase rotation factor computed for the (p,q) VA and the l-th frequency bin within the i-th iteration of the STDAEC algorithm (overall folding).
$\{\mathbf{X}_{m,\mathrm{OF}}^{(i)}[l]\}$	Overall folded spectrum computed for the l-th frequency bin within the i-th iteration of the STDAEC algorithm.
$\hat{C}_i[l]$	Estimate of the complex amplitude $C_i[l]$ computed on the basis of a overall folded spectrum within the i-th iteration of the STDAEC algorithm.
$\hat{F}_i[l]$	Estimate of the normalised frequency $F_i[l]$ computed on the basis of a overall folded spectrum within the i-th iteration of the STDAEC algorithm.
$\mathbf{C}_{X_0}^{(i)}[l]$	Estimate of the contribution, given by the target detected within i-th iteration of the STDAEC algorithm, to the vector $\mathbf{X}^{(i)}[l]$.
$\hat{R}_i[l]$, $\hat{\theta}_i[l]$, $\hat{\phi}_i[l]$	Estimates of the range, azimuth and elevation made available by the SPE for the i-th target detected in the l-th frequency bin.

represents the set of the values of the VA index v identifying the elements of $\mathcal{S}_{\mathrm{FFT}}$ that belong to $\bar{\mathcal{S}}_{\mathrm{FFT}}$. Each of the triads of $\bar{\mathcal{S}}_{\mathrm{FFT}}$ is processed, independently of all the other ones, by a novel iterative estimation algorithm called *single target detection, range estimation and cancellation* (STDREC). This algorithm detects the most relevant targets on the selected antenna and estimates their ranges (i.e., the frequencies associated with these ranges; see (9) and (19)) and their complex amplitudes (see (11) and (13)). The name of this algorithm originates from the fact that, in each of its iterations, it *detects* a single target (namely, the strongest target), *estimates* its parameters (and, in particular, the frequency characterizing it, i.e. its range) and *cancels* the target contribution to the received signal; the residual signal resulting from target cancellation represents the input of the next iteration. The output of the STDREC algorithm that processes

the raw data originating from the v_k-th VA is represented by the set[4]

$$\mathcal{S}_{v_k} \triangleq \left\{ \left(\hat{\alpha}_i^{(v_k)}, \hat{C}_i^{(v_k)} \right), i = 0, 1, \ldots, L_k - 1 \right\}, \quad (30)$$

with $k = 0, 1, \ldots, N_A - 1$; here, L_k is the overall number of targets detected on the considered VA, whereas $\hat{C}_i^{(v_k)}$ and $\hat{\alpha}_i^{(v_k)}$ represent the estimate of the complex amplitude of the i-th target and the index of the *frequency bin*[5] in which this target has been detected. Finally, the information provided by the N_A sets $\{\mathcal{S}_{v_k}\}$ are merged to generate the single set

$$\mathcal{S}_{\text{RPE}} \triangleq \left\{ \left(\hat{\alpha}_l, E_{b,l} \right), l = 0, 1, \ldots, L_b - 1 \right\}, \quad (31)$$

where L_b is the overall number of targets detected on all the selected VAs, $\hat{\alpha}_l$ is the index of the *frequency bin* in which the l-th target has been detected and $E_{b,l}$ is the average energy estimated for it. Note that:

a) The cardinality L_b of the set $\mathcal{S}_{\text{RPE}}$ represents a preliminary estimate of the overall number of targets; in fact, multiple targets having the same range or ranges whose mutual differences are below the resolution of the employed radar system are detected as a single target and no effort is made at this stage to separate their contributions.

b) The energies $\{E_{b,l}\}$ represent the perceptual importance of the identified frequency bins, in the sense that a larger energy is associated with a more important frequency bin.

Both the sets $\mathcal{S}_{\text{FFT}}$ (27) and $\mathcal{S}_{\text{RPE}}$ (31) feed the SPE. The aim of this block is to analyse the spectral information associated with the ranges (i.e., with the frequency bins) identified by the RPE in order to: a) estimate the angular coordinates (i.e., azimuth and elevation) of the targets contributing to each frequency bin; b) detect additional targets associated with adjacent frequency bins and potentially hidden by the spectral leakage due to stronger targets; c) estimate the angular coordinates (i.e., azimuth and elevation) of such additional targets and compute a finer estimate of their range.

The first stage of the processing accomplished by the SPE involves the whole set $\mathcal{S}_{\text{FFT}}$ (27) and is executed on a bin-by-bin basis, since it aims at: a) detecting all the targets that contribute to the energy of each frequency bin contained in the TRP and b) estimating their angular coordinates. For this reason, this stage consists of L_b estimators running *in parallel*; each estimator focuses on one of the L_b frequency bins (i.e., ranges) appearing in the TRP (see Fig. 5). Moreover, each estimator executes a novel iterative estimation algorithm, called *single target detection, angular estimation and cancellation* (STDAEC). The l-th STDAEC algorithm processes the spectral information available on the whole virtual receive array and referring to the $\hat{\alpha}_l$-th frequency bin only (with $l = 0, 1, \ldots, L_b - 1$), detects $L[l]$ targets contributing to it and, for each detected target, computes: a) an estimate of its complex amplitude; b) an estimate of its angular coordinates (i.e., its azimuth and its elevation); c) a refined estimate of its range (do not forget that the preliminary estimate of this range is provided by the bin index $\hat{\alpha}_l$). If $D[l]$ iterations are accomplished by the l-th STDAEC algorithm, $D[l]$ distinct targets are detected in the $\hat{\alpha}_l$-th frequency bin, provided that none of them is classified as a *false* (i.e., *ghost*) *target*. In addition, all the estimates generated by this algorithm are collected in the set

$$\mathcal{T}_l \triangleq \left\{ \left(\hat{C}_i[l], \hat{F}_i[l], \hat{\alpha}_i[l], \hat{F}_{\text{V},i}[l], \hat{F}_{\text{H},i}[l] \right); \right. \\ \left. i = 0, 1, \ldots, D[l] - 1 \right\}, \quad (32)$$

or in the set

$$\mathcal{T}_l \triangleq \left\{ \left(\hat{C}_i[l], \hat{F}_i[l], \hat{\alpha}_i[l], \hat{F}_{\text{H},i}[l] \right); \right. \\ \left. i = 0, 1, \ldots, D[l] - 1 \right\}, \quad (33)$$

with $l = 0, 1, \ldots, L_b - 1$, in the case of 3D and 2D radar imaging, respectively; here, $\hat{C}_i[l]$, $\hat{F}_i[l]$ and $\hat{\alpha}_i[l]$ denote the estimates of the complex amplitude $C_i[l]$, of the normalised frequency $F_i[l]$ and of the frequency bin $\alpha_i[l]$, respectively, characterizing the i-th target detected *on the reference* VA and in the l-th frequency bin, whereas $\hat{F}_{\text{H},i}[l]$ and $\hat{F}_{\text{V},i}[l]$ represent the estimates of the normalised horizontal spatial frequency $F_{\text{H},i}[l]$ and of the normalised vertical spatial frequency $F_{\text{V},i}[l]$, respectively, referring to the above mentioned target.

Finally, in the second (and last) stage of the SPE, the spatial coordinates of all the detected targets are computed on the basis of the spatial information collected in the L_b sets $\{\mathcal{T}_l\}$ and an overall image of the propagation scenario is generated in the form of a *point cloud*.

B. SOME CONSIDERATIONS ON TARGET DETECTION AND CANCELLATION IN THE ANGULAR DOMAIN

It is worth pointing out that the STDAEC algorithm represents the most complicated part of the processing accomplished by all the blocks appearing in Fig. 5. The derivation of this algorithm relies on the fact that: a) each target provides an *additive contribution* to the spectra evaluated on all the VAs; b) *periodic variations* are observed in the phase of this contribution if we move horizontally or vertically along the considered virtual array (see Fig. 4). In fact, if we assume that the intensity of the echo received by each VA from the i-th target detected in the l-th frequency bin does not change from antenna to antenna, the complex amplitude $C_i[p, q, l]$ observed on the (p, q) VA can be expressed as (see (9) and (10))

$$C_i[p, q, l] = C_i[l] \exp\left[j \frac{4\pi}{\lambda} \left[d_{\text{VH}} (p - p_R) \cos(\phi_i[l]) \right. \right. \\ \left. \left. \cdot \sin(\theta_i[l]) + d_{\text{VV}} (q - q_R) \sin(\phi_i[l]) \right] \right]; \quad (34)$$

[4]Note that the complex amplitude $\hat{C}_i^{(v_k)}$ appearing in the following equations is replaced by $\hat{A}_i^{(v_k)}$ if the received sequence is complex (see eqs. (7) and (13)). This consideration holds for various equations appearing in the remaining part of this manuscript.

[5]Generally speaking, the evaluation of an FFT of order N_0 leads to partitioning the normalised frequency interval $[0, 1/2)$ in N_0 *frequency bins*.

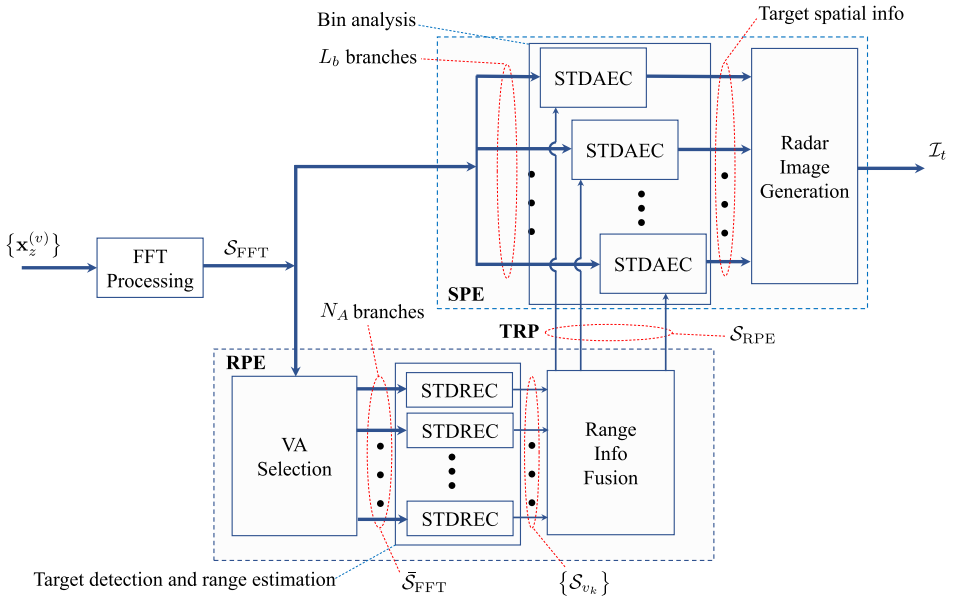

FIGURE 5. Block diagram describing the inner structure of the RASCAs for an FMCW radar system.

here, $\lambda = c/f_0$ is the wavelength associated with the start frequency (see (14)), (p_R, q_R) is the couple of integers identifying the selected *reference* VA, $\theta_i[l]$, $\phi_i[l]$ and $R_i[l]$ are the azimuth, the elevation and the range, respectively, characterizing the considered target, and $C_i[l]$ is its complex amplitude observed on the reference antenna. If (34) holds, the rate of the phase variations observed in the complex amplitudes $\{C_i[p, q, l]\}$ for a given l is proportional to (see (23) and (24))

$$F_{\text{H},i}[l] \triangleq \frac{2d_{\text{VH}}}{\lambda} \cos(\phi_i[l]) \sin(\theta_i[l]) \tag{35}$$

and

$$F_{\text{V},i}[l] \triangleq \frac{2d_{\text{VV}}}{\lambda} \sin(\phi_i[l]), \tag{36}$$

if we move along an HULA and a *vertical* ULA (VULA), respectively. In fact, the quantity $F_{\text{H},i}[l]$ ($F_{\text{V},i}[l]$) represents the normalised horizontal (vertical) *spatial frequency* characterizing the i-th target detected in the l-th frequency bin; if both these frequencies are known, the elevation and the azimuth of this target can be evaluated as

$$\phi_i[l] = \arcsin\left(\frac{\lambda}{2d_{\text{VV}}} F_{\text{V},i}[l]\right) \tag{37}$$

and

$$\theta_i[l] = \arcsin\left(\frac{\lambda}{2d_{\text{VH}} \cos(\phi_i[l])} F_{\text{H},i}[l]\right), \tag{38}$$

respectively.

Moreover, in the derivation of the STDAEC algorithm, the following two techniques have been exploited:

Serial cancellation of targets – This technique is conceptually similar to the cancellation strategy exploited by the STDREC algorithm and allows us to detect multiple targets in the same frequency bin and, in particular, to identify targets having similar spatial coordinates. It is important to keep in mind that the frequencies associated with distinct targets detected in the same frequency bin do not necessarily belongs to that bin; in fact, they can belong to adjacent bins, so that the tails (not the peak) of their spectra are really observed in the considered frequency bin. This problem originates from the fact that, generally speaking, *the contribution of a point target to the spectrum computed on each* VA *is not a line*, unless the associated normalised frequency is exactly a multiple of the fundamental frequency

$$F_{\text{FFT}} = 1/N_0, \tag{39}$$

consequently, such a contribution is spread over multiple adjacent frequency bins (i.e., spectral leakage is observed)

Spatial folding – As already stated above, the frequency associated with a target detected in the l-th frequency bin does not necessarily fall exactly in that bin. The technique dubbed *spatial folding* has been devised to: a) evaluate a more accurate estimate of the frequency associated with a target detected in a given bin; b) discriminate real targets from ghost targets. Spatial folding is based on the following idea. Once the horizontal and the vertical spatial frequencies associated with a target detected in a given frequency bin have been estimated (see (35) and (36)), the spectra computed on multiple VAs can be combined *in a constructive fashion* by

1) taking a *reference* VA (identified by $(p, q) = (p_R, q_R)$; see Fig. 4), and compensating for the phase differences, estimated for that target, between the reference VA and the other VAs of the whole array, or
2) taking a *reference* ULA and compensating for the phase differences, estimated for that target, between the reference ULA and other ULAs *parallel* to it.

In case 1), folding generates a single spectrum, dubbed *folded spectrum* , and has the beneficial effects of a) averaging out the effects of the noise that affects the VAs and b) combining, in a constructive fashion, the contributions of all the targets different from the one which the employed spatial frequencies refer to. For this reason, in analysing the amplitude of the folded spectrum, a well defined peak in its amplitude is expected in the l-th frequency bin or in a bin close to it. When this peak is detected, a refined estimate of the frequency (and, consequently, of the range) and the complex amplitude characterizing the target for which folding has been accomplished can be computed by identifying its position. On the contrary, if no peak is found, the detected target is actually a *ghost target*. In case 2), folding generates as many *folded spectra* as the number of antennas of the reference ULA and offers the same advantages as case 1).

In the remaining part of this manuscript, when folding is employed, the following terminology is adopted:

Vertical folding – This refers to the case in which folding involves a reference HULA on which other HULAs are folded.

Overall folding – This refers to the case in which folding involves all the spectra, i.e. the overall virtual URA; a single folded spectrum is computed in this case.

Note that, in any case, folding may involve the *whole* virtual receive array or *a portion of it*. The exploitation of a subset of the available VAs is motivated by the fact that, in practice, in computing a folded spectrum that refers to the l-th frequency bin, the *estimates* $\hat{F}_{\mathrm{H},i}[l]$ and $\hat{F}_{\mathrm{V},i}[l]$ of the frequencies $F_{\mathrm{H},i}[l]$ and $F_{\mathrm{V},i}[l]$, respectively, are employed, so that the quality of the phase compensation factors computed for the antennas that are *farther* from the reference antenna or the reference HULA may be affected by significant *estimation errors*.

All the mathematical details about vertical and overall folding can be found in the next paragraph.

C. DETAILED DESCRIPTION OF THE RANGE & ANGLE SERIAL CANCELLATION ALGORITHMS FOR A FREQUENCY MODULATED CONTINUOUS WAVE RADAR SYSTEM ENDOWED WITH A TWO-DIMENSIONAL ANTENNA ARRAY

In the following, the RASCA-FR3 is described first; then, the (minor) modifications required to obtain the RASCA-FC3 from it are illustrated. The RASCA-FR3 processing is divided in three tasks, each associated with one of the blocks appearing in Fig. 5 (the i-th task is denoted Ti); a description of each task is provided below. Various details about the techniques employed in these tasks, omitted here to ease the understanding of the overall flow of the algorithm, are provided in Section VI.

1) **T1**–FFT PROCESSING

The processing accomplished within this task can be summarized as follows. Given the vector $\mathbf{x}_z^{(v)}$, the N-dimensional vectors

$$\mathbf{x}_1^{(v)} \triangleq \left[x_{1,0}^{(v)}, x_{1,1}^{(v)}, \ldots, x_{1,N-1}^{(v)}\right]^T \tag{40}$$

and

$$\mathbf{x}_2^{(v)} \triangleq \left[x_{2,0}^{(v)}, x_{2,1}^{(v)}, \ldots, x_{2,N-1}^{(v)}\right]^T \tag{41}$$

are evaluated for $v = 0, 1, \ldots, N_{\mathrm{VR}} - 1$; here,

$$x_{m,n}^{(v)} \triangleq n^m \, x_{z,n}^{(v)} \tag{42}$$

with $n = 0, 1, \ldots, N-1$ and $m = 1, 2$. Then, the vectors $\mathbf{x}_z^{(v)}$, $\mathbf{x}_1^{(v)}$ and $\mathbf{x}_2^{(v)}$ undergo *zero padding* (ZP) for any v; this produces the N_0 -dimensional vectors

$$\mathbf{x}_{0,\mathrm{ZP}}^{(v)} = \left[(\mathbf{x}_z^{(v)})^T \; \mathbf{0}_{(M-1)N}^T\right]^T, \tag{43}$$

$$\mathbf{x}_{1,\mathrm{ZP}}^{(v)} = \left[(\mathbf{x}_1^{(v)})^T \; \mathbf{0}_{(M-1)N}^T\right]^T \tag{44}$$

and

$$\mathbf{x}_{2,\mathrm{ZP}}^{(v)} = \left[(\mathbf{x}_2^{(v)})^T \; \mathbf{0}_{(M-1)N}^T\right]^T, \tag{45}$$

respectively; here, M is a positive integer (dubbed *oversampling factor*), $\mathbf{0}_D$ is a D-dimensional (column) null vector and

$$N_0 \triangleq M\,N. \tag{46}$$

Finally, the N_0-dimensional vectors

$$\begin{aligned}\mathbf{X}_m^{(v)} &= \left[X_{m,0}^{(v)}, X_{m,1}^{(v)}, \ldots, X_{m,N_0-1}^{(v)}\right]^T = \mathbf{X}_m[p,q] \\ &= \left[X_{m,0}[p,q], X_{m,1}[p,q], \ldots, X_{m,N_0-1}[p,q]\right]^T \\ &\triangleq \mathrm{DFT}_{N_0}\left[\mathbf{x}_{m,\mathrm{ZP}}^{(v)}\right],\end{aligned} \tag{47}$$

with $m = 0,\ 1,\ 2$, are computed for any v (i.e., for any p and q) by executing a N_0 order FFT for each of them; here, $\mathrm{DFT}_{N_0}[\mathbf{x}]$ denotes, up to a scale factor, the N_0 order *discrete Fourier transform* (DFT) of the N_0-dimensional vector $\mathbf{x}$. More specifically, we assume that

$$X_{m,k}^{(v)} \triangleq \frac{1}{N}\sum_{n=0}^{N-1} n^m \, x_{z,n}^{(v)} \exp\left(-j\frac{2\pi nk}{N_0}\right), \tag{48}$$

with $k = 0, 1, \ldots, N_0 - 1$ and $m = 0,\ 1,\ 2$.

2) **T2**–RPE

The processing accomplished within this task consists of the three consecutive steps listed below (the i-th step is denoted T2-Si in the following); each step is associated with one of the blocks included in the RPE, as shown in Fig. 5.

T2-S1) VA *selection* – In this step, the set $\bar{\mathcal{S}}_{\mathrm{FFT}}$ (28) is built. This requires generating the set $\mathcal{S}_A$ (29), i.e. a set of N_A integers that identifies the selected VAs. In our computer simulations, the elements of $\mathcal{S}_A$ have been generated by *randomly* extracting N_A distinct integers from the set $\{0, 1, \ldots, N_{\mathrm{VR}} - 1\}$.

T2-S2) *Target detection and range estimation* – The processing carried out within this step is executed by the STDREC algorithm; this operates on an antenna-by-antenna

basis. The STDREC processing for the v_k-th VA (with $k = 0, 1, \ldots, N_A - 1$) can be summarized as follows. A simple initialization is accomplished first by setting

$$\mathbf{X}_m^{(v_k)}[0] \triangleq \mathbf{X}_m^{(v_k)}, \tag{49}$$

with $m = 0, 1, 2$, and the iteration index i to 0. Then, the STDREC iterations are started; in the i-th iteration, the three steps described below are accomplished to detect a new target and cancel its contribution to the triad $(\mathbf{X}_0^{(v_k)}[i], \mathbf{X}_1^{(v_k)}[i], \mathbf{X}_2^{(v_k)}[i])$ (the p-th step of each is denoted STDREC-S p in the following).

STDREC-S1) *Detection of a new target and estimation of its parameters* – The triad $(\mathbf{X}_0^{(v_k)}[i], \mathbf{X}_1^{(v_k)}[i], \mathbf{X}_2^{(v_k)}[i])$ is processed to detect a new (i.e., the i-th) target, and to estimate the normalised frequency $F_i^{(v_k)}$ and the complex amplitude $C_i^{(v_k)}$ associated with it. Note that, generally speaking, the normalised frequency $F_i^{(v_k)}$ is not a multiple of the fundamental frequency F_{FFT} (39), that characterizes the FFT processing executed in **T1**; for this reason, it can be expressed as

$$F_i^{(v_k)} = F_{c,i}^{(v_k)} + \delta_i^{(v_k)} F_{\mathrm{DFT}}, \tag{50}$$

where $F_{c,i}^{(v_k)}$ represents a *coarse estimate* of $F_i^{(v_k)}$ and $\delta_i^{(v_k)}$ is a real parameter called *residual*. This step consists in executing an algorithm, dubbed *single frequency estimator*[6] (SFE) and whose detailed description is provided in Paragraph VI-A. In short, the SFE computes the estimates $\hat{C}_i^{(v_k)}$, $\hat{F}_{c,i}^{(v_k)}$, $\hat{\delta}_i^{(v_k)}$,

$$\hat{\alpha}_i^{(v_k)} = \left\lfloor \hat{F}_{c,i}^{(v_k)} / F_{\mathrm{DFT}} \right\rfloor \tag{51}$$

and

$$\hat{F}_i^{(v_k)} = \hat{F}_{c,i}^{(v_k)} + \hat{\delta}_i^{(v_k)} F_{\mathrm{DFT}} \tag{52}$$

of the parameters $C_i^{(v_k)}$, $F_{c,i}^{(v_k)}$, $\delta_i^{(v_k)}$, $\alpha_i^{(v_k)}$ and $F_i^{(v_k)}$, respectively, on the basis of the triad $(\mathbf{X}_0^{(v_k)}[i], \mathbf{X}_1^{(v_k)}[i], \mathbf{X}_2^{(v_k)}[i])$; here, $\hat{\alpha}_i^{(v_k)}$ represents the index of the frequency bin in which the i-th target is detected on the v_k-th antenna. Note that the parameter $\hat{F}_i^{(v_k)}$, even if useless in the construction of the set $\mathcal{S}_{v_k}$ (30), is exploited in the next step.

STDREC-S2) *Cancellation of the new target* – The contribution $(\mathbf{C}_{X_0}^{(v_k)}[i], \mathbf{C}_{X_1}^{(v_k)}[i], \mathbf{C}_{X_2}^{(v_k)}[i])$, given by the i-th (i.e., by the last) target detected on the v_k-th VA, to the triad $(\mathbf{X}_0^{(v_k)}[i], \mathbf{X}_1^{(v_k)}[i], \mathbf{X}_2^{(v_k)}[i])$ is computed on the basis of (130)–(132) (see Paragraph VI-D) and cancelled from the triad itself. Cancellation consists in the computation of the new *residual* triad

$$\begin{aligned}\mathbf{X}_m^{(v_k)}[i+1] &= \left[X_{m,0}^{(v_k)}[i+1], \ldots, X_{m,N_0-1}^{(v_k)}[i+1]\right]^T \\ &\triangleq \mathbf{X}_m^{(v_k)}[i] - \mathbf{C}_{X_m}^{(v_k)}[i],\end{aligned} \tag{53}$$

with $m = 0, 1, 2$.

[6]Note that our general description of the SFE includes the computation of three DFTs, that, in this case, are already evaluated in **T1**.

STDREC-S3) *Computation of the residual energy in the frequency domain* – The energy

$$E_{i+1}^{(v_k)} \triangleq \left\| \mathbf{X}_0^{(v_k)}[i+1] \right\|^2 = \sum_{p=0}^{N_0-1} \left| X_{0,p}^{(v_k)}[i+1] \right|^2 \tag{54}$$

characterizing the residual spectrum vector $\mathbf{X}_0^{(v_k)}[i+1]$ (53) is computed and compared with the positive threshold T_{STDREC} (which may depend on range, i.e. on the detected frequency). If this energy is below the threshold, the STDREC algorithm stops and $L_k = i$ relevant targets are detected on the v_k -th VA; otherwise, the recursion index i is increased by one and a new recursion is started by going back to **STDREC-S1**.

T2-S3) *Fusion of range information* – This step aims at merging the information provided by the N_A sets $\{\mathcal{S}_{v_k}\}$ (30) evaluated in the previous step. Its output is represented by the set $\mathcal{S}_{\mathrm{RPE}}$ (31), whose elements (i.e., the L_b couples $\{(\hat{\alpha}_l, E_{b,l})\}$) are evaluated as follows. If we define the set

$$\mathcal{A}_b^{(v_k)} \triangleq \{\hat{\alpha}_i^{(v_k)};\, i = 0, 1, \ldots, L_k - 1\}, \tag{55}$$

identifying all the bins in which *at least one target* has been detected on the v_k-th VA (with $k = 0, 1, \ldots, N_A - 1$), the set

$$\mathcal{A}_b \triangleq \{\hat{\alpha}_l;\, l = 0, 1, \ldots, L_b - 1\} \tag{56}$$

is generated by putting together all the distinct integers that appear at least once in the N_A sets $\{\mathcal{A}_b^{(v_k)};\, k = 0, 1, \ldots, N_A - 1\}$. Then, the average energy $E_{b,l}$ associated with the $\hat{\alpha}_l$-th bin (with $l = 0, 1, \ldots, L_b - 1$) is computed as

$$E_{b,l} = \frac{1}{N_{b,l}} \sum_{k=0}^{N_A-1} \sum_{i=0}^{L_k-1} \left| \hat{C}_i^{(v_k)} \right|^2 \delta\left[\hat{\alpha}_i^{(v_k)} - \hat{\alpha}_l\right], \tag{57}$$

where

$$N_{b,l} = \sum_{k=0}^{N_A-1} \sum_{i=0}^{L_k-1} \delta\left[\hat{\alpha}_i^{(v_k)} - \hat{\alpha}_l\right] \tag{58}$$

represents the overall number of antennas that contribute to this energy (here, $\delta[z] = 1$ if $z = 0$ and $\delta[z] = 0$ if $z \neq 0$)

3) T3–SPE

The processing accomplished within this task consists of the two consecutive steps listed below (the i-th step is denoted T3-Si in the following); each step is associated with one of the blocks contained in the SPE represented in Fig. 5.

T3-S1) *Bin analysis* – Within this step, L_b STDAEC algorithms are run *in parallel*, one for each of the L_b ranges (i.e., frequency bins) appearing in the TRP. A schematic description of l -th STDAEC algorithm is provided below (with $l = 0, 1, \ldots, L_b - 1$). This algorithm consists of three steps (its r-th step is denoted STDAEC-Sr in the following) and is initialised by

1) Setting its iteration index i to 0.
2) Setting

$$\mathbf{X}^{(0)}[l] \triangleq \mathbf{X}[l], \tag{59}$$

where

$$\mathbf{X}[l] \triangleq \left[X_{0,\hat{\alpha}_l}[p,q]\right], \tag{60}$$

is a $N_{\mathrm{VH}} \times N_{\mathrm{VV}}$ matrix collecting the spectral information available on the whole virtual receive array and referring to the $\hat{\alpha}_l$-th frequency bin only.

Then, the STDAEC algorithm starts executing its iterations. Within its i -th iteration, it accomplishes the three steps described below.

STDAEC-S1) *Detection of a new target and estimation of its angular parameters* – In this step, the $N_{\mathrm{VH}} \times N_{\mathrm{VV}}$ matrix

$$\mathbf{X}^{(i)}[l] \triangleq \left[X_l^{(i)}[p,q]\right], \tag{61}$$

is processed to detect the strongest target contributing to it, and to compute the estimates $\hat{\theta}_i[l]$, $\hat{\phi}_i[l]$ and $\hat{C}_i[l]$ of $\theta_i[l]$, $\phi_i[l]$) and $C_i[l]$, respectively (note that this target represents the i-th one detected in the considered frequency bin, since $(i-1)$ targets have been detected in the previous recursions). This result is achieved by executing a novel iterative detection and estimation algorithm called *single target detection and angular estimation* (STDAE), whose description is provided after illustrating the overall structure of the RASCA-FR3 to ease reading.

STDAEC-S2) *Target cancellation* – The contribution $\mathbf{C}_{X_0}^{(i)}[l]$, given by the i-th target detected in the l-th frequency bin, to the vector $\mathbf{X}^{(i)}[l]$ (61) is computed on the basis of (144)–(145) (see Paragraph VI-D) and is cancelled. Cancellation consists in the computation of the new *residual* vector

$$\mathbf{X}^{(i+1)}[l] \triangleq \mathbf{X}^{(i)}[l] - \mathbf{C}_{X_0}^{(i)}[l]. \tag{62}$$

STDAEC-S3) *Residual energy test* – The energy

$$E^{(i+1)}[l] \triangleq \left\|\mathbf{X}^{(i+1)}[l]\right\|^2 = \sum_{p=0}^{N_{\mathrm{VH}}-1}\sum_{q=0}^{N_{\mathrm{VV}}-1}\left|X_l^{(i+1)}[p,q]\right|^2 \tag{63}$$

of the residual spectrum vector $\mathbf{X}^{(i+1)}[l]$ (62) is compared with the positive threshold T_{STDAEC} (which may depend on angular coordinates). If this energy is below the threshold, the STDAEC algorithm stops; otherwise, the recursion index i is increased by one and a new iteration is started by going back to **STDAEC-S1**. If $D[l]$ iterations are accomplished by the STDAEC algorithm operating on the $\hat{\alpha}_l$-th frequency bin, no more than $D[l]$ distinct targets are identified in that bin ($D[l]$ targets are found if none of them is deemed to be a ghost target). All the targets information acquired from the $\hat{\alpha}_l$-th frequency bin are collected in the set $\mathcal{T}_l$ (32).

T3-S2) *Evaluation of the target spatial coordinates and generation of the overall image* – In this step, the estimates of the range, of the elevation and of the azimuth of the i-th target detected in the $\hat{\alpha}_l$-th frequency bin are computed as (see (19), (37) and (38))

$$\hat{R}_i[l] = \frac{c}{2\mu}\hat{f}_i[l], \tag{64}$$

$$\hat{\phi}_i[l] = \arcsin\left(\frac{\lambda}{2d_{\mathrm{VV}}}\hat{F}_{\mathrm{V},i}[l]\right) \tag{65}$$

and

$$\hat{\theta}_i[l] = \arcsin\left(\frac{\lambda}{2d_{\mathrm{VH}}\cos(\hat{\phi}_i[l])}\hat{F}_{\mathrm{H},i}[l]\right), \tag{66}$$

respectively; here, $\hat{f}_i[l] = F_i[l]f_s$ (see (8)). Finally, these information are fused to generate the overall set $\mathcal{I}_t$ (25), describing the generated radar image; in general, this image is a cloud of $\hat{L}$ points. The set $\mathcal{I}_t$ (25) results from the union of all the sets $\{\mathcal{I}_t^{(l)}\}$, where

$$\mathcal{I}_t^{(l)} \triangleq \left\{\left(\hat{R}_i[l], \hat{\theta}_i[l], \hat{\phi}_i[l], \left|\hat{C}_i[l]\right|\right); i = 0, 1, \ldots, D[l]-1\right\}, \tag{67}$$

with $l = 0, 1, \ldots, L_b - 1$.

This concludes our description of the RASCA-FR3.

Let us focus now on the most complicated part of the STDAEC algorithm, i.e. on the STDAE algorithm. This algorithm makes use of the so called *spatial folding* (see the previous paragraph). The exploitation of this procedure in the STDAE algorithm requires:

1) Selecting a *reference* VULA, that consists of N_{VULA} adjacent and vertically aligned VAs (with $N_{\mathrm{VULA}} \leq N_{\mathrm{VV}}$), within the virtual array; in the following, we assume, without any loss of generality, that the reference VULA includes the reference antenna and, consequently, is identified by $p = p_R$ and $q = q_I, q_I + 1, \ldots, q_F$ (with $q_I \leq q_R \leq q_F$), so that $N_{\mathrm{VULA}} = q_F - q_I + 1$ (see Fig. 6a).
2) Selecting a *reference* HULA, that consists of N_{HULA} adjacent and horizontally aligned VAs; in the following, we assume, without any loss of generality, that the reference HULA is the horizontal ULA containing the reference antenna and, consequently, is identified by $p = p_I, p_I + 1, \ldots, p_F$ (with $p_I \leq p_R \leq p_F$) and $q = q_R$, so that $N_{\mathrm{HULA}} = p_F - p_I + 1$ (see Fig. 6a).
3) Selecting a set of HULAs, different from the reference HULA and having the same size of it (i.e., the same number of VAs); in the following, we assume, without any loss of generality, that these HULAs, called *vertically folded* HULAs, correspond to $q = q_I^{(\mathrm{VF})}, q_I^{(\mathrm{VF})} + 1, \ldots, q_R - 1, q_R + 1, \ldots, q_F^{(\mathrm{VF})}$, with $q_I^{(\mathrm{VF})} < q_R < q_F^{(\mathrm{VF})}$, as illustrated in Fig. 6b; note that the overall number of involved HULAs is $N_{\mathrm{HULA}}^{(\mathrm{VF})} = q_F^{(\mathrm{VF})} - q_I^{(\mathrm{VF})} + 1$.

The STDAE algorithm consists in the four steps described below (its r-th step is denoted STDAE-Sr in the following).

STDAE-S1) FFT *processing on the reference* VULA *and vertical frequency estimation* – The portion of the initial spectral information referring to the reference VULA is extracted from the matrix $\mathbf{X}^{(i)}[l]$ and stored in the N_{VULA} -dimensional vector

$$\mathbf{S}_{\mathrm{VULA},0}^{(i)}[l] = \left[S_{0,0}^{(i)}[l], S_{0,1}^{(i)}[l], \ldots, S_{0,N_{\mathrm{VULA}}-1}^{(i)}[l]\right]^T \triangleq \left[X_l^{(i)}[p_R, q_I], \ldots, X_l^{(i)}[p_R, q_F]\right]^T, \tag{68}$$

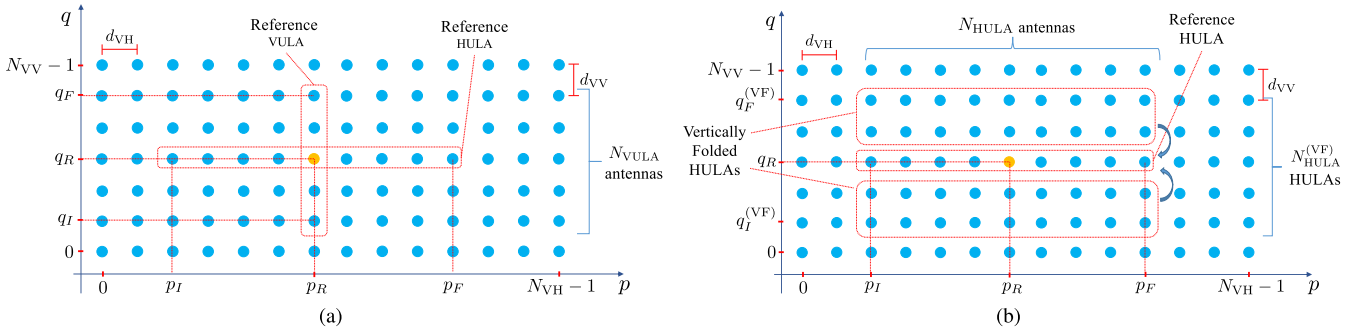

FIGURE 6. Example of reference VULA and reference HULA including the reference antenna (a) and representation of a set of vertically folded HULAs (b).

that is processed by the *complex single frequency estimator*[7] (CSFE). This algorithm detects the i-th (strongest target) appearing in $\hat{\alpha}_l$-th frequency bin and computes the estimates $\hat{C}_{\mathrm{V},i}[l]$ and $\hat{F}_{\mathrm{V},i}[l]$ of the parameters $C_i[l]$ and $F_{\mathrm{V},i}[l]$ (see (36)), respectively. Note that the quantity $\hat{C}_{\mathrm{V},i}[l]$ is not exploited in the following since, it represents a *preliminary estimate* of $C_i[l]$.

It is worth pointing out that the execution of the CSFE entails:

a) The evaluation of the N_{VULA}-dimensional vector

$$\mathbf{S}^{(i)}_{\mathrm{VULA},k}[l] \triangleq \left[S^{(i)}_{k,0}[l], S^{(i)}_{k,1}[l], \ldots, S^{(i)}_{k,N_{\mathrm{VULA}}-1}[l]\right]^T, \quad (69)$$

with $k = 1$ and 2; here,

$$S^{(i)}_{k,p}[l] \triangleq p^k\, X^{(i)}_{\mathrm{VULA},p}[l] = p^k\, X^{(i)}_l[p_R, q_I + p] \quad (70)$$

with $p = 0, 1, \ldots, N_{\mathrm{VULA}} - 1$.

b) The computation of an $\bar{N}_0$ order FFT of the vector $\bar{\mathbf{S}}^{(i)}_{\mathrm{VULA},k}[l]$, that represents a zero padded version of the vector $\mathbf{S}^{(i)}_{\mathrm{VULA},k}[l]$ (with $k = 0$, 1 and 2); here,

$$\bar{N}_0 \triangleq \bar{M} \cdot N_{\mathrm{VULA}} \quad (71)$$

and $\bar{M}$ represents the adopted oversampling factor. This produces the vector

$$\begin{aligned}\mathbf{s}^{(i)}_{\mathrm{VULA},k}[l] &= \left[s^{(i)}_{k,0}[l], s^{(i)}_{k,1}[l], \ldots, s^{(i)}_{k,\bar{N}_0-1}[l]\right]^T \\ &\triangleq \mathrm{DFT}_{\bar{N}_0}\left[\bar{\mathbf{S}}^{(i)}_{\mathrm{VULA},k}[l]\right], \end{aligned} \quad (72)$$

with $k = 0$, 1 and 2. Note that the m-th element of the vector $\mathbf{s}^{(i)}_{\mathrm{VULA},k}[l]$ can be expressed as

$$s^{(i)}_{k,m}[l] \triangleq \frac{1}{N_{\mathrm{VULA}}} \sum_{p=0}^{N_{\mathrm{VULA}}-1} S^{(i)}_{k,p}[l] \exp\left(-j\frac{2\pi pm}{\bar{N}_0}\right), \quad (73)$$

with $m = 0, 1, \ldots, \bar{N}_0 - 1$.

STDAE-S2) *Vertical folding* – The estimate $\hat{F}_{\mathrm{V},i}[l]$ of the normalised vertical frequency $F_{\mathrm{V},i}[l]$ (36) is employed to compensate for the phase difference between each of the HULAs selected for vertical folding and the reference HULA (i.e., for the phase differences along the *vertical* direction), so that the spectral information associated with all these HULAs can be combined (i.e., summed) in a constructive fashion. To this aim, the *phase rotation factor*

$$R^{(\mathrm{VF})}_i[l, q] \triangleq \left[\exp\left(-j\Delta\psi^{(\mathrm{VF})}_i[l]\right)\right]^{q-q_R}, \quad (74)$$

with

$$\Delta\psi^{(\mathrm{VF})}_i[l] \triangleq 2\pi\hat{F}_{\mathrm{V},i}[l], \quad (75)$$

is computed for the q-th HULA, with $q = q_I^{(\mathrm{VF})}, q_I^{(\mathrm{VF})} + 1, \ldots, q_R - 1, q_R + 1, \ldots, q_F^{(\mathrm{VF})}$. Then, vertical folding is accomplished by computing the N_{HULA} -dimensional vector

$$\mathbf{X}^{(\mathrm{VF})}_i[l] = \mathbf{X}^{(i)}[l, q_R] + \sum_{\substack{q=q_I^{(\mathrm{VF})} \\ q\neq q_R}}^{q_F^{(\mathrm{VF})}} \mathbf{X}^{(i)}[l, q]\; R^{(\mathrm{VF})}_i[l, q], \quad (76)$$

that collects the values taken on by the N_{HULA} vertically folded spectra referring to the $\hat{\alpha}_l$-th frequency bin; here,

$$\begin{aligned}&\mathbf{X}^{(i)}[l, q] \\ &\triangleq \left[X^{(i)}_l[p_I, q], X^{(i)}_l[p_I + 1, q], \ldots, X^{(i)}_l[p_F, q]\right]^T, \end{aligned} \quad (77)$$

is a N_{HULA}-dimensional row vector extracted from the q-th row of the matrix $\mathbf{X}^{(i)}[l]$ (61).

STDAE-S3) FFT *processing and horizontal frequency estimation* – The processing accomplished in this step is very similar to that carried out in **STDAE-S1**. In fact, the only difference is represented by the fact that the N_{VULA}-dimensional vector $\mathbf{S}^{(i)}_{\mathrm{VULA},0}[l]$ (68) is replaced by the N_{HULA}-dimensional vector $\mathbf{X}^{(\mathrm{VF})}_i[l]$ (76) generated in the previous step. Therefore, in this case, the CSFE algorithm is exploited to compute the estimate $\hat{F}_{\mathrm{H},i}[l]$ of the horizontal frequency $F_{\mathrm{H},i}[l]$ (35) and a new estimate, denoted $\hat{C}_{\mathrm{H},i}[l]$, of the complex amplitude $C_i[l]$ associated with the i-th target. Note that: a) in general, an order different from $\bar{N}_0$ (71) can be selected for the three DFTs computed by the CSFE algorithm in this step; b) the quantity $\hat{C}_{\mathrm{H},i}[l]$ is not exploited in the following since, it represents a preliminary estimate of $C_i[l]$;

[7] A detailed description of this estimator is provided in Paragraph VI-B. Note that this algorithm represents the complex counterpart of the SFE, in the sense that the former is fed by a complex sequence, whereas the latter by a real one.

c) the estimates $\hat{C}_{\mathrm{V},i}[l]$ and $\hat{C}_{\mathrm{H},i}[l]$ can be significantly different if multiple targets having similar horizontal frequencies or similar vertical frequencies contribute to the considered frequency bin.

STDAE-S4) *Overall folding and frequency/amplitude estimation* – In this step, the angular information i.e., the frequencies $\hat{F}_{\mathrm{V},i}[l]$ and $\hat{F}_{\mathrm{H},i}[l]$ computed in **STDAE-S2** and **STDAE-S3**, respectively, are exploited to accomplish overall folding[8]; this step involves the whole spectrum computed on the selected VAs. If the whole receive antenna array is exploited, overall folding consists in computing the N_0-dimensional vector

$$\mathbf{X}_{0,\mathrm{OF}}[l] \triangleq \sum_{p=0}^{N_{\mathrm{VH}}-1} \sum_{q=0}^{N_{\mathrm{VV}}-1} \mathbf{X}_0[p,q]\ R_i^{(\mathrm{HV})}[l,p,q], \quad (78)$$

where

$$R_i^{(\mathrm{HV})}[l,p,q] \triangleq R_i^{(\mathrm{VF})}[l,q]\ R_i^{(\mathrm{HF})}[l,p] \quad (79)$$

is a phase rotation factor, $R_i^{(\mathrm{VF})}[l,q]$ is expressed by (74),

$$R_i^{(\mathrm{HF})}[l,p] \triangleq \left[\exp\left(-j\Delta\psi_i^{(\mathrm{HF})}[l]\right)\right]^{p-p_R} \quad (80)$$

and

$$\Delta\psi_i^{(\mathrm{HF})}[l] \triangleq 2\pi\hat{F}_{\mathrm{H},i}[l]; \quad (81)$$

note that $R_i^{(\mathrm{HV})}[l,p,q] = 1$ if $p = p_R$ and $q = q_R$. Given $\mathbf{X}_{0,\mathrm{OF}}[l]$ (78), the sequence of the absolute values of its elements is analysed to verify the presence of a peak in the $\hat{\alpha}_l$-th frequency bin or in a bin close to it. To this aim, after evaluating

$$\hat{\alpha}_{\mathrm{OF}} \triangleq \arg \max_{\tilde{a}\in\{0,1,\ldots,N_0-1\}} \left|\mathbf{X}_{0,\mathrm{OF}}[\tilde{a}]\right|, \quad (82)$$

the quantity $d_{\hat{\alpha}}[l] \triangleq |\hat{\alpha}_{\mathrm{OF}} - \hat{\alpha}_l|$ is compared with the positive threshold T_{OF}. If $d_{\hat{\alpha}}[l]$ exceeds T_{OF}, the presence of a ghost target is detected; otherwise, the N_0-dimensional vector

$$\mathbf{X}_{m,\mathrm{OF}}[l] \triangleq \sum_{p=0}^{N_{\mathrm{VH}}-1} \sum_{q=0}^{N_{\mathrm{VV}}-1} \mathbf{X}_m[p,q]\ R_i^{(\mathrm{HV})}[l,p,q], \quad (83)$$

is computed for $m = 1$ and 2, and the CSFE algorithm[9] is run to estimate, on the basis of the triad ($\mathbf{X}_{0,\mathrm{OF}}[l]$, $\mathbf{X}_{1,\mathrm{OF}}[l]$, $\mathbf{X}_{2,\mathrm{OF}}[l]$), the *final estimates* $\hat{F}_i[l]$ and $\hat{C}_i[l]$ of the parameters $F_i[l]$ and $C_i[l]$, respectively; these parameters characterize the i-th target detected in the $\hat{\alpha}_l$-th frequency bin. Note that the integer part (see (51))

$$\hat{\alpha}_i[l] \triangleq \left\lfloor \hat{F}_i[l]/F_{\mathrm{DFT}} \right\rfloor \quad (84)$$

of $\hat{F}_i[l]$ does not necessarily coincide with $\hat{\alpha}_l$ but, if it differs, it is certainly close to $\hat{\alpha}_l$. If $\hat{\alpha}_i[l]$ is different from $\hat{\alpha}_l$ and appears in one of the couples forming the set $\mathcal{S}_{\mathrm{RPE}}$ (31), it is discarded, because the corresponding frequency bin is already being analysed by one of the other STDAEC algorithms. Otherwise, the new couple

$$\left(\hat{\alpha}_i[l], E_{b,L_b}\right), \quad (85)$$

where $E_{b,L_b} \triangleq |\hat{C}_i[l]|^2$, is added to the set $\mathcal{S}_{\mathrm{RPE}}$ and the number of its elements (i.e., L_b) is increased by one. This means that an additional STDAEC algorithm is run on the (new) $\hat{\alpha}_i[l]$-th bin.

This concludes our description of the STDAE algorithm and, consequently, of the RASCA-FR3, whose overall structure is summarised in Algorithm 1.

The RASCA-FC3 can be easily obtained from RASCA-FR3 by: a) replacing $C_i^{(v_k)}$ and $\hat{C}_i^{(v_k)}$ with $A_i^{(v_k)}$ and $\hat{A}_i^{(v_k)}$, respectively (see **STDREC-S1**); b) replacing the SFE with the CSFE in **STDREC-S1**; c) computing the vectors of the triad ($\mathbf{C}_{X_0}^{(v_k)}[i]$, $\mathbf{C}_{X_1}^{(v_k)}[i]$, $\mathbf{C}_{X_2}^{(v_k)}[i]$) on the basis of (140)–(142) (see Paragraph VI-D) in **STDREC-S2**; d) replacing $C_i[l]$ and $\hat{C}_i[l]$ with $\hat{A}_i[l]$ and $A_i[l]$, respectively (see **STDAEC-S1**); e) replacing $\hat{C}_{\mathrm{V},i}[l]$ and $\hat{C}_{\mathrm{H},i}[l]$ with $\hat{A}_{\mathrm{V},i}[l]$ and $\hat{A}_{\mathrm{H},i}[l]$, respectively (see **STDAE-S1** and **STDAE-S3**).

4) ADDITIONAL COMMENTS

The structure of the RASCA-FR3 (RASCA-FC3) deserves a number of comments, that are listed below for the different tasks and the steps they consist of.

T1 – In this task, each of the vectors $\{\mathbf{X}_0^{(v)}, \mathbf{X}_1^{(v)}, \mathbf{X}_2^{(v)}\}$ is computed by executing a N_0 order FFT. The vector $\mathbf{X}_0^{(v)}$ collects N_0 equally spaced samples of the spectrum of the sequence $\{x_{z,n}^{(v)}\}$ acquired on the v-th VA (see (42), (47) and (18)). The vectors $\mathbf{X}_1^{(v)}$ and $\mathbf{X}_2^{(v)}$, instead, consist of, up to a scale factor, N_0 equally spaced samples of the *first* and the *second derivatives*, respectively, of the same spectrum.

T2-S1 – The exploitation of a subset of the available antennas is motivated by the need of reducing the computational effort required by **T2** as much as possible. The adoption of a *deterministic* method for the selection of N_A antennas (with $N_A < N_{\mathrm{VR}}$) is not recommended. In fact, when multiple consecutive snapshots are processed to generate independent images, randomly changing the subset of N_A antennas from snapshot to snapshot allows the considered radar system to benefit from *antenna diversity*.

T2-S2 – The STDREC algorithm deserves the following comments:

a) The availability of *accurate* estimates of the normalised frequency $F_i^{(v_k)}$ and of the complex amplitude $C_i^{(v_k)}$ ($A_i^{(v_k)}$) (see (7) and (13)) plays an important role in this step, since these parameters are exploited in the serial cancellation procedure based on (53). In particular, ignoring the frequency residual $\delta_i^{(v_k)}$ of the normalised frequency $F_i^{(v_k)}$ (50) in this procedure (i.e., assuming that $\hat{F}_i^{(v_k)} = \hat{\alpha}_i^{(v_k)}$;

[8] As already mentioned above, a portion of the whole virtual array can be exploited to mitigate the impact of the estimation errors affecting these spatial frequencies.

[9] Note that our general description of the CSFE includes the computation of three order N_0 DFTs, that, in this case, are already available, being represented by $\{\mathbf{X}_{m,\mathrm{OF}}[l]; m = 0, 1, 2\}$.

Algorithm 1: *Range & Angle Serial Cancellation Algorithm* for an FMCW Radar System (Real Case)

T1 – FFT Processing:
Compute the vectors $\mathbf{x}_{0,\mathrm{ZP}}^{(v)}$, $\mathbf{x}_{1,\mathrm{ZP}}^{(v)}$ and $\mathbf{x}_{2,\mathrm{ZP}}^{(v)}$ according to (43)–(45); then, compute the triad $\{\mathbf{X}_0^{(v)}, \mathbf{X}_1^{(v)}, \mathbf{X}_2^{(v)}\}$ according to (47).

T2 – RPE:
S1) Extract N_A VAs from all the available VAs; then, build the set $\bar{\mathcal{S}}_{\mathrm{FFT}}$ (28).
for $k = 0$ *to* $N_A - 1$ **do**
  S2) Set $\mathbf{X}_m^{(v_k)}[0] \triangleq \mathbf{X}_m^{(v_k)}$ for $m = 0,\ 1,\ 2$ (see (49)); then, set the iteration index $i = 0$ and compute the initial energy $E_0^{(v_k)}$ according to (54).
  while $E_i^{(v_k)} > T_{\mathrm{STDREC}}$ **do**
    STDREC-S1) Compute the couple $(\hat{C}_i^{(v_k)}, \hat{F}_i^{(v_k)})$ running the SFE algorithm on the triad $(\mathbf{X}_0^{(v_k)}[i], \mathbf{X}_1^{(v_k)}[i], \mathbf{X}_2^{(v_k)}[i])$.
    STDREC-S2) Compute the vectors $(\mathbf{C}_{X_0}^{(v_k)}[i], \mathbf{C}_{X_1}^{(v_k)}[i], \mathbf{C}_{X_2}^{(v_k)}[i])$ according to (130)–(132); then, compute the new residual triad $(\mathbf{X}_0^{(v_k)}[i+1], \mathbf{X}_1^{(v_k)}[i+1], \mathbf{X}_2^{(v_k)}[i+1])$ according to (53).
    STDREC-S3) Compute the residual energy $E_{i+1}^{(v_k)}$ according to (54).
  end
end
S3) Build the set $\mathcal{S}_{\mathrm{RPE}}$ (31) (see (56) and (58)).

T3 – SPE:
S1) Set the iteration index $i = 0$ and set the initial vector $\mathbf{X}^{(0)}[l]$ according to (59); then, compute the initial energy $E^{(0)}[l]$ according to (63).
Parallel For $l = 0$ *to* $l = L_b - 1$ **do**
  while $E^{(i)}[l] > T_{\mathrm{STDAEC}}$ **do**
    STDAEC-S1) Compute the couple $(\hat{C}_{\mathrm{V},i}[l], \hat{F}_{\mathrm{V},i}[l])$ running the CSFE algorithm fed by the vector $\mathbf{S}_{\mathrm{VULA},0}^{(i)}[l]$ evaluated according to (68). Then, compute the phase rotation factor $R_i^{(\mathrm{VF})}[l, q]$ and the matrix $\mathbf{X}_i^{(\mathrm{VF})}[l]$ according to (74) and (76), respectively. Then, run the CSFE algorithm to compute the couple $(\hat{C}_{\mathrm{H},i}[l], \hat{F}_{\mathrm{H},i}[l])$ and compute the phase rotation factor $R_i^{(\mathrm{HF})}[l, p]$ according to (80). Finally, compute the vectors $\{\mathbf{X}_{m,\mathrm{OF}}[l];\ m = 0,\ 1,\ 2\}$ according to (78) and (83) and run the CSFE algorithm fed by the set $\{\mathbf{X}_{m,\mathrm{OF}}[l];\ m = 0,\ 1,\ 2\}$ to evaluate the couple $(\hat{C}_i[l], \hat{F}_i[l])$.
    STDAEC-S2) Compute the vector $\mathbf{C}_{X_0}^{(i)}[l]$ according to (144)–(145); then compute the new residual vector $\mathbf{X}^{(i+1)}[l]$ according to (62).
    STDAEC-S3) Compute the residual energy $E^{(i+1)}[l]$ according to (63).
  end
  S2) Compute $\hat{R}_i[l]$, $\hat{\phi}_i[l]$, $\hat{\theta}_i[l]$ according to (64)–(66).
end

see (51)) may result in a significant *error accumulation*.

b) A threshold on the maximum computational effort required by the STDREC algorithm can be set by requiring that the recursion index i never exceeds a fixed threshold; this is equivalent to limit the overall number of targets that can be detected on each VA.

c) The STDREC algorithm generates N_A different data sets; the k -th data set consists of the triads $\{(\hat{\alpha}_i^{(v_k)}, \hat{F}_i^{(v_k)}, \hat{C}_i^{(v_k)});\ i = 0, 1, \ldots, L_k - 1\}$ $(\{(\hat{\alpha}_i^{(v_k)}, \hat{F}_i^{(v_k)}, \hat{A}_i^{(v_k)});\ i = 0, 1, \ldots, L_k - 1\})$, characterizing the L_k targets detected on the v_k-th antenna (with $k = 0, 1, \ldots, N_A - 1$). Note that the overall number of targets may change from antenna to antenna, especially in the presence of extended targets; this is due to the fact that the signals acquired on different VAs can exhibit significant differences in their spectral content.

d) The following important interpretation of the processing accomplished by the STDREC algorithm on the v_k-th VA can be given. The vector $\mathbf{X}_0^{(v_k)}$ can be seen as a collection of noisy spectral information referring to N_0 distinct *frequency bins* (i.e., to N_0 distinct *range bins*) and is usually *dense* in the presence of multiple extended targets, as illustrated in Fig. 7-a) (where the absolute value of its elements is represented). The STDREC allows to extract a *discrete frequency* (i.e., *range*) *profile* from the vector $\mathbf{X}_0^{(v_k)}$, as illustrated in Fig. 7-b). In various real world scenarios, this profile turns out to be *sparse*, even in the presence of a dense vector $\mathbf{X}_0^{(v_k)}$; this is beneficial, since allows to concentrate the RPE computational effort on a set of *specific ranges*

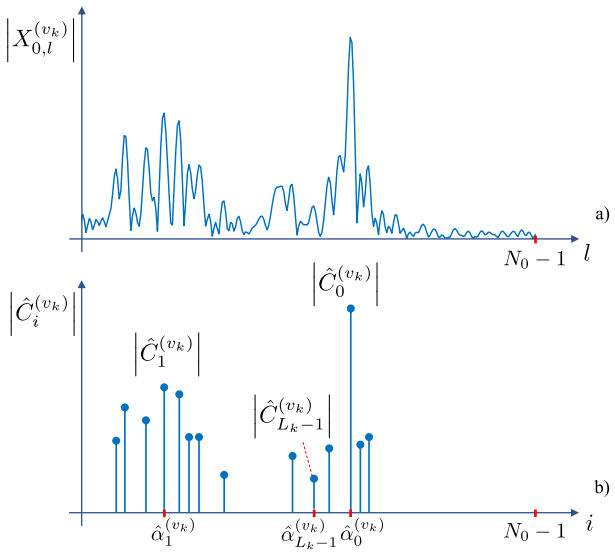

FIGURE 7. Representation of: a) the absolute value of the elements of the vector $\mathbf{x}_0^{(v_k)}$; b) the corresponding discrete amplitude-range profile generated by the STDREC algorithm (the RASCA-FC3 is considered).

(i.e., frequency bins). The *range profile* characterizing the v_k -th VA is described by the set of L_k couples $\mathcal{S}_{v_k} = \{(\hat{\alpha}_i^{(v_k)}, \hat{C}_i^{(v_k)}); i = 0, 1, \ldots, L_k - 1\}$ ($\mathcal{S}_{v_k} = \{(\hat{\alpha}_i^{(v_k)}, \hat{A}_i^{(v_k)}); i = 0, 1, \ldots, L_k - 1\}$), with $k = 0, 1, \ldots, N_A - 1$; the parameter $\hat{\alpha}_i^{(v_k)}$ identifies the frequency bin associated with the i-th target detected on the considered VA, whereas the absolute value of $\hat{C}_i^{(v_k)}$ ($\hat{A}_i^{(v_k)}$) represents an estimate of the *strength* of the echo associated with it.

e) The STDREC algorithm can be used for detecting multiple targets and accurately estimating their range in a monostatic radar.

f) The STDREC algorithm can be easily extended in a way that *multiple targets* are detected and estimated in parallel in each of its iterations. If we focus on its i-iteration and the v_k-th VA, this result is achieved by running multiple (say, $m_i^{(v_k)}$) instances of the SFE (CSFE) algorithm in parallel. Each of these instances is initialised with the frequency corresponding to the absolute maximum or a relative maximum detected in the sequence of the absolute values of the elements of the vector $\mathbf{X}_0^{(v_k)}[i]$ (see (47)). In this case, a constraint is set on the minimum spacing between the $m_i^{(v_k)}$ detected frequencies in order to minimize the interference between the instances running in parallel. Moreover, after identifying the absolute maximum in the above mentioned sequence, a threshold, proportional to such a maximum, is set on the minimum value of the acceptable relative maximum/maxima, so that unrelevant frequencies are discarded. It is also worth stressing that, if a *cluster* of $m_i^{(v_k)}$ distinct frequencies is estimated, each of the components of the triad ($\mathbf{C}_{X_0}^{(v_k)}[i]$, $\mathbf{C}_{X_1}^{(v_k)}[i]$, $\mathbf{C}_{X_2}^{(v_k)}[i]$) appearing in the RHS of (53) consists of the sum of $m_i^{(v_k)}$ terms, each associated with one of these frequencies.

g) The STDREC algorithm employed in the RASCA-FR3 (RASCA-FC3) represents an instance of the *single frequency estimation and cancellation* (*complex single frequency estimation and cancellation*) algorithm derived in [10] for the estimation of multiple overlapped *real* (*complex*) tones. For this reason, in the case of complex received signals, it can be replaced by one of the *multiple tone estimators* available in the technical literature, like the CFH algorithm [22], the algorithm developed by Ye and Aboutanios [23], [24] and the algorithm derived by Serbes [25] (the last two algorithms are denoted Alg-YA and Alg-S, respectively, in the following). In fact, all these algorithms are recursive and rely on a serial cancellation procedure since, within each recursion, they detect a single tone, estimate its parameters and subtract its contribution from the residual signal emerging from the previous iteration.

h) The estimates generated by the STDREC algorithm are potentially biased if the parameters of the SFE (CSFE) executed in its first step are not properly selected (see [10]). In principle, this bias can be arbitrarily reduced by increasing the overall number of iterations and/or re-estimations accomplished by the SFE (CSFE). However, we found out that, in the case of complex received signal, a computationally efficient alternative to this approach is represented by running an additional step (i.e., STDREC-S4) after that the first three steps of the STDREC algorithm has been carried out. In this final step, the Alg-YA is run after initializing it with the estimates of the normalised frequencies and the associated complex amplitudes generated by the STDREC. The hybrid technique that results from interconnecting the STDREC algorithm with the above mentioned algorithm is dubbed *hybrid* STDREC (HSTDREC) in the following; note that this algorithm represents an instance of the hybrid CSFE proposed in [10].

T3-S1 – This step is the most complicated of the whole algorithm and deserves the following comments:

a) In principle, the horizontal and vertical spatial frequencies (see (35) and (36)) of multiple targets contributing to the $\hat{\alpha}_l$-th frequency bin can be detected by first computing a 2D DFT of the matrix $\mathbf{X}[l]$ (60) and, then, by looking for local maxima over the absolute values of the elements of the resulting 2D matrix; note that the matrix $\mathbf{X}[l]$ can be also zero-padded before computing its 2D FFT to improve the resulting spectral resolution. This procedure may require a significant compu-

tational effort and its accuracy is affected by the spectral leakage due to any potential strong target. In the STDAEC algorithm, instead, 2D processing is avoided by alternating vertical and horizontal 1D FFTs. Consequently, relevant spatial frequencies are estimated by searching for the peaks of 1D amplitude spectra (i.e., in the absolute values of the elements of the vectors $\mathbf{S}^{(i)}_{\mathrm{VULA},0}[l]$ and $\mathbf{X}^{(\mathrm{VF})}_{i}[l]$); in other words, an AM approach is adopted. Note that this approach allow us to mitigate the overall computational complexity and to detect weak targets hidden by close strong targets through successive cancellations.

b) In **STDAE-S1**, each of the three vectors $\{\mathbf{s}^{(i)}_{\mathrm{VULA},k}[l]; k = 0, 1, 2\}$ is computed by executing a $\bar{N}_0$ order FFT (see (72)). Note that, on the one hand, the vector $\mathbf{s}^{(i)}_{\mathrm{VULA},0}[l]$ collects $\bar{N}_0$ equally spaced samples of the spectrum of the sequence $\{X^{(i)}_{\mathrm{VULA},p}; p = 0, 1, \ldots, N_{\mathrm{VULA}} - 1\}$ (see (70)). On the other hand, the k-th vector $\mathbf{s}^{(i)}_{\mathrm{VULA},k}[l]$ (with $k = 1$ and 2) collects, up to a scale factor, N_0 equally spaced samples of the k-th order derivative of the same spectrum.

c) The processing accomplished in **STDAE-S3** is very similar to that carried out in **STDAE-S1**. In fact, the only difference is represented by the fact that the N_{VULA}-dimensional vector $\mathbf{S}^{(i)}_{\mathrm{VULA},0}[l]$ (68) is replaced by the N_{HULA}-dimensional vector $\mathbf{X}^{(\mathrm{VF})}_{i}[l]$ (76) generated in **STDAE-S2**. Therefore, in this case, the CSFE is exploited to estimate the horizontal frequency $F_{\mathrm{H},i}[l]$ and, again, the complex amplitude $C_i[l]$ ($A_i[l]$) associated with the i-th target.

d) Similarly as the STDREC algorithm, the STDAEC algorithm can also be considered as an instance of the CSFEC algorithm mentioned at point g) of **T2-S2**. Therefore, in principle, it can be replaced by the CFH algorithm [22], the Alg-YA [23], [24] or the Alg-S [25]. Moreover, a further (and final) step, based the Alg-YA can be added to the STDAEC algorithm to mitigate its estimation bias.

e) As already suggested for the STDREC algorithm, the STDAEC algorithm can be employed to detect and estimate multiple angles in parallel; this requires running multiple instances of the CSFE algorithm in parallel.

Our final comments concern the use of RASCA-FR3 and RASCA-FC3 in FMCW radar systems whose virtual antenna array is not an URA; for instance, in our experimental work (see Section X), a colocated MIMO FMCW radar equipped with the virtual receive array shown in Fig. 8 has been employed. Note that the first two processing tasks of the RASCAs are carried out on an antenna-by-antenna basis; therefore, they are not influenced by the shape of the considered virtual array. However, this shape influences the way spatial folding is accomplished in **T3**. More specifically, as far as the last point is concerned, the following considerations can be made:

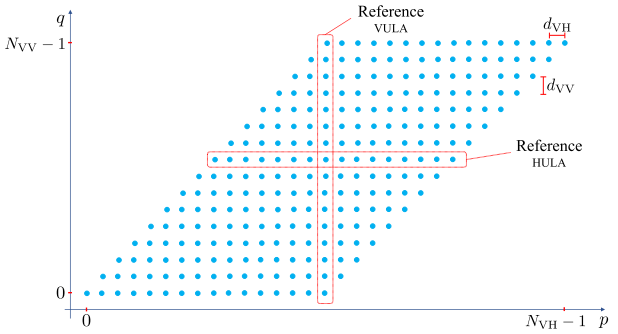

FIGURE 8. Virtual array considered in our experimental work.

1) The array structure represented in Fig. 8 can be treated as an URA if its gaps are zero-padded.

2) The reference VULA should be selected in a way to maximize the number of non-zero vertically aligned VAs and, consequently, the number of VAs contributing to the estimation of the elevation angle, as illustrated in Fig. 8.

3) The reference HULA should be selected in the middle of the antenna array; this mitigates the effects of the errors affecting the estimate of normalised vertical frequency in the vertical folding procedure (do not forget that such errors may have a significant impact on the contributions of the HULAs that are farther from the reference HULA; see (74)).

4) The vertical folding accomplished by the STDAE algorithm involves VULAs of different sizes. More specifically, in the i-th iteration of the STDAEC algorithm, vertical folding is accomplished by computing the N_{HULA}-dimensional vector (see (61) and **STDAE-S2**)

$$\mathbf{X}^{(\mathrm{VF})}_{i}[l] = \left[X^{(\mathrm{VF})}_{i}[p_I, l], X^{(i)}_{l}[p_I + 1, l], \ldots, X^{(i)}_{l}[p_F, l]\right]^T \tag{86}$$

where

$$X^{(\mathrm{VF})}_{i}[p, l] = \frac{1}{N_V[p]} \sum_{\substack{q=q_I[p] \\ q \neq q_R}}^{q_F[p]} X^{(i)}_{l}[p, q]\ R^{(\mathrm{VF})}_{i}[l, q] + \frac{X^{(i)}_{l}[p, q_R]}{N_V[p]}, \tag{87}$$

with $p = p_I, p_I + 1, \ldots, p_F$; here, $R^{(\mathrm{VF})}_{i}[l, q]$ is expressed by (74), $q_I[p]$ ($q_F[p]$) is the index identifying the first (last) antenna of the p-th VULA and $N_{\mathrm{V}}[p]$ is the overall number of VAs which that VULA consists of.

D. RANGE & ANGLE SERIAL CANCELLATION ALGORITHMS FOR A RADAR SYSTEM ENDOWED WITH A ONE-DIMENSIONAL ANTENNA ARRAY

The algorithms described in the previous paragraph can be easily adapted to the case in which the considered colocated

MIMO radar system is equipped with a single ULA and, consequently, can be exploited for 2D imaging only; this leads to RASCA-FR2 and RASCA-FC2. The changes made in RASCA-FR3 and RASCA-FC3 to obtain RASCA-FR2 and RASCA-FC2, respectively, concern only the SPE and can be summarized as follows:

1) The first three steps of the STDAE in **T3-S1** are not performed; therefore, the fourth step of that algorithm is the first one to be executed. Moreover, the matrix $\mathbf{X}^{(i)}[l]$ (61) is replaced by the N_{VH}-dimensional vector

$$\mathbf{X}^{(i)}[l] \triangleq \left[X_l^{(i)}[p]\right], \tag{88}$$

collecting the spectral information available on the whole virtual receive array and referring to the $\hat{\alpha}_l$-th frequency bin only.

2) The spatial frequency $\hat{F}_{\mathrm{V},i}[l]$ is unavailable and, therefore, it is not included in the set $\mathcal{T}_l$ (32); note that the elevation angle $\hat{\phi}_i[l]$ (65) is not estimated in this case.

V. RANGE & ANGLE SERIAL CANCELLATION ALGORITHMS FOR A COLOCATED MIMO SFCW RADAR SYSTEM

In this paragraph we analyse the main changes that need to be introduced in the RASCA-FC2 and RASCA-FC3 described in the previous paragraph to adapt them to a MIMO SFCW radar system, i.e. to develop RASCA-S2 and RASCA-S3. Let us focus on RASCA-S3 first. As far as **T1** is concerned, the only required change is represented by the replacement of: a) the sequence $\{x_{c,n}^{(v)}\}$ (12) with the sequence $\{x_{c,n}^{(v)}\}$ (15); b) each FFT with an inverse FFT (IFFT). This means that the spectra $\{\mathbf{X}_0^{(v)}, \mathbf{X}_1^{(v)}, \mathbf{X}_2^{(v)}; v = 0, 1, \ldots, N_{\mathrm{VR}} - 1\}$ computed in **T1** (now dubbed **IFFT processing**) provide time domain information and, in particular, information about the impulse responses of the communication channels associated with all the available VAs. For this reason, frequency bins are replaced by bins in the time domain; such bins are called *delay bins* in the remaining part of this document.

The changes to be made in **T2** concern its second step (i.e., the STDREC algorithm), since the noisy measurements processed in this step are always complex (see (15) and (17)); the new structure of this step is summarized below.

T2-S2) *Target detection and range estimation* – In this step, that aims at detecting the most relevant targets on each of the N_A antennas, a minor change is required in the cancellation procedure with respect to its counterpart employed in the MIMO FMCW radar system. This is due to the fact that, as already stated above, the noisy measurements processed in a MIMO SFCW radar system are always represented by *complex* (frequency-domain) sequences.

The initialization of the STDREC algorithm remains unchanged: the triad $(\mathbf{X}_0^{(v_k)}[0], \mathbf{X}_1^{(v_k)}[0], \mathbf{X}_2^{(v_k)}[0])$ is defined according to (49) (with $k = 0, 1, \ldots, N_A - 1$). In its i-th iteration, this algorithm accomplishes the three steps described below (these are denoted STDREC-Sp in the following, with $p = 1,\ 2$ and 3).

STDREC-S1) *Detection of a new target and estimation of its parameters* – In this step, the normalised delay $F_i^{(v_k)}$ and the complex amplitude $A_i^{(v_k)}$ associated with the i-th target are estimated. Note that, generally speaking, the normalised delay $F_i^{(v_k)}$ is not a multiple of the *fundamental delay*

$$F_{\mathrm{IDFT}} = 1/N_0, \tag{89}$$

that characterizes the output of the IFFT processing executed in task **T1**; for this reason, it can be expressed as

$$F_i^{(v_k)} = F_{c,i}^{(v_k)} + \delta_i^{(v_k)} F_{\mathrm{IDFT}}, \tag{90}$$

where $F_{c,i}^{(v_k)}$ is a given *coarse estimate* of the normalised delay $F_i^{(v_k)}$ and $\delta_i^{(v_k)}$ is a real parameter called *residual*. The processing accomplished in this step is executed by an algorithm dubbed *complex single delay estimator* (CSDE) in the following (see Paragraph VI-C); this computes the estimates $\hat{A}_i^{(v_k)}$, $\hat{F}_{c,i}^{(v_k)}$,

$$\hat{\alpha}_i^{(v_k)} \triangleq \left\lfloor \hat{F}_{c,i}^{(v_k)} / F_{\mathrm{IDFT}} \right\rfloor \tag{91}$$

$$\hat{F}_i^{(v_k)} = \hat{F}_{c,i}^{(v_k)} + \hat{\delta}_i^{(v_k)} F_{\mathrm{IDFT}} \tag{92}$$

of the parameters $A_i^{(v_k)}$, $F_{c,i}^{(v_k)}$, $\alpha_i^{(v_k)}$ and $F_i^{(v_k)}$, respectively, on the basis of the triad $(\mathbf{X}_0^{(v_k)}[i], \mathbf{X}_1^{(v_k)}[i], \mathbf{X}_2^{(v_k)}[i])$.

STDREC-S2) *Cancellation of the new target* – The contributions $(\mathbf{C}_{X_0}^{(v_k)}[i], \mathbf{C}_{X_1}^{(v_k)}[i], \mathbf{C}_{X_2}^{(v_k)}[i])$ given by the i -th (i.e., by the last) target detected on the v_k-th VA to the triad $(\mathbf{X}_0^{(v_k)}[i], \mathbf{X}_1^{(v_k)}[i], \mathbf{X}_2^{(v_k)}[i])$, are computed on the basis of (146)–(148) (see Paragraph VI-E). Therefore, the cancellation procedure consists again in the computation of the new *residual* triad on the basis of (53).

STDREC-S3) *Computation of the residual energy in the time domain* – The energy of the residual time-domain vector $\mathbf{X}_0^{(v_k)}[i+1]$ is computed (see (54)) and compared with the positive threshold T_{STDREC}. If this energy is below the threshold, the STDREC algorithm stops and $L_k = i$ relevant targets are detected on the v_k-th VA; otherwise, the recursion index i is increased by one and a new recursion is started (i.e., we go back to **STDREC-S1**).

T2-S3) *Range information fusion* – In this case, the set $\mathcal{A}_b$ (see (56)) collects L_b relevant time bins $\{\hat{\alpha}_l; l = 0, 1, \ldots, L_b - 1\}$, whereas the set $\{E_{b,l}\}$ contains the energy associated with each of them (see (57)). The average energy $E_{b,l}$ associated with the $\hat{\alpha}_l$-th delay bin is evaluated as

$$E_{b,l} = \frac{1}{N_{b,l}} \sum_{k=0}^{N_A-1} \sum_{i=0}^{L_k-1} \left|\hat{A}_i^{(v_k)}\right|^2 \delta\left[\hat{\alpha}_i^{(v_k)} - \hat{\alpha}_l\right], \tag{93}$$

with $l = 0, 1, \ldots, L_b - 1$; here, $N_{b,l}$ is defined by (58). The final output of the information fusion is represented by the set $\mathcal{S}_{\mathrm{RPE}}$ (31). Note that the cardinality L_b of the last set represents a preliminary estimate of the overall number of targets.

The processing accomplished in **T3** (i.e., by the SPE) has the same structure and interpretation as that illustrated for the FMCW radar system since it aims at estimating the angular

parameters of the targets on the basis of the discrete range profile computed in **T2**. However, frequency bins are now replaced by delay bins. Note also that, in step **T3-S1**, the matrix $\mathbf{X}[l]$ is still defined on the basis of (60), but the complex amplitude $A_i[p, q, l]$ appearing in (34) is replaced by

$$A_i[p,q,l] = A_i[l] \exp\left[-j\frac{4\pi}{\lambda}\left[d_{\mathrm{VH}}\,(p-p_R)\cos(\phi_i[l])\right.\right. \\ \left.\left.\cdot \sin(\theta_i[l]) + d_{\mathrm{VV}}\,(q-q_R)\sin(\phi_i[l])\right]\right], \quad (94)$$

where $A_i[l]$ is the complex amplitude observed for the i-th target in the l-th time bin on the reference VA. This leads to some relevant differences in the formulas employed by the STDAE algorithm in the estimation of the parameters $\{\theta_i[l], \phi_i[l], F_i[l], A_i[l]\}$ (see **STDAEC-S1**) with respect to the case of a MIMO FMCW radar system. The modifications introduced in the STDAE processing are provided after illustrating the overall structure of the RASCA-S3 to ease reading.

STDAEC-S2) *Target cancellation* – The contribution $\mathbf{C}_{X_0}^{(i)}[l]$, given by the i-th target detected in the l-th time bin, to the vector $\mathbf{X}^{(i)}[l]$ is computed by means of (154) (see Paragraph VI-E) and is cancelled from $\mathbf{X}^{(i)}[l]$. Cancellation consists in the evaluation of the new residual according to (62).

STDAEC-S3) *Residual energy test* – In this step, the energy $E^{(i+1)}[l]$ of the residual $\mathbf{X}^{(i+1)}[l]$ evaluated in the previous step is computed on the basis of (63)) and is compared with a positive threshold; if this energy is below the threshold, the STDAEC algorithm stops, otherwise the recursion index i is increased by one and a new iteration is started by going back to **STDAEC-S1**.

All the target information acquired from the $\hat{\alpha}_l$-th frequency bin are collected in the set

$$\mathcal{T}_l \triangleq \left\{\left(\hat{A}_i[l], \hat{F}_i[l], \hat{\alpha}_i[l], \hat{F}_{V,i}[l], \hat{F}_{H,i}[l]\right); \right. \\ \left. i = 0, 1, \ldots, D[l]-1\right\} \quad (95)$$

with $l = 0, 1, \ldots, L_b - 1$; here, $D[l]$ denotes the overall number of targets detected in the considered bin. In **T3-S2** the evaluation of spatial coordinates $(\hat{R}_i[l], \hat{\phi}_i[l], \hat{\theta}_i[l])$ is accomplished in the same way as in the FMCW case, i.e. on the basis of (64)–(66). Finally, the available information are merged to generate the overall set $\mathcal{I}_t$ (25), which, generally speaking, can be represented as a cloud of $\hat{L}$ points; note that $\mathcal{I}_t$ results of the union of the sets $\{\mathcal{I}_t^{(l)}\}$ and that the set $\mathcal{I}_t^{(l)}$ is still defined according to (67).

This concludes our description of the RASCA-S3. Let us summarise now the four steps of the STDAE algorithm embedded in RASCA-S3.

STDAE-S1) IFFT *processing on the reference* VULA and vertical frequency estimation – In this step, the vector

$$\mathbf{s}_{\mathrm{VULA},k}^{(i)}[l] = \left[s_{k,0}^{(i)}[l], s_{k,1}^{(i)}[l], \ldots, s_{k,\bar{N}_0-1}^{(i)}[l]\right]^T \\ \triangleq \mathrm{IDFT}_{\bar{N}_0}\left[\bar{\mathbf{S}}_{\mathrm{VULA},k}^{(i)}[l]\right], \quad (96)$$

is evaluated by the CSDE algorithm (see Paragraph VI-C), for $k = 0$, 1 and 2; note that

$$s_{k,m}^{(i)}[l] \triangleq \frac{1}{N_{\mathrm{VULA}}}\sum_{p=0}^{N_{\mathrm{VULA}}-1} S_{k,p}^{(i)}[l]\exp\left(j\frac{2\pi pm}{\bar{N}_0}\right), \quad (97)$$

with $m = 0, 1, \ldots, \bar{N}_0 - 1$, and that the quantity $S_{k,p}^{(i)}[l]$ is still defined by (70). The CSDE algorithm produces the estimates $\hat{A}_{\mathrm{V},i}[l]$ and $\hat{F}_{\mathrm{V},i}[l]$ of $A_i[l]$ and $F_i[l]$, respectively.

STDAE-S2) *Vertical folding* – Vertical folding is employed to compensate for the phase differences between the considered HULAs. However, the *phase rotation factor* appearing in (76) is computed as

$$R_i^{(\mathrm{VF})}[l,q] \triangleq \left[\exp\left(j\Delta\psi_i^{(\mathrm{VF})}[l]\right)\right]^{q-q_R}, \quad (98)$$

where

$$\Delta\psi_i^{(\mathrm{VF})}[l] \triangleq 2\pi\hat{F}_{\mathrm{V},i}[l] \quad (99)$$

and $\hat{F}_{\mathrm{V},i}[l]$ is the estimate of the normalised vertical frequency $F_{\mathrm{V},i}[l]$ evaluated in **STDAE-S1**.

STDAE-S3) IFFT *processing and horizontal delay estimation* – In this step, the CSDE algorithm is executed to compute the estimates $\hat{F}_{\mathrm{H},i}[l]$ (35) and $\hat{A}_i[l]$ of the normalised horizontal frequency $F_{\mathrm{H},i}[l]$ and of the complex amplitude $A_i[l]$, respectively.

STDAE-S4) *Overall folding and delay/amplitude estimation* – In this step, the angular information (i.e., the normalised spatial frequencies $\hat{F}_{\mathrm{V},i}[l]$ and $\hat{F}_{\mathrm{H},i}[l]$) evaluated in the previous steps are exploited to apply folding to the whole receive antenna array or to a portion of it. Similarly as the case of a MIMO FMCW radar, overall folding requires the computation of the N_0 -dimensional vectors $\mathbf{X}_{0,\mathrm{OF}}[l]$, $\mathbf{X}_{1,\mathrm{OF}}[l]$ and $\mathbf{X}_{2,\mathrm{OF}}[l]$ (see (78)); the horizontal phase rotation $R_i^{(\mathrm{HF})}[l,p]$ appearing in the RHS of (79) is defined as

$$R_i^{(\mathrm{HF})}[l,p] \triangleq \left[\exp\left(j\Delta\psi_i^{(\mathrm{HF})}[l]\right)\right]^{p-p_R}, \quad (100)$$

where

$$\Delta\psi_i^{(\mathrm{HF})}[l] \triangleq 2\pi\hat{F}_{\mathrm{H},i}[l]. \quad (101)$$

If a peak is detected in the sequence made of the absolute values of the elements of $\mathbf{X}_{0,\mathrm{OF}}[l]$, the CSDE algorithm is run to estimate, on the basis of the vectors $\mathbf{X}_{0,\mathrm{OF}}[l]$, $\mathbf{X}_{1,\mathrm{OF}}[l]$ and $\mathbf{X}_{2,\mathrm{OF}}[l]$, the final estimates $\hat{F}_i[l]$ and $\hat{A}_i[l]$ of the parameters $F_i[l]$ and $A_i[l]$. Then, if the estimated normalised delay $\hat{F}_i[l]$ (see (90)) is close to $\hat{\alpha}_l$ and the quantity $\hat{\alpha}_i[l]$ appears in one of the couples of set $\mathcal{S}_{\mathrm{RPE}}$ (31), it is discarded. Otherwise, the new couple $(\hat{\alpha}_i[l], E_{b,L_b})$ (see (85)) is added to the set $\mathcal{S}_{\mathrm{RPE}}$ and the number of its elements (i.e., L_b) is increased by one.

The RASCA-S3 can be easily adapted to the case in which the radar system is equipped with a single ULA. The changes to be made are exactly the same as those illustrated in the previous paragraph for deriving RASCA-FR2 (RASCA-FC2) from RASCA-FR3 (RASCA-FC3).

VI. DESCRIPTION OF VARIOUS ALGORITHMS EMPLOYED IN THE PROPOSED EMBODIMENTS

In this section, various mathematical details about the techniques employed in the RASCAs are provided.

Since the processing accomplished in **T1** of the RASCAs has been fully analysed in the previous section, in this paragraph we provide a detailed description of: a) the SFE (see **T2-S2**); b) the CSFE (see **T2-S2** and **T3-S1**); c) the CSDE (see **T2-S2** and **T3-S1**); d) the target cancellation procedures employed in **T2-S3** and **T3-S1**.

A. SINGLE FREQUENCY ESTIMATOR

In this Paragraph, the SFE derived in [10] is summarized. This algorithm processes the samples of the real sequence $\{x_{r,n}; n = 0, 1, \ldots, N-1\}$, whose n-th element is

$$\begin{aligned} x_{r,n} &= a\cos(2\pi n F + \psi) + w_{r,n} \\ &= C\exp(j2\pi n F) + C^*\exp(-j2\pi n F) + w_{r,n}, \end{aligned} \quad (102)$$

with $n = 0, 1, \ldots, N-1$, and generates an estimate of the *normalised frequency* F and of the *complex amplitude*

$$C \triangleq \frac{1}{2} a\exp(j\psi) \quad (103)$$

of the real tone appearing in the RHS of (102); here, N is the overall number of elements of the sequence $\{x_{r,n}\}$, a and ψ are the tone amplitude and phase, respectively, and $\{w_{r,n}; n = 0, 1, \ldots, N-1\}$ is a real AWGN sequence. This algorithm is initialised by

1) Evaluating: a) the vector

$$\mathbf{X}_0 = \left[X_{0,0}, X_{0,1}^{(v)}, \ldots, X_{0,N_0-1}^{(v)}\right]^T \triangleq \mathrm{DFT}_{N_0}\left[\mathbf{x}_{0,\mathrm{ZP}}^{(v)}\right], \quad (104)$$

where the DFT order N_0 is defined by (46),

$$\mathbf{x}_{0,\mathrm{ZP}} \triangleq \left[(\mathbf{x}_0)^T \; \mathbf{0}_{(M-1)N}^T\right]^T, \quad (105)$$

M is the *oversampling factor* and

$$\mathbf{x}_0 \triangleq \left[x_{r,0}, x_{r,1}, \ldots, x_{r,N-1}\right]^T; \quad (106)$$

b) the initial coarse estimate $\hat{F}_c^{(0)}$ of F as

$$\hat{F}_c^{(0)} = \hat{\alpha}\, F_{\mathrm{DFT}}, \quad (107)$$

where the integer $\hat{\alpha}$ is computed as

$$\hat{\alpha} = \arg \max_{\tilde{\alpha}\in\{0,1,\ldots,N_0/2-1\}} \left|\bar{X}_{0,\tilde{\alpha}}\right|; \quad (108)$$

c) the quantity

$$\hat{\rho}^{(0)} \triangleq \frac{\hat{F}_c^{(0)}}{F_{\mathrm{DFT}}} = \hat{\alpha}; \quad (109)$$

d) the initial estimate $\hat{C}^{(0)}$ of C as

$$\hat{C}^{(0)} = G\left(\hat{F}_c^{(0)}\right) \quad (110)$$

where

$$G\left(\tilde{F}\right) \triangleq \frac{\bar{X}(\tilde{F}) - \bar{X}^*(\tilde{F})g(\tilde{F})}{1 - \left|g(\tilde{F})\right|^2}, \quad (111)$$

$$\bar{X}(\tilde{F}) \triangleq \frac{1}{N}\sum_{n=0}^{N-1} x_{r,n}\exp\left(-j2\pi n\tilde{F}\right) \quad (112)$$

and

$$g(\tilde{F}) \triangleq \frac{1}{N}\sum_{n=0}^{N-1} \exp\left(-j4\pi n\tilde{F}\right); \quad (113)$$

e) the spectral coefficients $\bar{X}_{1,\hat{\alpha}}$ and $\bar{X}_{2,\hat{\alpha}}$, and the coefficients $\{K_p(2\hat{\alpha});\ p = 1, 2\}$ and $\{b(\hat{\alpha}),\ c(\hat{\alpha})\}$ on the basis of the definitions

$$\bar{X}_{k,\rho} \triangleq \frac{1}{N}\sum_{n=0}^{N-1} x_{k,n}\exp\left(-j\frac{2\pi n\rho}{N_0}\right), \quad (114)$$

$$K_p(x) \triangleq \frac{1}{N}\sum_{n=0}^{N-1} g_p[n]\exp\left(-j\frac{2\pi nx}{N_0}\right), \quad (115)$$

$$b(\rho) \triangleq -\Re\left\{\hat{C}^*\bar{X}_{2,\rho}\right\} + 2\Re\left\{\left(\hat{C}^*\right)^2 K_2(2\rho)\right\} \quad (116)$$

and

$$c(\rho) \triangleq \Im\left\{\hat{C}^*\bar{X}_{1,\rho}\right\} - \Im\left\{\left(\hat{C}^*\right)^2 K_1(2\rho)\right\}, \quad (117)$$

respectively; f) the initial estimate $\hat{\Delta}^{(0)}$ of Δ as

$$\hat{\Delta}^{(0)} = P\left(\hat{\rho}^{(0)}\right), \quad (118)$$

where

$$P(\tilde{\rho}) \triangleq -c(\tilde{\rho})\,/\,b(\tilde{\rho}); \quad (119)$$

g) the first fine estimate $\hat{F}^{(0)}$ of F as

$$\hat{F}^{(0)} = \hat{F}_c^{(0)} + \frac{\hat{\Delta}^{(0)}}{2\pi} \quad (120)$$

2) Setting its iteration index i to 1.

Then, an iterative procedure is started. The i-th iteration is fed by the estimates $\hat{F}^{(i-1)}$ and $\hat{C}^{(i-1)}$ of F and C, respectively, and produces the new estimates $\hat{F}^{(i)}$ and $\hat{C}^{(i)}$ of the same quantities (with $i = 1, 2, \ldots, N_{\mathrm{SFE}}$, where N_{SFE} represents the overall number of iterations); the procedure employed for the evaluation of $\hat{F}^{(i)}$ and $\hat{C}^{(i)}$ consists of the two steps described below (the p-th step is denoted SFE-Sp).

SFE-S1) - The new estimate $\hat{\Delta}^{(i)}$ of Δ is computed as[10] (see (118)–(119))

$$\hat{\Delta}^{(i)} = P(\hat{\rho}^{(i-1)}) = -c\left(\hat{\rho}^{(i-1)}\right)/b\left(\hat{\rho}^{(i-1)}\right); \quad (121)$$

in the evaluation of the coefficients $\{b(\rho), c(\rho)\}$ appearing in the RHS of (119), $\hat{C} = \hat{C}^{(i-1)}$ and

$$\rho = \hat{\rho}^{(i-1)} \triangleq \hat{F}^{(i-1)}/F_{\mathrm{DFT}} \quad (122)$$

[10]The quantities $\{\bar{X}_{k,\rho}; k = 1, 2\}$ required in the computation of the coefficients $b(\rho)$ and $c(\rho)$ can be also evaluated by means of the interpolation-based method illustrated in [10, Sect. III, p. 12]. In our work, *barycentric interpolation* has been always used [26]; in the following, the parameter I represents the interpolation order. These considerations hold also for the CSFE and the CSDE described below.

are assumed. Then,

$$\hat{F}^{(i)} = \hat{F}^{(i-1)} + \hat{\Delta}^{(i)}/(2\pi) \tag{123}$$

is evaluated.

SFE-S2) - The new estimate $\hat{C}^{(i)}$ of $\hat{C}$ is evaluated as $\hat{C}^{(i)} = G(\hat{F}^{(i)})$ (see (110)–(111)). Moreover, the index i is incremented by one before starting the next iteration.

At the end of the last (i.e., of the N_{SFE}-th) iteration, the fine estimates $\hat{F} = \hat{F}^{(N_{\mathrm{SFE}})}$ and $\hat{C} = \hat{C}^{(N_{\mathrm{SFE}})}$ of F and C, respectively, become available.

B. COMPLEX SINGLE FREQUENCY ESTIMATOR

All the results illustrated in the previous paragraph refer to the real sequence $\{x_{r,n}\}$, whose n-th element is expressed by (102). However, a similar estimation method (namely, the CSFE) has been developed for the complex counterpart, i.e. for a complex sequence $\{x_{c,n};\ n = 0, 1, \ldots, N-1\}$, whose n-th element is

$$x_{c,n} = A \exp(j2\pi n F) + w_{c,n}, \tag{124}$$

with $n = 0, 1, \ldots, N-1$. Here, A is the complex amplitude of the single tone appearing in the RHS of the last equation, $\{w_{c,n};\ n = 0, 1, \ldots, N-1\}$ is a complex AWGN sequence and all the parameters have exactly the same meaning as that illustrated for (102). The description of the CSFE is similar to that illustrated for the SFE in the previous paragraph, the only differences being represented by the fact that: a) the parameter C (103) is replaced by A; b) (110) is replaced by

$$\tilde{A} = \hat{A} = \bar{X}(\hat{F}), \tag{125}$$

where $\bar{X}(\hat{F})$ is computed according to (112) (in which $x_{r,n}$ is replaced by $x_{c,n}$ (124)); c) (116) and (117) are replaced by

$$b(\rho) \triangleq \Re\{\hat{A}^* \bar{X}_{2,\rho}\} \tag{126}$$

and

$$c(\rho) \triangleq -\Im\{\hat{A}^* \bar{X}_{1,\rho}\}, \tag{127}$$

respectively.

C. COMPLEX SINGLE DELAY ESTIMATOR

The SFE (CSFE) described in Paragraph VI-A (VI-B) is fed by the real (complex) sequence $\{x_{r,n}\}$ ($\{x_{c,n}\}$), whose n-th element is expressed by (102) ((124)); as shown in Section II, these signal models are suitable to represent the sampled downconverted signal available at the receive side of a colocated FMCW MIMO radar in the presence of a single target (i.e., when $L = 1$). However, a similar estimation method, called CSDE, can be developed for a colocated SFCW MIMO radar system, since the complex (frequency-domain) signal model (15) characterizing this system is very similar to the complex (time-domain) signal model (12) illustrated for a FMCW radar system, the only differences being represented by: a) the physical meaning of the parameter $F_l^{(v)}$, since this represents a *normalised delay* in (15) and a *normalised frequency* in (12)); b) the sign of the argument of all the complex exponentials appearing in the RHS of (15), since this is the opposite of that of the corresponding functions contained in the RHS of (12).

The derivation of the CSDE follows the same line of reasoning as the CSFE. Moreover, the latter algorithm has the same structure as the former one, because of the similarity between the involved signal models. The few differences, originating from the above mentioned sign reversal, can be summarised as follows:

1) The vectors $\mathbf{X}_m^{(v)}$ (47) are generated by taking a N_0 order *inverse* DFT (IDFT) (in place of a N_0 order DFT) of the zero-padded vectors $\mathbf{x}_{0,\mathrm{ZP}}^{(v)}$ (43), $\mathbf{x}_{1,\mathrm{ZP}}^{(v)}$ (44) and $\mathbf{x}_{2,\mathrm{ZP}}^{(v)}$ (45), respectively.
2) The estimate $\hat{\Delta}^{(i)}$ of the delay residual Δ is evaluated on the basis of (121) and (119), where, however,

$$b(\hat{\rho}) \triangleq -\Re\{\hat{A}^* \bar{X}_{2,\hat{\rho}}\}, \tag{128}$$

and $\hat{A}$ is the estimate of the complex amplitude A computed on the basis of (125) (the coefficient $c(\hat{\rho})$, instead, is still expressed by (127)). Moreover, in the evaluation of the coefficients $\{b(\hat{\rho}), c(\hat{\rho})\}$, the quantity $\bar{X}_{k,\hat{\rho}}$ (114) is replaced by

$$\bar{X}_{k,\hat{\rho}} \triangleq \frac{1}{N} \sum_{n=0}^{N-1} x_{k,n} \exp\left(j \frac{2\pi n \hat{\rho}}{N_0}\right), \tag{129}$$

where $\hat{\rho}$ is still defined by (122).

Given the CSDE, the counterpart of the CSFEC algorithm, called *complex single delay estimation and cancellation* (CSDEC), can be easily developed.

D. TARGET CANCELLATION PROCEDURES EMPLOYED IN FMCW RADAR SYSTEMS

In **T2** of the RASCA-FR2 and RASCA-FR3 (and, in particular, in **STDREC-S2**; see (53)), a target cancellation procedure is used in combination with the SFE. This procedure requires the evaluation of the triad ($\mathbf{C}_{X_0}^{(v)}[i]$, $\mathbf{C}_{X_1}^{(v)}[i]$, $\mathbf{C}_{X_2}^{(v)}[i]$), that represents the contribution given by the i-th (i.e., by the last) *point target* detected on the v-th VA. If $\hat{F}_i^{(v)}$ and $\hat{C}_i^{(v)}$ denote the estimates of the normalised frequency and the complex amplitude, respectively, characterizing this target, the expressions

$$\mathbf{C}_{X_0}^{(v)}[i] = \hat{C}_i^{(v)}\, \bar{\mathbf{W}}_0^{(v)}[i] + \left(\hat{C}_i^{(v)}\right)^* \left(\bar{\mathbf{W}}_{0,c}^{(v)}[i]\right), \tag{130}$$

$$\mathbf{C}_{X_1}^{(v)}[i] = \hat{C}_i^{(v)}\, \bar{\mathbf{W}}_1^{(v)}[i] + \left(\hat{C}_i^{(v)}\right)^* \left(\bar{\mathbf{W}}_{1,c}^{(v)}[i]\right) \tag{131}$$

and

$$\mathbf{C}_{X_2}^{(v)}[i] = \hat{C}_i^{(v)}\, \bar{\mathbf{W}}_2^{(v)}[i] + \left(\hat{C}_i^{(v)}\right)^* \left(\bar{\mathbf{W}}_{2,c}^{(v)}[i]\right) \tag{132}$$

are employed; here, $\bar{\mathbf{W}}_k^{(v)}[i]$ denotes the N_0 order DFT of the vector

$$\bar{\mathbf{w}}_k^{(v)}[i] \triangleq \left[0, 1^k \cdot \bar{w}_i^{(v)}, 2^k \cdot \left(\bar{w}_i^{(v)}\right)^2, \ldots, (N-1)^k \cdot \left(\bar{w}_i^{(v)}\right)^{N-1}, 0, \ldots, 0\right]^T, \tag{133}$$

with $k = 0$, 1 and 2, $\bar{\mathbf{W}}_{k,c}^{(v)}[i]$ the N_0 order DFT of the vector $(\bar{\mathbf{w}}_k^{(v)}[i])^*$,

$$\bar{w}_i^{(v)} \triangleq \exp(j2\pi \bar{F}_i^{(v)}) \tag{134}$$

and

$$\bar{F}_i^{(v)} \triangleq \hat{f}_i^{(v)} T_s \tag{135}$$

is the normalised frequency associated with the frequency $\hat{f}_v^{(i)}$. It is important to point out that an efficient method can be used for the computation of the vectors $\bar{\mathbf{W}}_k^{(v)}[i]$ and $\bar{\mathbf{W}}_{k,c}^{(v)}[i]$ appearing in the RHS of (130)–(132) (with $k = 0$, 1 and 2); note that, for any k, these vectors represent the N_0 order DFTs of the sequences $\{n^k\ (\bar{w}_i^{(v)})^n;\ n = 0, 1, \ldots, N-1\}$ and $\{n^k\ ((\bar{w}_i^{(v)})^*)^n; n = 0, 1, \ldots, N-1\}$, respectively. In fact, the l-th element of the vectors $\bar{\mathbf{W}}_k^{(v)}[i]$ and $\bar{\mathbf{W}}_{k,c}^{(v)}[i]$ is given by

$$\begin{aligned}\bar{W}_k^{(v)}[i,l] &= \frac{1}{N}\sum_{n=0}^{N-1} n^k \left(\bar{w}_i^{(v)}\right)^n \exp\left(-j\frac{2\pi l}{N_0}n\right) \\ &= \frac{1}{N}\sum_{n=0}^{N-1} n^k (q[l])^n\end{aligned} \tag{136}$$

and

$$\begin{aligned}\bar{W}_{k,c}^{(v)}[i,l] &= \frac{1}{N}\sum_{n=0}^{N-1} n^k \left(\left(\bar{w}_i^{(v)}\right)^*\right)^n \exp\left(-j\frac{2\pi l}{N_0}n\right) \\ &= \frac{1}{N}\sum_{n=0}^{N-1} n^k (q_c[l])^n,\end{aligned} \tag{137}$$

respectively, where

$$q[l] \triangleq \exp\left(j2\pi\left(\bar{F}_i^{(v)} - \frac{l}{N_0}\right)\right) \tag{138}$$

and

$$q_c[l] \triangleq \exp\left(j2\pi\left(-\bar{F}_i^{(v)} - \frac{l}{N_0}\right)\right). \tag{139}$$

Therefore, the identities listed in [10, eqs. (84)-(85) and (145)] can be exploited for an efficient computation of the RHSs of (136) and (137).

A target cancellation procedure is also employed in **T2** of the RASCA-FC2 and RASCA-FC3; however, in this case, the CSFE is adopted in place of the SFE, and the vectors $\mathbf{C}_{X_0}^{(v)}[i]$, $\mathbf{C}_{X_1}^{(v)}[i]$ and $\mathbf{C}_{X_2}^{(v)}[i]$ are evaluated as

$$\mathbf{C}_{X_0}^{(v)}[i] = \hat{A}_i^{(v)}\ \bar{\mathbf{W}}_0^{(v)}[i], \tag{140}$$

$$\mathbf{C}_{X_1}^{(v)}[i] = \hat{A}_i^{(v)}\ \bar{\mathbf{W}}_1^{(v)}[i] \tag{141}$$

and

$$\mathbf{C}_{X_2}^{(v)}[i] = \hat{A}_i^{(v)}\ \bar{\mathbf{W}}_2^{(v)}[i]; \tag{142}$$

respectively; here, $\bar{\mathbf{W}}_k^{(v)}[i]$ denotes the N_0 order DFT of the vector

$$\begin{aligned}\bar{\mathbf{w}}_k^{(v)}[i] \triangleq \Big[0, 1^k \cdot \bar{w}_i^{(v)}, 2^k \cdot \left(\bar{w}_i^{(v)}\right)^2, \ldots, \\ (N-1)^k \cdot \left(\bar{w}_i^{(v)}\right)^{N-1}, 0, \ldots, 0\Big]^T,\end{aligned} \tag{143}$$

with $k = 0$, 1 and 2, and $\bar{w}_i^{(v)}$ is still expressed by (134). The vector $\bar{\mathbf{W}}_k^{(v)}[i]$ appearing in (130)–(132) (with $k = 0$, 1 and 2) can be efficiently computed following the same approach illustrated above for the SFE.

The CSFE is also employed in **T3-S1** and, in particular, in **STDAEC-S2** of the RASCA-FR2, RASCA-FR3, RASCA-FC2 and RASCA-FC3. In this case, the cancellation procedure requires the evaluation of the contribution

$$\mathbf{C}_{X_0}^{(i)}[l] = \left[C_{X_0}^{(i)}[p,q,l]\right] \tag{144}$$

given by the i-th (i.e., by the last) target detected in the l-th frequency bin to the whole array (see (62)). Here, we focus on the target cancellation procedure employed in the above mentioned RASCAs. In this case, if $\hat{A}_i[l]$, $\hat{F}_{\mathrm{V},i}[l]$ and $\hat{F}_{\mathrm{H},i}[l]$ denote the estimates of the complex amplitude, the normalised vertical spatial frequency and the normalised horizontal spatial frequency, respectively, characterizing the i-th target, the expression

$$\begin{aligned}C_{X_0}^{(i)}[p,q,l] = \hat{A}_i[l]\ \exp\Big\{j2\pi\Big[(p-p_R)\hat{F}_{\mathrm{H},i}[l] \\ +(q-q_R)\hat{F}_{\mathrm{V},i}[l]\Big]\Big\},\end{aligned} \tag{145}$$

is employed for any VA (i.e., for any p and q).

Finally, it is important to mention that the cancellation procedure adopted in STDREC algorithm aims at removing the contribution of a single target in each of its iterations. If a *cluster* of $m_i^{(v)}$ distinct frequencies is estimated by the SFE (CSFE) in the i-th iteration of the above mentioned algorithm, each of the components of the triad ($\mathbf{C}_{X_0}^{(v)}[i]$, $\mathbf{C}_{X_1}^{(v)}[i]$, $\mathbf{C}_{X_2}^{(v)}[i]$) consists of the sum of $m_i^{(v)}$ terms and each term is evaluated on the basis of (130)–(132) ((140)–(142)).

E. TARGET CANCELLATION PROCEDURES EMPLOYED IN SFCW RADAR SYSTEMS

In this paragraph we take into consideration a MIMO SFCW radar system and focus on the two cancellation procedures employed in the RASCA-S2 and RASCA-S3 (see Paragraph V); the first procedure is used in combination with the CSDE in **T2** (and, in particular, in **STDREC-S2**), whereas the second one with the CSDE in **T3-S1** (and, in particular, in **STDAEC-S2**). The first procedure is based on (53); in the considered radar system, the vectors ($\mathbf{C}_{X_0}^{(v)}[i]$, $\mathbf{C}_{X_1}^{(v)}[i]$, $\mathbf{C}_{X_2}^{(v)}[i]$) appearing in the RHS of that equation and expressing the contribution given by the i-th (i.e., by the last) target detected on the v-th VA are evaluated as

$$\mathbf{C}_{X_0}^{(v)}[i] = \hat{A}_i^{(v)}\ \bar{\mathbf{W}}_0^{(v)}[i], \tag{146}$$

$$\mathbf{C}_{X_1}^{(v)}[i] = \hat{A}_i^{(v)}\ \bar{\mathbf{W}}_1^{(v)}[i] \tag{147}$$

and

$$\mathbf{C}_{X_2}^{(v)}[i] = \hat{A}_i^{(v)}\ \bar{\mathbf{W}}_2^{(v)}[i], \tag{148}$$

respectively; here, $\bar{\mathbf{W}}_k^{(v)}[i]$ denotes the N_0 order IDFT of the vector

$$\bar{\mathbf{w}}_k^{(v)}[i] \triangleq \left[0,\ 1^k \cdot \bar{w}_i^{(v)},\ 2^k \cdot \left(\bar{w}_i^{(v)}\right)^2, \ldots,\right.$$
$$\left.(N-1)^k \cdot \left(\bar{w}_i^{(v)}\right)^{N-1}, 0, \ldots, 0\right]^T, \tag{149}$$

with $k = 0$, 1 and 2,

$$\bar{w}_i^{(v)} \triangleq \exp(-j2\pi \hat{F}_i^{(v)}), \tag{150}$$
$$\hat{F}_i^{(v)} \triangleq \hat{\tau}_i^{(v)} \Delta f \tag{151}$$

and $\hat{A}_i^{(v)}$ and $\hat{\tau}_i^{(v)}$ represent the estimates of the complex amplitude $A_i^{(v)}$ and of the delay $\tau_i^{(v)}$, respectively, characterizing the i-th target. An efficient method can be used for the computation of the vector $\bar{\mathbf{W}}_k^{(v)}[i]$ appearing in the RHS of (146)–(148) (with $k = 0$, 1 and 2), since, for any k, this vector is the N_0 order IDFTs of the sequence $\{n^k\ (\bar{W}_i^{(v)})^n;$ $n = 0, 1, \ldots, N-1\}$, with $W \triangleq \bar{W}_i^{(v)}$. In fact, the l -th element of the vectors $\bar{\mathbf{W}}_k^{(v)}[i]$ is given by

$$\bar{w}_k^{(v)}[i, l] = \frac{1}{N}\sum_{n=0}^{N-1} n^k \left(\bar{w}_i^{(v)}\right)^n \exp\left(j\frac{2\pi l}{N_0}n\right)$$
$$= \frac{1}{N}\sum_{n=0}^{N-1} n^k (\bar{q}[l])^n, \tag{152}$$

where

$$\bar{q}[l] \triangleq \exp\left(-j2\pi\left(\bar{F}_i^{(v)} - \frac{l}{N_0}\right)\right). \tag{153}$$

Even in this case, the identities listed in [10, eqs. (84), (85) and (145)] can be exploited for an efficient computation of the RHS of (152).

The second cancellation procedure is expressed by (62) and requires the evaluation of the matrix $\mathbf{C}_{X_0}^{(i)}[l]$ (144) given by the i-th (i.e., by the last) target detected in the l-th delay bin on the whole array. If $\hat{A}_i[l]$, $\hat{F}_{\mathrm{V},i}[l]$ and $\hat{F}_{\mathrm{H},i}[l]$ denote the estimates of the complex amplitude, the normalised vertical spatial delay and the normalised horizontal spatial delay, respectively, characterizing that target, $C_{X_0}^{(i)}[p, q, l]$ is evaluated as

$$C_{X_0}^{(i)}[p, q, l] = \hat{A}_i[l]\ \exp\left\{-j2\pi\left[(p - p_R)\hat{F}_{\mathrm{H},i}[l]\right.\right.$$
$$\left.\left.+(q - q_R)\hat{F}_{\mathrm{V},i}[l]\right]\right\}, \tag{154}$$

for any VA (i.e., for any p and q).

VII. LIMITATIONS

In this section, some technical limitations that have emerged in the implementation of our algorithms on commercial radar devices are illustrated and the solutions we have devised to mitigate their impact are described.

A. UNEQUAL RESPONSE OF VIRTUAL ANTENNAS

The derivation of the RASCAs for FMCW radar systems relies on the assumption that the real (complex) sample sequence made available by the v-th VA is expressed by (6) ((12)); the validity of a similar model has been assumed for SFCW radar systems (see (15)). The adopted signal models hold if the amplitudes of the L overlapped oscillations contributing to the useful component of the received signal do not change from antenna to antenna. However, our experiments accomplished on commercial colocated radar devices have evidenced that: a) these amplitudes are not constant across the whole virtual array; b) their differences are influenced by the azimuth and the elevation of each target. We believe that all this is due to the different behavior of the multiple receive chains employed in each MIMO device and to the mismatches in the receive antenna patterns. This problem affects the quality of the data acquired through both FMCW and SFCW radar systems and, consequently, the accuracy of our detection and estimation algorithms. It can be mitigated by enriching the physical array with a set of surrounding *passive antennas*; in this case, the array is artificially extended with new antennas along all its sides, so that the behavior of all its active antennas becomes more uniform.

It important to point out that, in principle, the presence of this phenomenon can be accounted for in the development of target detection and estimation algorithms by including its effects in the received signal model. For instance, (6) can be generalised as

$$x_{r,n}^{(v)} = \sum_{l=0}^{L-1} \alpha_v(\theta_l, \phi_l)\ a_l\ \cos\left(2\pi n F_l^{(v)} + \psi_l^{(v)}\right) + w_{r,n}^{(v)}, \tag{155}$$

where $\alpha_v(\theta_l, \phi_l)$ represents an attenuation factor depending on the angular coordinates of the l-th target and v is the VA index. Consequently, the complex amplitude associated with the l-th target detectable on the considered VA becomes (see (7))

$$C_l^{(v)}(\theta_l, \phi_l) \triangleq \frac{1}{2} a_l\ \alpha_v(\theta_l, \phi_l) \exp\left(j\ \psi_l^{(v)}\right). \tag{156}$$

Neglecting the presence of the factor $\alpha_v\left(\theta_l,\ \phi_l\right)$ in the development of our algorithms has the following implication: an error is introduced by the STDAEC algorithm in its cancellation procedure (see **STDAEC-S2** in Paragraph VI). Note, in particular, that the estimate $\hat{C}_i[l]$ of the complex amplitude characterizing to the i-th target detected in the $\hat{\alpha}_l$-th bin is computed *after* the overall spatial folding (i.e., after **STDAE-S5**); consequently, its absolute value represents a sort of *spatial average* computed over all the involved VAs. Moreover, only the phase variations of this complex gain are accounted for in the computation of the contribution $\mathbf{C}_{X_0}^{(i)}[l]$ of this target to the matrix $\mathbf{X}^{(i)}[l]$ (see (144)–(145)). Note that, if the functions $\{\alpha_v(\theta_l, \phi_l)\}$ were known for all the VAs, their effect could be compensated for *after* evaluating the estimates $(\hat{\theta}_i, \hat{\phi}_i)$ of the angular coordinates of the i-th target; in fact, this

result could be achieved by replacing the estimate $\hat{C}_i[l]$ of the complex gain $C_i[l]$ with

$$\hat{C}_i[v, l] \triangleq \hat{C}_i[l]\, \alpha_v(\hat{\theta}_i, \hat{\phi}_i). \tag{157}$$

in the evaluation of the term $\mathbf{C}_{X_0}^{(i)}[l]$ appearing in (144)–(145). Estimating the function $\alpha_v(\theta, \phi)$, however, is a time consuming task, since it requires a proper measurement setup and an anechoic chamber. We believe that this problem can be circumvented by: a) exploiting *deep learning techniques* [27] in the SPE; b) adopting a *data-driven approach* [28], [29]. This solution is motivated by the fact that:

a) Deep learning techniques can be employed to approximate complicated functions, that do not lend themselves to a simple parametric representation and without requiring particular expertise in data pre-processing.

b) A data-driven approach allows to train different models on the basis of data collected in a real scenario or synthetically generated data, without prior knowledge about the parametric representation of the considered problem. Note that a fundamental role is played by the adopted training procedure since it makes the involved network able to generate correct predictions on the basis of never seen data available at its input.

In practice, the adoption of the proposed approach requires modifying the STDAEC technique employed in the RASCAs (see Fig. 5) and, in particular, embedding a deep neural network in it. This network is employed to estimate the distorted amplitudes of all the targets detected in the l -th frequency bin (with $l = 0, 1, \ldots, L_b - 1$), so that accurate cancellation becomes possible.

The use of this solution in our radar systems is not investigated in the following, since it is out of the scope of this manuscript.

B. ANTENNA COUPLING

In our description of the SFE, the CSFE and the CSDE (see Section VI), it has been implicitly assumed that the minimum frequency of the useful component contained in the observed data sequence can be arbitrarily small. Unluckily, this is not always true. For instance, in commercial colocated FMCW MIMO radar systems, a strong interference is observed in the lower portion of the spectrum evaluated on all the receive antennas. This phenomenon, known as *mutual coupling* [30], is due to the electromagnetic coupling that originates from the small distance between adjacent transmit and receive antennas [20]. Its impact can be mitigated resorting to various methods based on calibration measurements [31]. Because of mutual coupling, any target whose range is below a certain threshold cannot be detected by our algorithms in a reliable fashion.

VIII. OTHER TARGET DETECTION AND ESTIMATION TECHNIQUES

The detection and estimation algorithms described above have been compared, in terms of accuracy and complexity, with two different types of algorithms that, similarly as the RASCAs, are able to generate radar images in the form of point clouds. The algorithms of the first type are called FFT-*based algorithms* (FFT-BAs), since they rely on multidimensional FFT processing for the evaluation of all the spatial coordinates of targets (i.e., their range and DOA); such algorithms have been inspired by the FFT-based algorithm proposed by Texas Instrument in [5]. The algorithms of the second type, instead, are called MUSIC-*based algorithms* (MUSIC-BAs); these make use of the same method as the first type for range estimation, but the MUSIC algorithm for DOA estimation [32]. In the remaining part of this section, a brief description is provided for both types. In our analysis, we always refer to a FMCW radar system, since, if a SFCW radar system is considered, the only change to be made in the described algorithms consists in replacing each FFT with an IFFT of the same order.

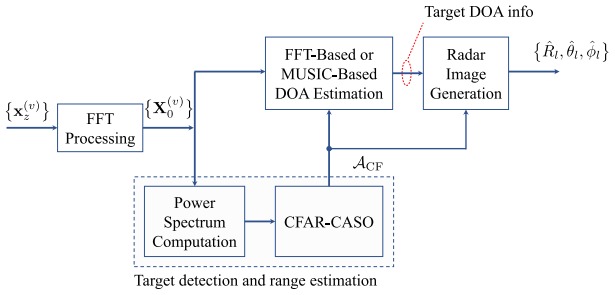

FIGURE 9. Block diagram describing the overall structure of the FFT-BAs and the MUSIC-BAs.

The inner structure of both types of algorithms is described by the block diagram shown in Fig. 9. The processing accomplished by the blocks this diagram consists of, can be summarized as follows. Each vector of the set $\{\mathbf{x}_z^{(v)}\}$, collecting N_{VR} vectors (see (18)), undergoes, after ZP, a N_0 order FFT; this produces a set of N_0-dimensional vectors $\{\mathbf{X}_0^{(v)}\}$ (see (43), (47) and (48)). Based on this set of vectors, the N_0-dimensional power spectrum

$$\mathbf{P}_0 = \left[P_{0,0}, P_{0,1}, \ldots, P_{0,N_0-1}\right]^T \tag{158}$$

is computed; here,

$$P_{0,i} \triangleq \frac{1}{N_{\mathrm{VR}}} \sum_{v=0}^{N_{\mathrm{VR}}-1} \left(X_{0,i}^{(v)}\right)^2 \tag{159}$$

with $i = 0, 1, \ldots, N_0 - 1$. The vector $\mathbf{P}_0$ (158) feeds the *cell-averaging smallest of - constant false alarm rate* (CFAR-CASO) algorithm developed in [33]. Based on this algorithm, a target is detected in the i-th frequency bin if

$$P_{0,i} > T_{\mathrm{CFAR}}, \tag{160}$$

where $i \in \{i_m, i_m + 1, \ldots, i_M\}$. Here,

$$T_{\mathrm{CFAR}} = K_0 \min\left(\bar{P}_l,\ \bar{P}_u\right) \tag{161}$$

represents a decision threshold, K_0 is a real parameter whose value is selected on the basis of the required *false alarm rate*,

and

$$\bar{P}_l = \frac{1}{C_s} \sum_{k=i-(G_s+C_s)}^{i-(G_s+1)} P_{0,k} \tag{162}$$

and

$$\bar{P}_u = \frac{1}{C_s} \sum_{k=i+G_s+1}^{i+G_s+C_s} P_{0,k} \tag{163}$$

represent the average of the power spectrum computed over C_s adjacent bins positioned on the left and on the right, respectively, with respect to the i-th frequency bin. Moreover, G_s and C_s are two integer parameters defining the size and the position (with respect to the i-th bin), respectively, of the set of frequency bins involved in the computation of $\bar{P}_l$ (162) and $\bar{P}_u$ (163), whereas i_m and i_M are two non negative integers such that $i_m \geq (G_s + C_s)$ and $i_M \leq N_0 - 1 - (G_s + C_s)$.

In our work, the inequality

$$P_{0,i} > P_{l,u} \tag{164}$$

is also required to be satisfied together with the condition (160), where $P_{l,u}$ represents the largest element of the set $\{P_{0,i+l};\ l = -(G_s + C_s), -(G_s + C_s) + 1, -G_s - 1, G_s + 1, G_s + C_s\}$. This allows us to reduce the overall number of detected targets, so reducing the density of the generated point cloud.

The CFAR-CASO algorithm generates the vector

$$\mathcal{A}_{\mathrm{CF}} = \left[\hat{\alpha}_0, \hat{\alpha}_1, \ldots, \hat{\alpha}_{L_b-1}\right]^T \tag{165}$$

where $\hat{\alpha}_l$ represents the index of the frequency bin in which the l-th target has been detected (with $l = 0, 1, \ldots, L_b - 1$) and L_b is the overall number of detected targets. This vector is processed for DOA estimation. The two options (associated with the above mentioned types of algorithms) are considered for this task and are described in the remaining part of this paragraph.

FFT-*based* DOA *estimation* – Let us focus first on the case in which a virtual HULA, consisting of N_{VH} virtual elements, is employed for resolving the targets associated with a given frequency bin and estimating their azimuth. In this case, azimuth estimation consists of the following two steps:

1) The N_{VH}-dimensional column vector (see (88))

$$\mathbf{X}\left[l\right] \triangleq \left[X_{0,\hat{\alpha}_l}^{(0)}, X_{0,\hat{\alpha}_l}^{(1)}, \ldots, X_{0,\hat{\alpha}_l}^{(N_{\mathrm{VH}}-1)}\right]^T, \tag{166}$$

collecting the spectral information available on the whole array and referring to the $\hat{\alpha}_l$-th frequency bin (with $l = 0, 1, \ldots, L_b - 1$) is applied to an $\bar{N}_0$ order FFT algorithm; let $\mathbf{s}[l] = [s_0[l], s_1[l], \ldots, s_{\bar{N}_0-1}[l]]^T$ denote the $\bar{N}_0$-dimensional FFT output.

2) The dominant peaks[11] in the sequence $\{|s_k[l]|;\ k = 0, 1, \ldots, \bar{N}_0 - 1\}$ are identified; each peak corresponds to a distinct target. If $k_i[l]$ denotes the index of i-th peak (with $i = 0, 1, \ldots, L_h[l] - 1$, where $L_h[l]$ is the overall number of targets detected in the considered frequency bin), the estimate of the azimuth of the i-th target is evaluated as

$$\hat{\theta}_i\left[l\right] = \arcsin\left(h_{\bar{N}_0}\left[k_i\left[l\right]\right]\right) \tag{167}$$

where

$$h_{\bar{N}_0}\left[x\right] \triangleq 2\left(x - \bar{N}_0/2\right)/\bar{N}_0\,. \tag{168}$$

Let us now consider the case in which the URA represented in Fig. 4 is employed for resolving the targets associated with each frequency bin, and estimating their azimuth and elevation. The algorithm employed in this case involves the $N_{\mathrm{VH}} \times N_{\mathrm{VV}}$ matrix $\mathbf{X}[l] \triangleq [X_{0,\hat{\alpha}_l}[p, q]]$ (60), collecting the spectral information available on the whole array for the $\hat{\alpha}_l$-th frequency bin. This algorithm consists of the following four steps:

1) The p_R-th row of the matrix $\mathbf{X}[l]$ is processed to generate the $\bar{N}_0$-dimensional column vector $\mathbf{s}_{\mathrm{VULA},0}[l] = [s_{0,0}\left[l\right], s_{0,1}\left[l\right], \ldots, s_{0,\bar{N}_0-1}\left[l\right]]^T$ on the basis of (68); here, p_R represents the column index of the reference antenna in the considered URA (see Fig. 4).

2) The dominant peaks of the sequence $\{[|s_{0,r}\left[l\right]|;\ r = 0, 1, \ldots, \bar{N}_0 - 1\}$ are identified. If $r_i[l]$ denotes the index of i-th peak (with $i = 0, 1, \ldots, L_v[l] - 1$, where $L_v[l]$ is the overall number of targets detected in the considered frequency bin), the estimate of the elevation $\hat{\phi}_i[l]$ of the associated target is evaluated as

$$\hat{\phi}_i\left[l\right] = \arcsin\left(h_{\bar{N}_0}\left[r_i\left[l\right]\right]\right). \tag{169}$$

3) The 2D FFT of the matrix $\mathbf{X}[l]$ is computed; this produces the $\bar{N}_0 \times \bar{N}_0$ matrix $\bar{\mathbf{S}}[l] = [\bar{S}_{k,r}[l]]$, such that

$$\bar{S}_{k,r}\left[l\right] \triangleq \frac{1}{N_{\mathrm{VR}}} \sum_{q=0}^{N_{\mathrm{VV}}-1} \sum_{p=0}^{N_{\mathrm{VH}}-1} X_{0,\hat{\alpha}_l}\left[p, q\right] \cdot \exp\left(-j\frac{2\pi}{\lambda}\psi_{r,k}\right), \tag{170}$$

where

$$\psi_{r,k} \triangleq q\, h_{\bar{N}_0}[r]\, d_{\mathrm{VV}} + p\, h_{\bar{N}_0}[k]\, d_{\mathrm{VH}}. \tag{171}$$

4) The dominant peaks of the sequence $\{[|\bar{S}_{k,r_i[l]}[l]|;\ k = 0, 1, \ldots, \bar{N}_0 - 1\}$ are identified (with $i = 0, 1, \ldots, L_v[l] - 1$); let $L_h[i, l]$ denote their overall number. If the m-th peak is found for $k = k_{m,i}[l]$ (with $m = 0, 1, \ldots, L_h[i, l] - 1$), the azimuth $\hat{\theta}_{i,r_i[l]}[l]$ of the associated target is evaluated as

$$\hat{\theta}_{i,r_i[l]}\left[l\right] = \arcsin\left(\frac{h_{\bar{N}_0}\left[k_{m,i}[l]\right]}{\cos\left(\hat{\phi}_i\left[l\right]\right)}\right), \tag{172}$$

where $\hat{\phi}_i\left[l\right]$ is expressed by (169); consequently, the angular coordinates of the i-th target detected in the $\hat{\alpha}_l$-th frequency bin are $(\hat{\theta}_{i,r_i[l]}\left[l\right], \hat{\phi}_i\left[l\right])$, whereas its range is computed on the basis of $\hat{\alpha}_l$.

[11] It is important to distinguish peaks associated with different targets from side-lobes; in our simulations, a candidate peak is classified as a side-lobe (and, consequently, ignored) if its amplitude differs by more than 1 dB from that of a close dominant peak, as suggested in [5].

The last step concludes our description of the FFT-BAs. Note that the overall number of detected targets is given by

$$\hat{L} = \sum_{l=0}^{L_b-1} \sum_{i=0}^{L_v[l]-1} L_h[i,l]. \tag{173}$$

MUSIC-*based* DOA *estimation* – Similarly as our description of the FFT-BAs, we first focus on the case in which a virtual HULA, consisting of N_{VH} virtual elements, is employed for resolving the targets associated with a given frequency bin and estimating their azimuth. In this case, the algorithm considered for DOA estimation consists of the following three steps:

1) The $N_{\mathrm{VH}} \times N_{\mathrm{VH}}$ autocorrelation matrix

$$\mathbf{R}_X[l] = \mathbf{X}[l]\,\mathbf{X}[l]^H \tag{174}$$

is computed; here, $\mathbf{X}[l]$ is defined by (166).

2) The $\bar{N}_0$-dimensional *pseudo-spectrum* $\mathbf{P}_{\mathrm{MU}}^{(l)}$ is evaluated; its k-th element is given by

$$\mathcal{P}_{\mathrm{MU}}^{(l)}[k] = \frac{1}{\mathbf{a}^H[k]\,\mathbf{Q}_{N_{\mathrm{VR}}}\mathbf{Q}_{N_{\mathrm{VR}}}^H\,\mathbf{a}[k]} \tag{175}$$

with $k = 0, 1, \ldots, \bar{N}_0 - 1$; here, $(\cdot)^H$ denotes the conjugate and transpose operator, $\mathbf{Q}_{N_{\mathrm{VH}}}$ is a matrix having size $N_{\mathrm{VH}} \times (N_{\mathrm{VH}}-1)$ and whose columns are the $(N_{\mathrm{VH}}-1)$ noise eigenvectors (associated with the $(N_{\mathrm{VH}}-1)$ smallest eigenvalues) of $\mathbf{R}_X[l]$ (174) and $\mathbf{a}[k]$ is a N_{VH}-dimensional steering vector, whose n-th element $a_n[k]$ is given by[12]

$$a_n[k] = \exp\left(j\pi n\, h_{\bar{N}_0}[k]\right), \tag{176}$$

with $n = 0, 1, \ldots, N_{\mathrm{VH}} - 1$.

3) The dominant peaks appearing in the sequence $\{\mathcal{P}_{\mathrm{MU}}^{(l)}[k];\ k = 0, 1, \ldots, \bar{N}_0 - 1\}$, consisting of the ordered elements of $\mathbf{P}_{\mathrm{MU}}^{(l)}$, are identified; let $L_h[l]$ denote their overall number. If the i-th peak is found for $k = k_i[l]$ (with $i = 0, 1, \ldots, L_h[l] - 1$), the azimuth $\hat{\theta}_i[l]$ of the associated target is evaluated on the basis of (167)–(168).

Let us consider now the case in which the uniform rectangular array shown in Fig. 4 is employed for resolving the targets associated with each frequency bin, and estimating their azimuth and elevation. In this case, the adopted procedure involves the $N_{\mathrm{VH}} \times N_{\mathrm{VV}}$ matrix $\mathbf{X}[l] \triangleq [X_{0,\hat{\alpha}_l}[p,q]]$ (60) for any $\hat{\alpha}_l$ and consists of the following four steps:

1) The pseudo-spectrum referring to the reference VULA (that consists of N_{VULA} virtual elements) is evaluated. In this step, we assume that the p_R-th row of $\mathbf{X}[l]$ is employed for the evaluation of the autocorrelation matrix $\mathbf{R}_X[l]$ (174) and that the $\bar{N}_0$-dimensional vector $\mathbf{P}_{\mathrm{MU}}^{(\mathrm{VULA})}[l]$ is computed on the basis of (175)–(176) (note that N_{VR} and $\delta[k]$ are replaced by N_{VULA} and $\delta[r]$, respectively).

2) The dominant peaks appearing in the sequence of the ordered elements of $\mathbf{P}_{\mathrm{MU}}^{(\mathrm{VULA})}[l]$ are identified; let $L_v[l]$ denote their overall number. If the i-th peak is found for $r = r_i[l]$ (with $i = 0, 1, \ldots, L_v[l] - 1$), the elevation $\hat{\phi}_i[l]$ of the associated target is evaluated on the basis of (169).

3) The pseudo-spectrum $\mathbf{P}_{\mathrm{MU}}^{(\mathrm{HULA})}[l,i]$ associated with the i-th estimated elevation is evaluated for the whole virtual array. In this step, if we assume that the autocorrelation matrix $\mathbf{R}_X$ is computed according to (174) (where, however, $\mathbf{X}[l]$ is the $N_{\mathrm{VH}} \times N_{\mathrm{VV}}$ matrix defined above), the $\bar{N}_0$-dimensional vector $P_{\mathrm{MU}}^{(\mathrm{HULA})}[l,i]$ is generated on the basis of (175). Note that, in this case, N_{VR} is replaced by N_{HULA} and that the n-th element $a_n[k]$ of the N_{HULA}-dimensional steering vector $\mathbf{a}[k]$ is

$$a_n[k] = \exp\left(j\pi n\, h_{\bar{N}_0}[k] \cos\left(\hat{\phi}_i[l]\right)\right) \tag{177}$$

with $n = 0, 1, \ldots, N_{\mathrm{HULA}}$.

4) The dominant peaks appearing in the sequence of the ordered elements of $\mathbf{P}_{\mathrm{MU}}^{(\mathrm{HULA})}[l]$ are identified; let $L_h[i,l]$ denote their overall number. If the m-th peak is found for $k = k_{m,i}[l]$ (with $m = 0, 1, \ldots, L_h[i,l] - 1$), the azimuth $\hat{\theta}_{i,r_i[l]}[l]$ of the associated target is evaluated as

$$\hat{\theta}_{i,r_i[l]}[l] = \arcsin\left(h_{\bar{N}_0}\left[k_{m,i}[l]\right]\right). \tag{178}$$

Consequently, the angular coordinates of this target are $(\hat{\theta}_{i,r_i[l]}[l], \hat{\phi}_i[l])$, whereas its range is computed on the basis of its bin index $\hat{\alpha}_l$. The last step concludes our description of the MUSIC-BAs. Finally it is important to point out that:

a) The overall number of targets detected by these algorithms is still expressed by (173).

b) The order adopted in the computation of the pseudo-spectra (first the vertical pseudo spectrum $\mathbf{P}_{\mathrm{MU}}^{(\mathrm{VULA})}[l]$, then the horizontal pseudo-spectra $\{\mathbf{P}_{\mathrm{MU}}^{(\mathrm{HULA})}[l,i]\}$) is dictated by the fact $\mathbf{P}_{\mathrm{MU}}^{(\mathrm{HULA})}[l,i]$ depends on the elevation estimate $\hat{\phi}_i[l]$ for any i.

The performance of the FFT-BAs and the MUSIC-BAs has been assessed for both FMCW and SFCW radar systems working in 2D and 3D propagation scenarios. The acronyms adopted in the following for these types of algorithms are summarized in Table 2.

TABLE 2. Acronyms adopted for the FFT-based and MUSIC-based algorithms.

Alg. \ Radar	Complex FMCW	Real FMCW	SFCW
FFT-BA (2D)	FFT-FC2	FFT-FR2	FFT-S2
MUSIC-BA (2D)	MUSIC-FC2	MUSIC-FR2	MUSIC-S2
FFT-BA (3D)	FFT-FC3	FFT-FR3	FFT-S3
MUSIC-BA (3D)	MUSIC-FC3	MUSIC-FR3	MUSIC-S3

IX. COMPUTATIONAL COMPLEXITY

The computational cost of the algorithms described in Sections IV, V and VIII has been carefully assessed in terms of *floating point operations* (flops) to be executed in the detection of L targets.[13] Various details about the method

[12] Note that the following equation applies to an FMCW radar; if an SFCW radar is considered, the sign of the argument of the complex exponential appearing in its RHS must be reversed.

[13] In the remaining part of this section, the overall number of estimated targets ($\hat{L}$) is assumed to be equal to L, for simplicity.

we adopted for the evaluation of the computational cost of each algorithm are provided in Appendix for the RASCA-FC3 only. Our analysis leads to the conclusion that the overall cost of this algorithm and RASCA-FC2 is approximately of order $\mathcal{O}(M_{\mathrm{R-FC3}})$ and $\mathcal{O}(M_{\mathrm{R-FC2}})$, respectively, where (see (195))

$$M_{\mathrm{R-FC3}} = 24N_{\mathrm{VR}}\,N_0\log_2(N_0) + 26N_A\,K_{\mathrm{T}_2}\,N_0 + L_b\,K_{\mathrm{T}_3}\left(18N_{\mathrm{VH}}\,N_{\mathrm{VV}}\,N_0 + 16\bar{N}_0\log_2\left(\bar{N}_0\right)\right) \tag{179}$$

and

$$M_{\mathrm{R-FC2}} = 24N_{\mathrm{VH}}\,N_0\log_2(N_0) + 26N_A\,K_{\mathrm{T}_2}N_0 + L_b\,K_{\mathrm{T}_3}\left(18N_{\mathrm{VH}}\,N_0 + 8\bar{N}_0\log_2(\bar{N}_0)\right); \tag{180}$$

here, K_{T_2} (K_{T_3}) represents the overall number of iterations carried out by the STDREC (STDAEC) algorithm.

In evaluating the cost of the FFT-based and MUSIC-based algorithms described in Section VIII, we have assumed that: a) the cost due to the computation of the eigenvalue decomposition of a $d \times d$ matrix is $\mathcal{O}(d^3)$; b) the computational effort required to find the dominant peaks in a sequence is negligible. Based on these assumptions, it can be shown that the computational complexity of the FFT-FC3, FFT-FC2, MUSIC-FC3 and MUSIC-FC2 algorithms are approximately of order $\mathcal{O}(M_{\mathrm{F-FC3}})$, $\mathcal{O}(M_{\mathrm{F-FC2}})$, $\mathcal{O}(M_{\mathrm{M-FC3}})$ and $\mathcal{O}(M_{\mathrm{M-FC2}})$, respectively, where

$$M_{\mathrm{F-FC3}} = 8N_{\mathrm{VR}}N_0\log_2(N_0) + 8L_b\left(\bar{N}_0^2\log_2(\bar{N}_0^2) + \bar{N}_0\log_2(\bar{N}_0)\right), \tag{181}$$

$$M_{\mathrm{F-FC2}} = 8\left(N_{\mathrm{VH}}N_0\log_2(N_0) + L_b\bar{N}_0\log_2(\bar{N}_0)\right), \tag{182}$$

$$M_{\mathrm{M-FC3}} = 8N_{\mathrm{VR}}N_0\log_2(N_0) + L_b\bar{N}_0(N_{\mathrm{VV}}^3 + N_{\mathrm{VH}}^3) + 16L_b\bar{N}_0(N_{\mathrm{VV}}^2 + N_{\mathrm{VH}}^2) \tag{183}$$

and

$$M_{\mathrm{M-FC2}} = 8N_{\mathrm{VH}}N_0\log_2(N_0) + L_b\bar{N}_0(N_{\mathrm{VH}}^3 + 16N_{\mathrm{VH}}^2). \tag{184}$$

It is important to keep in mind that a comparison among the computational costs listed above does not fully account for the gap that can be observed in the execution speed of the corresponding algorithms. In fact, in practice, a portion of the computation time is absorbed by the procedure employed to find the dominant peaks of real sequences in both the FFT-BAs and the MUSIC-BAs. Moreover, the vector $\mathcal{A}_{\mathrm{CF}}$ (165), collecting the indices of the frequency bins in which *at least* one target has been detected, may include *ghost* targets; as evidenced by our computer simulations, the impact of this phenomenon on the overall computation time may not be negligible. Despite this, some interesting insights on how the complexity is influenced by the overall number of targets can be obtained by comparing the computational costs (179), (181) and (183) ((180), (182) and (184)) in two specific scenarios. The first scenario we take into consideration refers to the case in which the mutual distance between the targets is *above* the range resolution of the employed radar system, so that $K_{\mathrm{T}_2} = L$, $K_{\mathrm{T}_3} = 1$ and $L_b = L$ can be assumed in the RHS of (179)–(184). In our second scenario, instead, the targets form clusters, each of which consists of four targets having the *same* range, but different angular coordinates; for this reason, $K_{\mathrm{T}_2} = L/4$, $K_{\mathrm{T}_3} = 4$ and $L_b = L/4$ can be assumed in the RHS of (179)–(184). Moreover, the following parameters have been chosen for both scenarios: a) $N_{\mathrm{VR}} = 256$; b) $N_0 = 1024$; c) $N_A = 10$ d) $N_{\mathrm{VV}} = 16$; e) $N_{\mathrm{VH}} = 16$; f) $\bar{N}_0 = 32$. The dependence of the complexity M_{alg} on L is represented in Fig. 10a (Fig. 10b) for the first (second) scenario; here, alg denotes the algorithm which this complexity refers to. From these figures it is easily inferred that:

a) The RASCAs require the largest computational effort in both the considered scenarios for any value of L; for instance, $M_{\mathrm{RASCA-FC3}}$ is approximately 4.1 (4.6) times greater than $M_{\mathrm{MUSIC-FC3}}$ in the first (second) scenario for $L = 8$.

b) The ratio between $M_{\mathrm{RASCA-FC2}}$ and $M_{\mathrm{MUSIC-FC2}}$ is approximately 2.4 for any value of L in the first scenario, but it increases with L in the second scenario; for instance, $M_{\mathrm{RASCA-FC2}}$ is 3.9 (4.6) times greater than $M_{\mathrm{MUSIC-FC2}}$ for $L = 12$ ($L = 36$).

c) The computational cost estimated for the MUSIC-BAs in the first scenario is larger than that referring to the second scenario for $L \geq 4$; for instance, if $L = 20$, the value of $M_{\mathrm{MUSIC-FC3}}$ ($M_{\mathrm{MUSIC-FC2}}$) evaluated in first scenario is 1.33 (2.5) times larger than that found in the second scenario.

Finally, it is important to stress that:

a) in real world scenarios, the overall number of targets detected by the FFT-BAs and the MUSIC-BAs may be greater than the true number of targets, since some targets are detected multiple times; this may have a significant impact on the overall computational effort required by these algorithms.

b) The computational complexity of the RASCA-FR3 and the RASCA-S3 (RASCA-FR2 and RASCA-S2), the FFT-FR3 and the FFT-S3 (FFT-FR2 and FFT-S2), and the MUSIC-FR3 and the MUSIC-S3 (MUSIC-FR2 and MUSIC-S2) is of the same order as the RASCA-FC3 (RASCA-FC2), the FFT-FC3 (FFT-FC2) and the MUSIC-FC3 (MUSIC-FC2), respectively.

X. NUMERICAL RESULTS

In this section, the accuracy of the RASCAs is assessed on the basis of both synthetically generated and experimental data, and is compared with that provided by various FFT-BAs and MUSIC-BAs.

A. NUMERICAL RESULTS BASED ON SYNTHETICALLY GENERATED MEASUREMENTS

In this paragraph, the accuracy achieved by the RASCA-FC3, the FFT-FC3 and the MUSIC-FC3 in the generation

TABLE 3. ***Root mean square error*** $\bar{\varepsilon}_X$, ***peak error*** $\hat{\varepsilon}_X$ **and** ***detection rate*** R_D **evaluated in the two simulation scenarios defined in Paragraph X-A. Target range, azimuth and elevation are taken into consideration.**

		$\bar{\varepsilon}_X$			$\hat{\varepsilon}_X$			
Scenario	Algorithm	R (m)	θ (°)	ϕ (°)	R (m)	θ (°)	ϕ (°)	R_{D} (%)
S1	RASCA-FC3	0.01	1.56	0.79	0.02	9.86	2.64	100
	FFT-FC3	0.02	2.07	1.05	0.04	14.34	3.06	71
	MUSIC-FC3	0.02	1.74	0.83	0.04	34.03	13.48	70
S2	RASCA-FC3	0.01	1.54	0.79	0.02	8.01	2.31	100
	FFT-FC3	0.02	2.05	1.05	0.04	14.78	2.95	70
	MUSIC-FC3	0.02	1.53	0.81	0.04	7.56	2.03	0.72

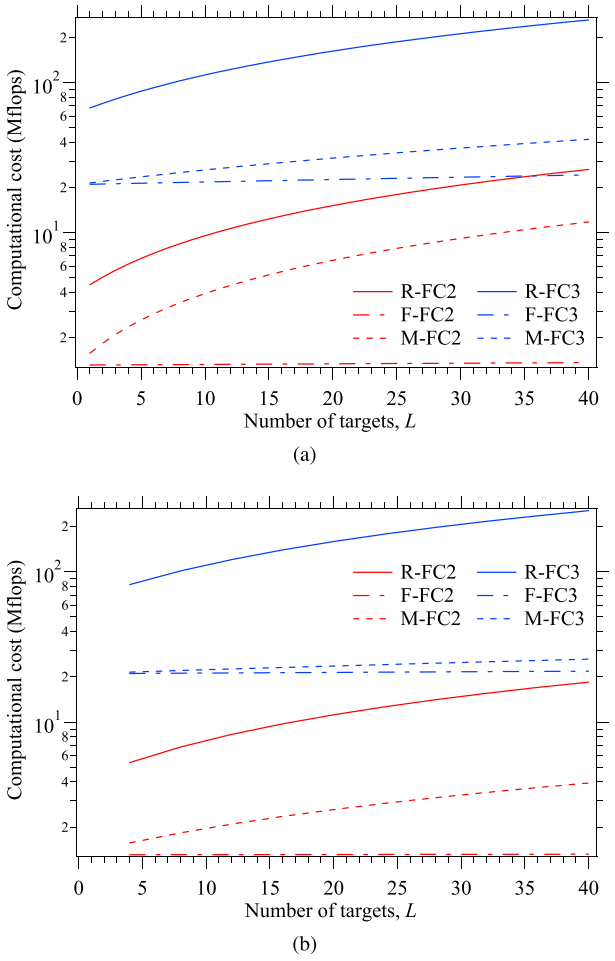

FIGURE 10. **Computational cost versus overall number of targets for: a) the first scenario; b) the second scenario. The RASCA-FC3, RASCA-FC2, FFT-FC3, FFT-FC2, MUSIC-FC3 and MUSIC-FC2 are considered.**

of 3D radar images is assessed. The performance of these algorithms has been evaluated in a colocated MIMO FMCW radar system providing both the in-phase and quadrature components of all its received signals, and equipped with an URA consisting of $N_T = 16$ TX and $N_R = 16$ RX antennas; therefore, the available virtual array is made of $16 \cdot 16 = 256$ VAs with inter-antenna spacing $d_{\mathrm{VV}} = d_{\mathrm{VH}} = \lambda/4$. The other relevant parameters of the considered radar system are: a) chirp slope $\mu = 4 \cdot 10^{13}$ Hz/s; b) bandwidth $B = 2.5$ GHz; c) central frequency $f_0 = 77$ GHz; d) sampling frequency $f_s = 8$ MHz; e) number of samples per chirp $N = 512$. Note that, in principle, the available antenna array allows us to achieve the range resolution

$$\Delta R = \frac{c}{2B} \cong 6\mathrm{cm}, \tag{185}$$

the azimuthal resolution

$$\Delta\theta = \frac{\lambda}{2d_{\mathrm{VH}}(N_{\mathrm{HULA}} - 1)} \cong 7.45^\circ \tag{186}$$

and the elevation resolution

$$\Delta\phi = \frac{\lambda}{2d_{\mathrm{VV}}(N_{\mathrm{VULA}} - 1)} \cong 7.45^\circ. \tag{187}$$

The considered radar system is assumed to operate in the presence of $L = 10$ targets, whose echoes have unit amplitude. The range, the azimuth and the elevation of each target are sequentially generated at the beginning of each run. Moreover, the range R_k, the azimuth θ_k and the elevation ϕ_k of the k-th target (with $k = 1, 2, \ldots, 10$) have been randomly evaluated in a way that: a) they belong to the intervals $[1,\ 10]$ m, $[-\pi/3,\ \pi/3]$ rad and $[-\pi/3,\ \pi/3]$ rad, respectively; b) the minimum spacing between the k-th target and the previously generated $(k-1)$ targets is not smaller than ΔR (185), $\Delta\theta$ (186) and $\Delta\phi$ (187) in the range, azimuth and elevation dimensions, respectively (scenario **S1**) or is not smaller than ΔR (185) in the range domain, but can be arbitrarily small in the azimuth and elevation dimensions (this scenario is denoted **S2**). In our computer simulations, the following values have been selected for the parameters of the RASCA-FC3:

a) FFT Processing: $M = 2$;
b) RPE: $N_A = 10$, $N_{\mathrm{CSFE}} = 10$, $I = 7$ and $T_{\mathrm{STDREC}} = 0.001 \cdot E_0^{(v_k)}$ (see (54));
c) SPE: $\bar{M} = 2$, $N_{\mathrm{CSFE}} = 10$, $I = 7$ and $T_{\mathrm{STDAEC}} = 0.001 \cdot E^{(0)}[l]$ (see (63)), $T_{\mathrm{OF}} = 0$.

In addition, the following values have been selected for the parameters of the FFT-FC3 and the MUSIC-FC3: $C_s = 3$, $G_s = 2$ and $K_0 = 1.5$. The SNR $\triangleq 1/\sigma^2$ has been assumed to be equal to 10 dB and the following performance indices have been evaluated to assess estimation accuracy: a) The *detection rate* (R_{D}) defined as the percentage of simulation runs in which the considered algorithm detects all the targets;

b) the *root mean square error* (RMSE)

$$\bar{\varepsilon}_X \triangleq \sqrt{N_m^{-1} \sum_{k=0}^{N_m-1} \left[X_k - \hat{X}_k\right]^2}; \tag{188}$$

c) the *peak error*

$$\hat{\varepsilon}_X \triangleq \max_k \left|X_k - \hat{X}_k\right|; \tag{189}$$

here, X_i and $\hat{X}_i$ represent the exact value of a parameter X and its corresponding estimate, whereas N_m represents the overall number of synthetically generated values of X; note that, if all the targets are detected by the considered algorithm in each run,

$$N_m \triangleq N_r\, L \tag{190}$$

where N_r is the overall number of simulation runs. In our work, the performance of the above mentioned algorithms has been assessed by: a) evaluating the detection rate for both the considered scenarios; b) ignoring the failure events (i.e., the events in which not all the targets have been detected) in the evaluation of all the RMSEs. The three performance indices defined above have been assessed on the basis of the estimates generated by executing $N_r = 500$ runs; the resulting values are summarised in Table 3. From these results it is easily inferred that:

a) The RASCA-FC3 achieves the lowest RMSEs in range, azimuth and elevation (range, elevation) estimation in the first (second) scenario; for instance, the RMSE $\bar{\varepsilon}_\theta$ characterising the RASCA-FC3 is about 1.3 (1.3) times smaller than the corresponding RMSE obtained for the FFT-FC3 in the first (second) scenario.

b) The RASCA-FC3 exhibits the lowest peak errors in range, azimuth and elevation (range) in the first (second) scenario; for instance, its peak error $\hat{\varepsilon}_R$ is 2 times smaller than the corresponding RMSE obtained for the FFT-FC3 and the MUSIC-FC3 in both scenarios.

c) All the considered algorithms achieve an excellent accuracy in both scenarios, since the RMSEs evaluated for range, azimuth and elevation are smaller than the corresponding resolutions given above.

d) The FFT-FC3 and the MUSIC-FC3 are outperformed by the RASCA-FC3 in terms of detection rate; in fact, the value of this parameter is about 70 % for the first two algorithms, but is equal to 100 % for the RASCA-FC3, since the last algorithm has been able to detect all the targets in every simulation run in both scenarios.

B. NUMERICAL RESULTS BASED ON EXPERIMENTAL MEASUREMENTS

In this paragraph, we first describe the radar devices employed in our measurement campaigns and the adopted experimental setup. Then, we analyse: 1) the accuracy achieved by our RPE (and, in particular, by the STDREC algorithm) in range and phase estimation on multiple antennas of the same array in the presence of a single target and of multiple targets; 2) the accuracy of the 2D (3D) images generated by RASCA-FR2 (RASCA-FR3), RASCA-FC2 (RASCA-FC3) and RASCA-S2 (RASCA-S3) in the presence of multiple targets.

1) EMPLOYED RADAR DEVICES AND ADOPTED EXPERIMENTAL SETUP

A measurement campaign has been accomplished to acquire a data set through two FMCW MIMO radars and one SFCW MIMO radar, all operating in the E-band. The first FMCW device, dubbed **TI FMCW** radar in the following, is the TIDEP-01012 *Cascade mmWave* radar (see Fig. 11 -a)). It is manufactured by *Texas Instrument Inc.* [34], classified as a *long range radar* (LLR) and provides both the in-phase and quadrature components of received signals (i.e., *complex measurements*). Its main parameters are: a) chirp slope $\mu = 4 \cdot 10^{13}$ Hz/s; b) bandwidth $B_1 = 2.5$ GHz; c) central frequency $f_c = 77$ GHz; d) sampling frequency $f_s = 8$ MHz; e) number of samples per chirp $N = 512$. Moreover, it is endowed with a planar array made of $N_T = 12$ TX and $N_R = 16$ RX antennas (each consisting of an array of four patch elements), as shown in Fig. 11-a). The corresponding virtual array consists of $12 \cdot 16 = 192$ VAs; however, only 134 of them are available, since the remaining 58 VAs overlap with the other elements of the virtual array. As shown in Fig. 11-b) (where each VA is represented by a small blue circle), the virtual array has the following characteristics:

1) the non-overlapped VAs form an *horizontal* ULA (HULA_1), consisting of $N_{\text{HULA}_1} = 86$ VAs and three smaller HULAs, each made of 16 equally-spaced VAs;
2) the inter-antenna spacing of all the HULAs is $d_{\text{VH}} = \lambda/4$;
3) the vertical spacing of the three smaller HULAs is not uniform, since $d_{\text{VV}_1} = \lambda/4$, $d_{\text{VV}_2} = \lambda$ and $d_{\text{VV}_3} = 3\lambda/2$ (see Fig. 11-b)).

This virtual antenna array allows us to achieve a range, azimuth and elevation resolution equal to $\Delta R_1 = 5.8$ cm (see (185)), $\Delta\theta_1 = 1.35°$ (see (186)), and $\Delta\phi_1 = 16.4°$ (see (187)), respectively; note that the elevation resolution is coarser than the azimuth one since $N_{\text{VV}} = 7$ equally aligned antennas ($d_{\text{VV}} = d_{\text{VV}_1} = \lambda/4$) are assumed along the vertical direction (this is equivalent to considering an elevation aperture $D_y = 3\lambda$ along the vertical direction; see [20]). In our work, on the one hand, a central portion of the first HULA (contained inside the red rectangle appearing in Fig. 11-b)), consisting of $N_{\text{VV}} = 16$ antennas, has been exploited for 2D imaging, in order to guarantee a fair comparison with the other two radar devices. On the other hand, the whole array have been employed for 3D imaging.

The second FMCW device, dubbed **Inras FMCW** radar in the following (see Fig. 12-a)), is a modular system manufactured by *Inras GmbH* [35] and consisting of: a) the so called *Radar Log* board; b) an RF front-end including

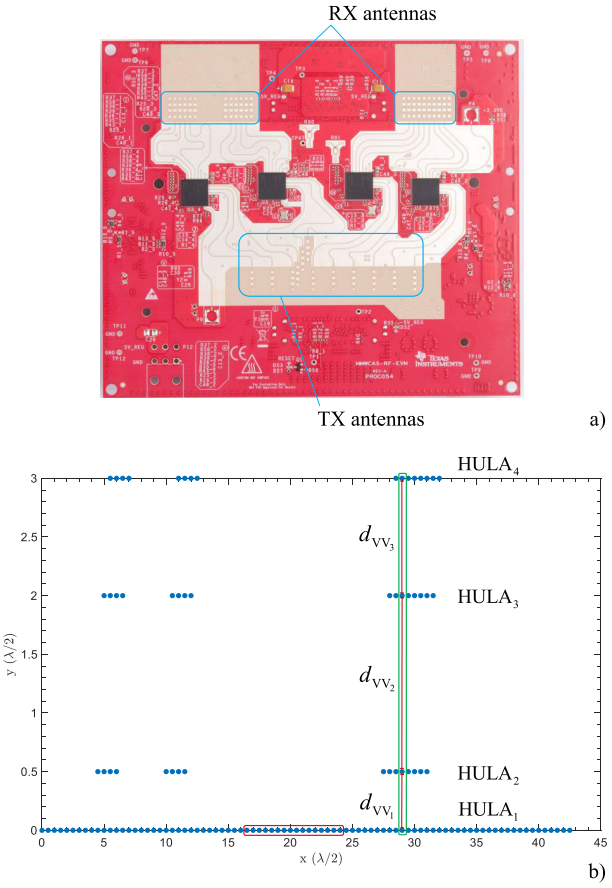

FIGURE 11. Representation of: a) the TI FMCW radar (the physical TX/RX antennas are contained inside the three rounded rectangles); b) the corresponding virtual array (the lower rounded rectangle contains the portion of HULA_1 employed for 2D imaging, whereas the green one the vertical array chosen as a reference for 3D imaging).

multiple TX/RX antennas and *monolithic microwave integrated circuits* (MMIC) operating at 77 GHz. This system is classified as a LLR and its main parameters are: a) chirp slope $\mu = 9.7656 \cdot 10^{12}$ Hz/s; b) bandwidth $B_2 = 2.5$ GHz; c) central frequency $f_c = 77$ GHz; d) sampling frequency $f_s = 8$ MHz; e) number of samples per chirp $N = 2048$. Unlike the TI FMCW radar, this device provides only the in-phase component of the RF received signals and, consequently, *real measurements*. Moreover, it is endowed with a custom designed planar array made of $N_T = 16$ TX antennas and $N_R = 16$ RX antennas, each consisting of an array of six patch elements, as shown in Fig. 12-a). The resulting virtual array, consisting of $N_{\text{VR}} = 16 \cdot 16 = 256$ VAs is shown in Fig. 12-b). As it can be inferred from the last figure, the virtual array has the following characteristics:

1) It consists of 16 HULAs, each of which is made of 16 antennas with inter-antenna spacing $d_{\text{VH}} = \lambda/4$.
2) The vertical distance between each couple of its adjacent HULAs is $d_{\text{VV}} = \lambda/2$; this entailes the unambiguous elevation range $[-45°, 45°]$.
3) Its shape is not rectangular (the horizontal shift of adjacent HULAs is equal to $\lambda/4$).

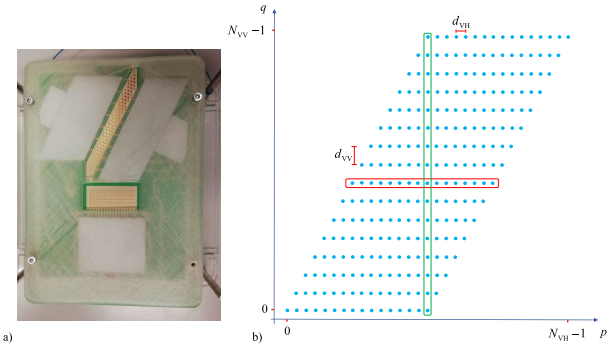

FIGURE 12. Representation of: a) the physical array of the Inras FMCW radar; b) the corresponding virtual array (the red rounded rectangle contains the HULA employed for 2D imaging, whereas the green one the vertical array chosen as a reference for 3D imaging).

This virtual array allows us to achieve the same range resolution as the TI FMCW radar, and azimuth and elevation resolutions equal to $\Delta\theta_2 = 7.6°$ and $\Delta\phi_2 = 3.8°$, respectively (see (186)–(187)). In our work, the HULA contained inside the red rectangle appearing in Fig. 12-b) (the whole array) has been exploited for 2D (3D) imaging.

The third device, dubbed **VIC SFCW** radar in the following, is the *Vito-In-Car* radar manufactured by *Vayyar Imaging Ltd Company* [36] (see Fig. 13-a)); it is classified as a *short range radar* (SRR). Its main parameters are: a) initial transmit frequency $f_0 = 78$ GHz; b) frequency spacing $\Delta f = 16.67$ MHz; c) overall number of frequencies $N_f = 121$. Therefore, the bandwidth and the central frequency of the radiated signal are $B_3 = 2.0$ GHz and $f_c = 79$ GHz, respectively. This device is equipped with the URA shown in Fig. 13-a); this is composed by $N_T = 16$ TX antennas and $N_R = 21$ RX antennas, so that an URA of $16 \cdot 21 = 336$ VAs is available, as shown in Fig. 13-b). However, in our work, only $N_{\text{VV}} = 20$ HULAs, each consisting of $N_{\text{HULA}} = 16$ virtual channels characterized by the inter-antenna spacing $d_{\text{VH}} = \lambda/4$, have been exploited; note that the vertical distance between two adjacent HULAs is $d_{\text{VV}} = \lambda/4$. The available array, made of $N_{\text{VV}} = 320$ virtual elements, allows us to achieve a range resolution slightly better that that provided by the TI FMCW radar ($\Delta R_3 = 7.5$ cm; see (185)), and azimuth and elevation resolutions equal to$\Delta\theta_3 = 7.6°$ and $\Delta\phi_3 = 6.0°$, respectively (see (186)–(187)). In our work, the HULA contained inside the red rectangle appearing in Fig. 13-b) (the whole array) has been exploited for 2D (3D) imaging.

Our measurement campaigns have been conducted in a large empty room (whose width, depth and height are 10 m, 8 m and 2.5 m, respectively). Each of the employed radar devices has been mounted on an horizontal wooden bar together with a pico-flexx camera manufactured by *PMD Technologies Inc.* [37] and has been lifted by a tripod at an height of roughly 1.60 m from ground, as shown in Fig. 14. The employed camera is based on a near-infrared *vertical cavity surface emitting laser*, and is able to provide a depth

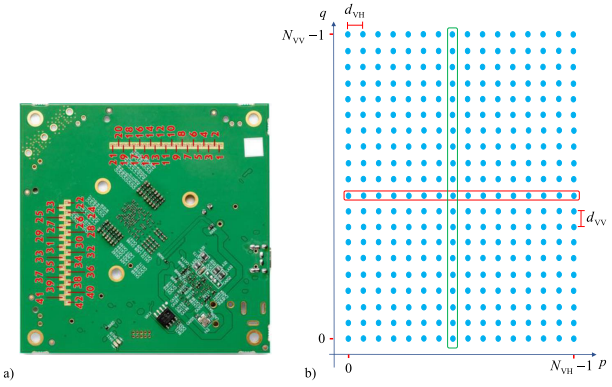

FIGURE 13. Representation of: a) the physical array of the VIC SFCW radar; b) the corresponding virtual array (the red rounded rectangle contains the HULA employed for 2D imaging, whereas the green one the vertical array chosen as a reference for 3D imaging).

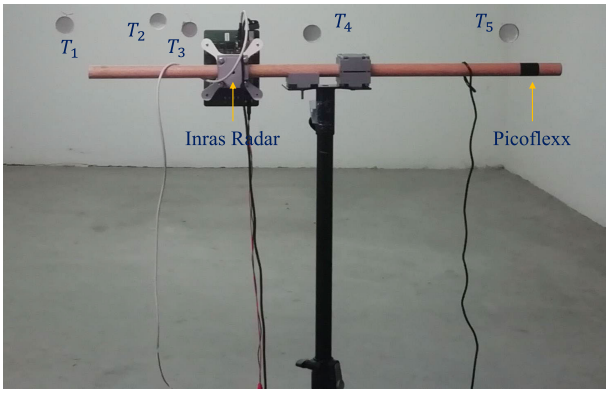

FIGURE 14. Experimental set-up developed for our measurement campaigns. The radar device (the Inras FMCW radar in this case) and a reference sensor (pico-flexx) are mounted on a wooden bar. A group of metal targets, placed at the same height as our sensors, is also visible.

map or, equivalently, a 3D point-cloud of a small region of the observed environment (its maximum depth is equal to 4 m, whereas its *field of view* is $62° \times 45°$).

In each measurement campaign, the experiments have been repeated for all the radar devices exactly in the same conditions. Note that the measurements acquired through the SFCW MIMO radar have been pre-processed by an on-board cancellation algorithm that exploits the measurements acquired from the first transmitted frame to cancel out unwanted received echoes.

It is important to point out that:

a) in all the radar systems, the target ranges have been estimated with respect to the central virtual channel of the employed ULA;
b) the exact target positions have been acquired with respect to the centre of the pico-flexx camera;
c) the data processing has been accomplished in the MATLAB environment;
d) all our detection and estimation algorithms have been run on a desktop computer equipped with a single i7 processor.

2) RANGE AND AMPLITUDE ESTIMATION

In this paragraph, the accuracy of the STDREC algorithm employed by the RPE is analysed for two specific static scenarios. The first scenario is characterized by a single detectable target (a small metal disk[14] having a diameter equal to 5.5 cm) placed in ten different positions. The target range R and azimuth θ have been selected in the interval $[1.0,\ 3.0]$ m, with a step of 0.5 m and $[-40°,\ 40°]$. The range and azimuth of the considered targets are listed in Table 4 for all the employed radar devices (the data referring to the i-th position are collected in the column identified by T_i, with $i = 1, 2, \ldots, 10$). The second scenario, instead, is characterized by the presence of an overall number of targets ranging from 1 to 9 (so that $1 \leq L \leq 9$). The targets are represented by small coins with a diameter of 2 cm; the range and azimuth characterizing their exact positions are listed in Table 5 (the data referring to the i-th target are collected in the column identified by T_i, with $i = 1, 2, \ldots, 9$). Each target has been sequentially added in our scenario; this has allowed us to assess how the performance of the STDREC algorithm is influenced by the value of the parameter L in the presence of *closely spaced targets*.

Prior knowledge of L has been assumed during the processing; moreover, the following values have been selected for the parameters of the STDREC algorithm[15]:

TI FMCW radar - $N = 512$, $M = 4$, $N_0 = N \cdot M = 2048$, $N_{\mathrm{CSFE}} = 5$ and $I = 7$.

Inras FMCW radar - $N = 2048$, $M = 1$, $N_0 = N \cdot M = 2048$, $N_{\mathrm{SFE}} = 5$ and $I = 7$.

VIC SFCW radar - $N = 121$, $M = 16$, $N_0 = N \cdot M = 1936$, $N_{\mathrm{CSDE}} = 5$ and $I = 7$.

Note that: a) the value of the oversampling factor (M) has been selected in way to guarantee approximately the same value of N_0 in all cases, i.e. roughly the same resolution in the spectral analysis of radar signals; b) the values of the parameters N_{SFE}, N_{CSFE} and N_{CSDE} are all equal and large enough so that accurate range estimation is achieved by the STDREC algorithm.

The accuracy of range estimates has been assessed by evaluating the RMSE $\bar{\varepsilon}_R$ and the peak error $\hat{\varepsilon}_R$, expressed by (188)–(189) with $X = R$, $X_i = R_i$ and $\hat{X}_i$. Since the RCS of the considered targets was unknown, our analysis of the complex gains available over the 16 channels of the considered virtual ULA and associated with the same target has concerned only their (unwrapped) phase. The phases $\{\psi^{(v)};\ v = 1, 2, \ldots, 16\}$ estimated by the STDREC algorithm over the considered reference HULA (consisting of 16 VAs; see the red rounded rectangles appearing in Figs. 11-b), 12-b), 13-b)) and associated with a target placed at approximately[16] the

[14]Each target is hung from the ceiling: a nylon thread has been used for suspending it.

[15]Note that in this case the stopping criterion based on eq. (54) has not be employed, since the overall number of targets is known.

[16]The exact range of this target can be found in the T_7 (T_3) column for the TI FMCW and the VIC SFCW radars (Inras FMCW radar) in Table 4.

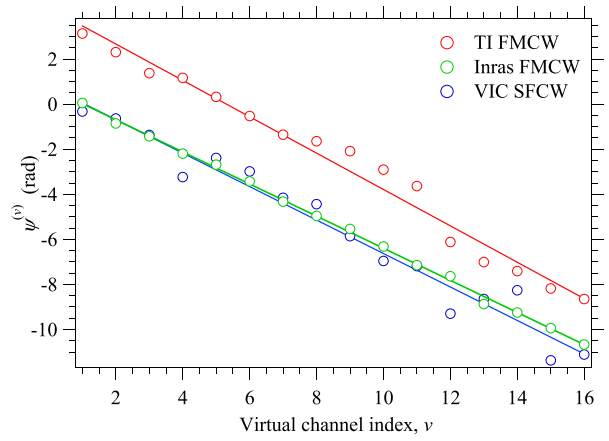

FIGURE 15. Unwrapped phase of the complex gain versus the index of the virtual channel of the reference HULA; a single target is assumed (first experimental scenario). The phase estimates generated by the STDREC algorithm in our three radar systems are identified by red, blue and green circles, whereas straight lines represent their linear fitting.

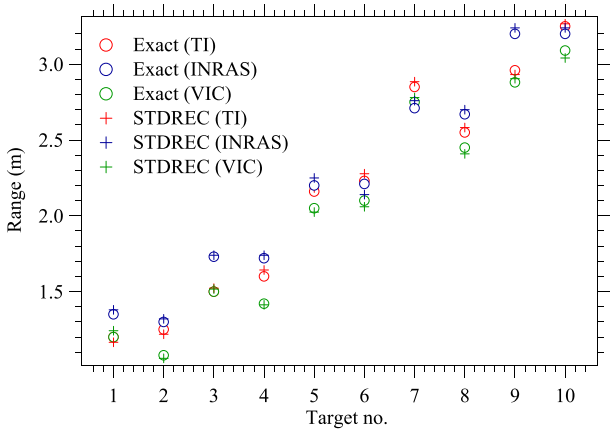

FIGURE 16. Representation of the ranges estimated by the STDREC algorithm (first experimental scenario). All our radar devices are considered.

same azimuth angle with respect to the centre of the radars is shown in Fig. 15. Since the distance d_{VH} between adjacent virtual channels is constant, the (unwrapped) estimated phases exhibit a linear dependence on the index of the virtual channel, as illustrated in Section II (see, in particular, (10) and (11)). Moreover, if a linear fitting is drawn for these data, it should be expected that the slope of the resulting straight line is proportional to $\sin(\theta)$ (see (23) with $\phi = 0$); this is confirmed by the results shown in Fig. 15 for both the FMCW and the SFCW radar systems. To assess the quality of the estimated phases, their RMSE $\bar{\varepsilon}_{\psi}$ has been evaluated in all the scenarios; in doing so, the linear fitting of the 16 phases $\{\psi^{(v)}\}$ has been taken as a reference with respect to which the error of each of them has been computed.

The estimate of the target range generated by the STDREC algorithm for each of the $N_m = 10$ distinct positions considered in the first scenario are listed in Table 4; in the same table, the value of $\bar{\varepsilon}_{\psi}$ computed for each position is also given. The target ranges and their estimates listed in Table 4 are also represented in Fig. 16. The errors $\bar{\varepsilon}_R$ and $\hat{\varepsilon}_R$, the mean of $\bar{\varepsilon}_{\psi}$ (denoted $\bar{\varepsilon}_{m,\psi}$ and generated by taking the average of the N_m values available for $\bar{\varepsilon}_{\psi}$) and the average *computation time* (CT) evaluated on the basis of these results are listed in Table 6.

The results referring to the first scenario lead us to the following conclusions:

1) In all the considered cases, the STDREC is able to accurately estimate the range and the phase characterizing each target.
2) All the values of $\bar{\varepsilon}_R$ and $\hat{\varepsilon}_R$ are comparable, reasonably low and in the order of the resolution of our devices.
3) The range estimates evaluated for the VIC radar are closer to the corresponding exact values when the target range is below 3 m, while the opposite is true for the other two devices; this can be related to the fact that the first device is a SRR, whereas the other two are LRRs
4) The Inras FMCW radar achieves the lowest $\bar{\varepsilon}_{m,\psi}$.
5) The value of $\bar{\varepsilon}_{\psi}$ characterizing the VIC SFWC radar is lower when the target is closer to this device, whereas the opposite occurs in the case of the TI FMCW radar. This result is mainly due to: a) the far-field condition is satisfied for the VIC SFWC device at shorter ranges than for the TI FMCW device, since the antenna array of the former is more compact than that of the latter; b) the VIC SFCW (TI FMCW) radar is a SRR (LRR) system. For these reasons, the measurements provided by the VIC SFCW radar allow us to achieve more accurate results at shorter distances. On the contrary, the higher transmit power radiated by the TI FMCW radar explains why a smaller $\bar{\varepsilon}_{\psi}$ is achieved at larger ranges.
6) The CTs are always in the order of few milliseconds.

Let us focus on the second scenario. In this case, our range estimates have been generated by: a) the STDREC algorithm for all the radar devices; b) the HSTDREC algorithm for the TI FMCW and the VIC SFWC radars; c) the Alg-YA, the Alg-S and the CFH algorithm for the TI FMCW. The obtained results are listed in Table 5. The errors $\bar{\varepsilon}_R$ and $\hat{\varepsilon}_R$, and the CT obtained in this case are listed in Table 7. From these results it can be inferred that:

1) In the case of the TI FMCW radar, all the considered algorithms achieve comparable accuracy. However, the STDREC and the HSTDREC algorithms, unlike all the other algorithms, achieve the lowest RMSE and peak error.
2) The HSTDREC algorithm is not more accurate than the STDREC algorithm; moreover, these algorithms are characterized by similar CTs.
3) The estimated RMSEs and peak errors are in the order of the resolution of our radar devices, but a little bit higher in the Inras FMCW radar systems. This is mainly due to the poorer estimates evaluated for the targets T_8 and T_9, since, in our specific experiment, the energy received from these targets has been found to be lower than that coming from the others. This problem is

TABLE 4. Exact positions (range and azimuth) of the considered target, estimated ranges and RMSEs evaluated for the phase fitting over the considered sixteen virtual channels of each device (first experimental scenario). All our radar devices are taken into consideration.

Method		T_1	T_2	T_3	T_4	T_5	T_6	T_7	T_8	T_9	T_{10}
Exact (TI FMCW)	R (m)	1.2	1.25	1.5	1.6	2.16	2.23	2.85	2.55	2.96	3.25
	θ (°)	-25	40	-10	30	-18	24	-14	21	-18	25
STDREC	$\hat{R}$ (m)	1.166	1.219	1.523	1.643	2.184	2.278	2.885	2.582	2.932	3.267
	$\bar{\varepsilon}_{\psi}$ (rad)	0.8	0.597	0.592	0.5	0.521	0.524	0.576	0.574	0.513	0.506
Exact (Inras FMCW)	R (m)	1.35	1.3	1.73	1.72	2.2	2.1	2.71	2.67	3.2	3.2
	θ (°)	-25	35	-13	30	-5	15	-10	26	-9	20
STDREC	$\hat{R}$ (m)	1.38	1.32	1.74	1.74	2.25	2.14	2.76	2.7	3.24	3.24
	$\bar{\varepsilon}_{\psi}$ (rad)	0.18	0.18	0.2	0.22	0.67	0.79	0.16	0.21	0.16	0.3
Exact (VIC SFCW)	R (m)	1.2	1.08	1.5	1.42	2.05	2.1	2.75	2.45	2.88	3.09
	θ (°)	-35	30	-20	20	-12	15	-14	15	- 18	25
STDREC	$\hat{R}$ (m)	1.242	1.06	1.517	1.413	2.025	2.06	2.78	2.409	2.905	3.041
	$\bar{\varepsilon}_{\psi}$ (rad)	0.25	0.35	0.67	0.345	0.422	0.45	0.686	0.919	0.379	0.54

TABLE 5. Exact ranges of the nine coins characterizing our second experimental scenario. The range estimates evaluated by the Alg-YA, the Alg-S and the STDREC, the HSTDREC and the CFH algorithm are also provided.

Method	T_1 (m)	T_2 (m)	T_3 (m)	T_4 (m)	T_5 (m)	T_6 (m)	T_7 (m)	T_8 (m)	T_9 (m)
Exact	1.860	1.900	1.980	2.110	2.190	2.220	2.370	2.410	2.460
STDREC (TI FMCW)	1.900	1.966	2.015	2.113	2.158	2.242	2.377	2.441	2.516
HSTDREC (TI FMCW)	1.906	1.971	2.016	2.118	2.158	2.238	2.378	2.444	2.514
STDREC (VIC SFCW)	1.837	1.920	1.98	2.081	2.192	2.266	2.355	2.427	2.518
HSTDREC (VIC SFCW)	1.838	1.920	1.976	2.081	2.199	2.265	2.351	2.423	2.530
STDREC (Inras FMCW)	1.920	1.980	2.040	2.100	2.220	2.280	2.460	2.520	2.580
CFH (TI FMCW)	1.947	2.017	2.077	2.161	2.241	2.338	2.374	2.435	2.518
Alg-YA (TI FMCW)	2.022	2.054	2.161	2.257	2.294	2.339	2.416	2.447	2.514
Alg-S (TI FMCW)	2.020	2.142	2.142	2.142	2.153	2.236	2.383	2.433	2.522

not so evident in the case of the TI FMCW and SFCW radars, whose RMSEs and peak errors are very low.

Finally, we would like to stress that the accuracy of STDREC and HSTDREC algorithms can be related to the accuracy of the estimation and cancellation procedure they accomplish. This is exemplified by Fig. 17, where the *initial amplitude spectrum* of the signal received on the central virtual channel of the TI FMCW radar in the second scenario and *its* (weak) *residual*, resulting from the cancellation of the spectral contributions due to the detected targets, are shown. Here, the range and amplitude of the targets estimated by the STDREC (HSTDREC) are also represented by red circles (green crosses).

3) TWO-DIMENSIONAL AND THREE-DIMENSIONAL IMAGING

In this paragraph, the accuracy of the 2D and 3D images generated by the RASCAs is assessed. Two different groups of experiments have been carried out. The first (second) group of experiments has allowed us to assess the performance achieved by the above mentioned algorithm in 2D (3D) imaging. In both cases, the measurements have been acquired in the presence of an increasing number of targets for all our radar devices. In the first group of experiments, the following choices have been made:

TABLE 6. *Root mean square error* $\bar{\varepsilon}_R$*, peak error* $\hat{\varepsilon}_R$*, mean error* $\bar{\varepsilon}_{m,\psi}$ and CT evaluated for the STDREC algorithm in our first experimental scenario.

Method	$\bar{\varepsilon}_R$ (m)	$\hat{\varepsilon}_R$ (m)	$\bar{\varepsilon}_{m,\psi}$ (rad)	CT (msec)
TI FMCW	0.033	0.048	0.570	0.3
VIC SFCW	0.032	0.049	0.501	0.3
INRAS FMCW	0.035	0.050	0.30	0.4

TABLE 7. ***Root mean square error*** $\bar{\varepsilon}_R$***, peak error*** $\hat{\varepsilon}_R$ **and** ***computation time*** **(CT) evaluated in our second experimental scenario.**

Method	$\bar{\varepsilon}_R$ (m)	$\hat{\varepsilon}_R$ (m)	CT (msec)
STDREC (TI FMCW)	0.03	0.07	20
HSTDREC (TI FMCW)	0.03	0.07	20
STDREC (VIC SFCW)	0.03	0.06	15
HSTDREC (VIC SFCW)	0.03	0.07	16
STDREC (Inras FMCW)	0.07	0.10	40
CFH (TI FMCW)	0.07	0.12	15
Alg-YA (TI FMCW)	0.11	0.18	40
Alg-S (TI FMCW)	0.08	0.24	45

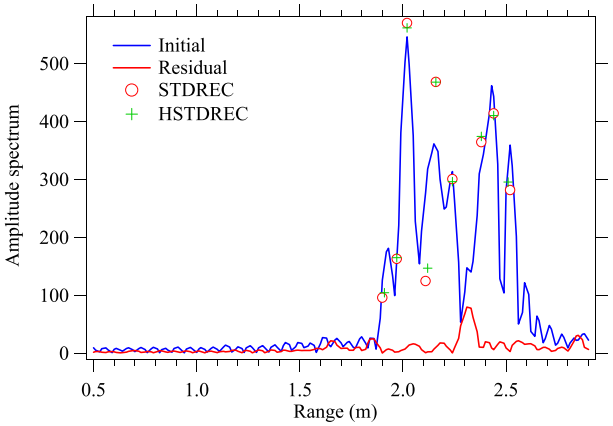

FIGURE 17. **Representation of the initial amplitude spectrum of the signal observed on the central virtual channel (blue line) and of the final *residual* amplitude spectrum generated by the STDREC algorithm (red line). The TI FMCW radar operating in our second experimental scenario is considered; moreover, the target positions estimated by STDREC (HSTDREC) are represented by red circles (green crosses).**

1) The targets have been placed at the same height. Their range and azimuth belong to the intervals [2.2, 2.7] m and $[-15°, 30°]$, respectively (see Table 8).
2) The measurements have been acquired through a virtual ULA, consisting of 16 VAs, in all the considered radar systems.

As far as the second group of experiments is concerned, the following choices have been made:

1) The range, azimuth and elevation of the targets have been selected in the intervals [1.9, 2.8] m, $[-30°, 35°]$ and $[-10°, 10°]$, respectively (see Table 11).
2) The measurements have been acquired through the whole virtual array of each of our radar devices.

The following values have been selected for the parameters of the RASCAs: a) $N_A = 16$ ($N_A = 10$) in the RPE employed in 2D (3D) imaging; b) $N_{\text{CSFE}} = N_{\text{SFE}} = N_{\text{CSDE}} = 5$ in both the STDREC and the STDAEC algorithms; c) the threshold $T_{\text{OF}} = 0$ has been selected in the STDAE-S4 algorithm; d) the values of the parameters N_0 and M are equal to those employed for the STDREC in the previous paragraph; e) the oversampling factor is $\bar{M} = 16$ ($\bar{M} = 7$) for Inras FMCW and VIC SFCW radar (for the TI FMCW), so that the FFT orders are $\bar{N}_0 = 256$ and $\bar{N}_0 = 320$ ($\bar{N}_0 = 602$), respectively. Moreover, the following values have been selected for the parameters[17] of the FFT-BAs and the MUSIC-BAs: $C_s = 6$, $G_s = 6$ and $K_0 = 2$. Prior knowledge of L has been assumed and the threshold T_{STDAEC} has been selected in the range $[0.01, 0.9] \cdot E^{(0)}[l]$ (63) (the value of this threshold has been adjusted on the basis of the SNR characterizing the received signal and the overall number of detectable targets).

The estimates of range and azimuth generated by the RASCAs on the basis of the measurements acquired in our first group of experiments are listed in Table 8, whereas the values of RMSE, peak error and CT computed by averaging the RMSEs, peak errors and CTs evaluated in each single experiment are listed in Table 9. In the last table, the values of RMSE, peak error and CT for the employed FFT-BAs and MUSIC-BAs are also provided. These results lead to the following conclusions:

1) All the range and azimuth errors are comparable with the resolution of our devices.
2) The RASCAs always outperform the other algorithms and require a lower CT.
3) The highest range (azimuth) peak errors and RMSEs are found in the case of the Inras FMCW (VIC SFWC) radar; the TI FMCW radar, instead, achieves the lowest range and azimuth errors. This is mainly due to the differences in the SNR available at the receive side of distinct radar devices is different.

The good accuracy achieved by the RASCAs is also evidenced by Fig. 18, where a *range-azimuth map* [19], generated though standard 2D FFT processing of the measurements acquired through the Inras FMWC radar, is represented as a contour plot[18]; in the same figure, the exact position of the five targets employed in our first group of experiments and their estimates evaluated by all the considered algorithms are shown.

Let us consider now on the results obtained for our second group of experiments. The estimates of range, azimuth and elevation generated by the RASCAs are listed in Table 11, whereas the values of RMSE, peak error and CT evaluated on the basis of this table are listed in Table 10. In the last table, the errors characterizing the FFT-based and MUSIC-based algorithm for 3D imaging are also provided. From these results it can be inferred that:

1) The RMSEs and the peak errors evaluated for target range, azimuth and elevation are reasonably low and comparable with those obtained in the case of 2D imaging. Moreover, these errors are smaller than the ones characterizing the FFT-based and MUSIC-based algorithms.

[17] Our simulations have evidenced that small changes in the value of these parameters do not significantly influence the detection probability and the estimation accuracy of the considered algorithms.

[18] Note that $x - y$ coordinates are employed in this case, in place of range and azimuth; the position of the radar system corresponds to the origin of our reference system.

TABLE 8. Exact range and azimuth of the five targets considered in our first group of experiments and corresponding estimates generated by the RASCAs.

Exp.	Method	Params.	T_1	T_2	T_3	T_4	T_5
	Exact	R (m)	2.26	2.51	2.44	2.68	2.21
		θ (°)	-12.7	-4.5	10.6	18.0	28.3
1)	RASCA-FC2	R (m)		2.52			
		θ (°)		-5.1			
	RASCA-FR2	R (m)		2.6			
		θ (°)		-3.9			
	RASCA-S2	R (m)	2.18				
		θ (°)	-11.8				
2)	RASCA-FC2	R (m)		2.53	2.40		
		θ (°)		-5.2	8.1		
	RASCA-FR2	R (m)		2.6	2.55		
		θ (°)		-4.3	11.3		
	RASCA-S2	R (m)	2.25		2.55		
		θ (°)	-12.8		6.3		
3)	RASCA-FC2	R (m)	2.27	2.53	2.41		
		θ (°)	-14.0	-5.2	9.8		
	RASCA-FR2	R (m)		2.63	2.55		2.33
		θ (°)		-4.3	11.3		28.2
	RASCA-S2	R (m)	2.31		2.54		2.16
		θ (°)	-13.2		7.2		25.5
4)	RASCA-FC2	R (m)	2.32	2.53	2.42		2.26
		θ (°)	-13.7	-5.2	11.2		29.4
	RASCA-FR2	R (m)	2.30	2.64	2.42		2.22
		θ (°)	-12.5	-4.1	11.9		31.2
	RASCA-S2	R (m)	2.31		2.54	2.75	2.16
		θ (°)	-13.2		6.7	17.5	25.5
5)	RASCA-FC2	R (m)	2.31	2.53	2.42	2.56	2.27
		θ (°)	-12.4	-5.2	11.2	17.0	26.3
	RASCA-FR2	R (m)	2.34	2.47	2.39	2.66	2.36
		θ (°)	-17.3	-6.7	8.1	16.4	29.5
	RASCA-S2	R (m)	2.30	2.52	2.53	2.7	2.13
		θ (°)	-12.5	-7.0	4.0	17.1	27.0

TABLE 9. *Root mean square error $\bar{\varepsilon}_X$, peak error $\hat{\varepsilon}_X$,* and *computation time* (CT) evaluated on the basis of our first group of measurements. Target range and azimuth are taken into consideration.

Method	$\bar{\varepsilon}$		$\hat{\varepsilon}$		CT
	R (m)	θ (°)	R (m)	θ (°)	(sec)
RASCA-FC2	0.04	1.2	0.05	1.5	0.3
FFT-FC2	0.06	1.6	0.11	2.8	0.4
MUSIC-FC2	0.05	1.4	0.09	2.4	0.5
RASCA-FR2	0.09	1.1	0.12	1.8	0.4
FFT-FR2	0.13	1.8	0.16	2.65	0.45
MUSIC-FR2	0.13	1.6	0.16	2.49	0.45
RASCA-S2	0.07	2.5	0.09	3.8	0.3
FFT-S2	0.07	3.0	0.09	4.0	0.45
MUSIC-S2	0.06	2.5	0.08	3.5	0.45

2) The range errors evaluated for all the radar devices are comparable; however, the highest (lowest) peak error and RMSE are achieved in the case of the VIC SFCW (TI FMCW) radar.
3) The azimuth and elevation estimates computed on the basis of the measurements acquired through the TI and Inras FMCW radars are reasonably good.
4) The accuracy achieved by the VIC SFCW radar in the estimation of target elevation is better than that in azimuth estimation. This is due to the fact that the URA of this device provides a larger number of channels (i.e., a finer angular resolution) along the vertical direction with respect to the horizontal one.
5) The average CT is in the order of few seconds for all the proposed algorithms; the lowest (highest) average CT is found in the case of the VIC SFCW and the TI FMCW radars (Inras FMCW radar). This is mainly due

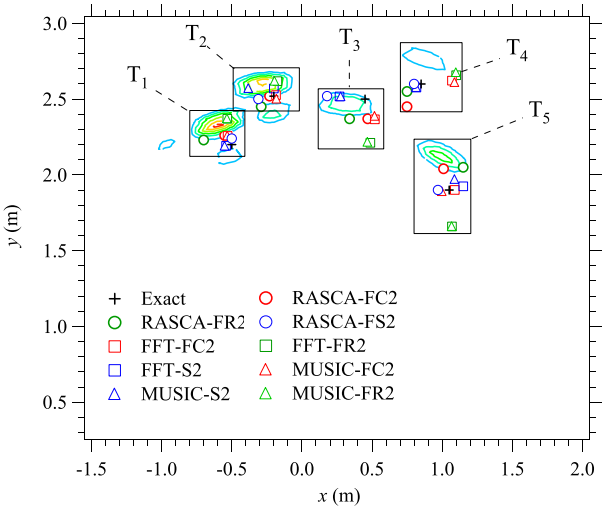

FIGURE 18. Representation of the range-azimuth map (in $x - y$ coordinates) computed on the basis of the measurements acquired through the Inras FMCW radar in the presence of five targets. The exact position of each target and its estimate obtained through the RASCAs (shown in Table 8) and the other algorithms are also shown. The rectangles allow to delimit the region in which the position of each target and its estimates are located.

TABLE 10. *Root mean square error $\bar{\varepsilon}_X$, peak error $\hat{\varepsilon}_X$* and *computation time* (CT) evaluated on the basis of our second group of measurements. Target range, azimuth and elevation are taken into consideration.

Method	$\bar{\varepsilon}$			$\hat{\varepsilon}$			CT
	R (m)	θ (°)	ϕ (°)	R (m)	θ (°)	ϕ (°)	(sec)
RASCA-FC3	0.05	2.8	1.9	0.07	3.9	2.5	2.0
FFT-FC3	0.07	3.0	1.5	0.08	4.2	2.1	1.5
MUSIC-FC3	0.07	3.9	3.2	0.08	6.4	3.8	1.6
RASCA-FR3	0.06	2.0	2.3	0.08	3.0	3.0	2.6
FFT-FR3	0.1	1.0	2.1	0.17	1.5	3.2	1.1
MUSIC-FR3	0.1	1.0	2.2	0.15	1.5	3.3	1.3
RASCA-S3	0.07	5.2	1.7	0.09	5.3	1.8	2.2
FFT-S3	0.08	5.1	2.1	0.11	6.5	2.8	1.0
MUSIC-S3	0.11	5.3	2.1	0.18	6.7	3.1	1.1

TABLE 11. Exact range, azimuth and elevation of the five targets considered in our second group of experiments and corresponding estimates generated by the RASCAs.

Exp.	Method	Params.	T_1	T_2	T_3	T_4	T_5
	Exact	R (m)	1.94	2.34	2.75	2.49	2.08
		θ (°)	-27.8	-9.9	0	14.0	35.2
		ϕ (°)	-6.0	2.0	-2.1	-7.0	-2.0
1)	RASCA-FC3	R (m)	1.89				
		θ (°)	-25.8				
		ϕ (°)	-4.0				
	RASCA-FR3	R (m)	2.04				
		θ (°)	-29.3				
		ϕ (°)	-7.5				
	RASCA-S3	R (m)	1.85				
		θ (°)	-20.9				
		ϕ (°)	-3.5				
2)	RASCA-FC3	R (m)	1.89				2.12
		θ (°)	-25.2				37.8
		ϕ (°)	-3.4				-2.3
	RASCA-FR3	R (m)	2.0				2.1
		θ (°)	-27.0				34.2
		ϕ (°)	-8.0				-2.5
	RASCA-S3	R (m)	1.91				2.05
		θ (°)	-21.0				28.5
		ϕ (°)	-3.5				-1.5
3)	RASCA-FC3	R (m)	1.89	2.43			2.12
		θ (°)	-25.2	-8.6			37.8
		ϕ (°)	-3.4	1.1			-3.4
	RASCA-FR3	R (m)	2.0	2.45			2.1
		θ (°)	-29	-10			31.5
		ϕ (°)	-4.0	5.0			-3.0
	RASCA-S3	R (m)	1.89	2.24			2.1
		θ (°)	-21.0	-9.5			29.2
		ϕ (°)	-4.0	5.0			-3.0
4)	RASCA-FC3	R (m)	1.89	2.44		2.48	2.12
		θ (°)	-25.2	-8.6		20.1	37.3
		ϕ (°)	-3.2	-0.6		-6.9	-2.9
	RASCA-FR3	R (m)	2.0	2.4		2.45	2.1
		θ (°)	-29.5	-12.0		18.3	33.5
		ϕ (°)	-4.0	5.0		5.0	-3.0
	RASCA-S3	R (m)	1.85	2.23		2.60	2.06
		θ (°)	-21	-9		15	29
		ϕ (°)	-3.5	0		-7	-2.5
5)	RASCA-FC3	R (m)	1.89	2.44	2.83	2.48	2.12
		θ (°)	-25.2	-8.6	3.2	20.1	37.3
		ϕ (°)	-3.2	-0.6	-2.87	-6.9	-2.9
	RASCA-FR3	R (m)	1.98	2.4	2.65	2.4	2.13
		θ (°)	-27.6	-15.0	0.4	18.3	37.3
		ϕ (°)	-5.8	5	-1.1	-3	-6.2
	RASCA-S3	R (m)	1.82	2.26	2.82	2.61	2.1
		θ (°)	-21.0	-9.0	2.1	14.6	29.0
		ϕ (°)	-3.5	0	-2.5	-8.2	-1.0

to the fact that the STDREC algorithm employed in the case of the Inras FMCW requires an higher computational effort with respect to its counterpart employed with the TI FMCW and the VIC SFCW radars.

6) In general, the CT of RASCAs is higher than that required by the proposed FFT-based or MUSIC-based methods. This is mainly due to the recursive cancellation procedure that is not employed by the other two methods. However, we believe that this cancellation procedure plays a fundamental role in the detection of weak targets and allows to achieve a good estimation accuracy.

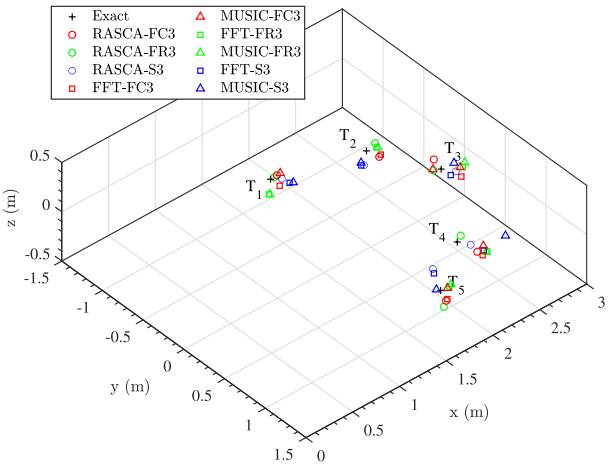

FIGURE 19. Representation of a 3D scenario characterized by five targets. The exact position of each target and the corresponding estimates evaluated by all the considered algorithms are shown (all our radar systems are considered).

The good accuracy and resolution provided by the RASCAs are highlighted by Fig. 19, where the exact positions of the five targets employed in our second group of experiments and their estimates produced by all the considered algorithms are shown; note that, unlike FFT-based and MUSIC-based algorithms, the RASCAs achieve good accuracy even in the presence of closely spaced targets, like T_4 and T_5.

XI. CONCLUSION

In this manuscript, six novel algorithms, dubbed *range & angle serial cancellation algorithms* (RASCAs), have been developed for the detection and the estimation of multiple targets in colocated MIMO radar systems. All these algorithms can be seen as instances of a general approach to target detection and estimation, and exploit new methods for the estimation of multiple overlapped real and complex tones. Moreover, four of them apply to colocated MIMO FMCW radar systems, whereas the other two to colocated MIMO SFCW radar systems. As evidenced by our computer simulations run on both synthetically generated data and measurements acquired through commercial devices, the devised algorithms are able to generate accurate 2D and 3D radar images in the presence of multiple closely spaced targets and outperform other algorithms based on the computation of multiple FFTs or on the MUSIC for DOA estimation.

APPENDIX
COMPUTATIONAL COMPLEXITY

In this Appendix, the computational complexity, in terms of flops, is assessed for the RASCA-FC3 developed

in Paragraph IV. The overall computational cost of this algorithm can be expressed as

$$\mathcal{C}_{\text{FC3}} = N_{\text{VR}}\,\mathcal{C}_{\text{T}_1} + N_A\,K_{\text{T}_2}\,\mathcal{C}_{\text{T}_2} + L_b\,K_{\text{T}_2}\,\mathcal{C}_{\text{T}_3} + \mathcal{C}_{\text{T}_{\text{sc}}}, \quad (191)$$

where $\mathcal{C}_{\text{T}_1}$ is the contribution due to the first task of the RASCA-FC3, K_{T_2} (K_{T_3}) represents the overall number of iterations carried out by the STDREC (STDAEC) algorithm, $\mathcal{C}_{\text{T}_2}$ ($\mathcal{C}_{\text{T}_3}$) is the contribution due to a single iteration of the STDREC (STDAEC) executed on a single VA (on the whole virtual array for a given frequency bin) and $\mathcal{C}_{\text{T}_{\text{sc}}}$ is the contribution due to the computation of the spatial coordinates of the overall image. The general criteria adopted in estimating the computational costs appearing in the RHS of (191) are illustrated in [38] and can be summarised as follows:

- $4d - 2$ flops are required to compute the inner product $\mathbf{u}_c^T\,\mathbf{v}$ of the d-dimensional complex column vector $\mathbf{u}_c$ and the d-dimensional real column vector $\mathbf{v}$;
- $6d + 2(d-1)$ flops are required to compute the inner product $\mathbf{u}_c^T\,\mathbf{v}_c$ of the d-dimensional complex vectors $\mathbf{u}_c$ and $\mathbf{v}_c$;
- d flops are required to find the largest element of d-dimensional real vector $\mathbf{v}$;
- $4d^2 + 14d - 8$ flops are required to compute an interpolation based on the elements of the d-dimensional complex vector $\mathbf{v}$.
- $8d\log_2(d)$ flops are required to compute the FFT of the d -dimensional complex vector $\mathbf{v}$.

The expressions of the computational costs associated with each of the three tasks of the RASCA-FC3 are illustrated below.

$\mathbf{T}_1$ - The cost $\mathcal{C}_{\text{T}_1}$ can be expressed as

$$\mathcal{C}_{\text{T}_1} \triangleq \mathcal{C}_{\mathbf{x}_{k,\text{ZP}}} + \mathcal{C}_{\mathbf{X}_k}, \quad (192)$$

where: a) $\mathcal{C}_{\mathbf{x}_{\text{ZP}}} = 4N$ is the contribution due to the computation of the vectors $\{\mathbf{x}_{k,\text{ZP}}^{(v)};\ k = 0, 1, 2\}$ (see (43)–(45)); b) $\mathcal{C}_{\mathbf{X}} = 24N_0\log_2 N_0$ is the contribution due to the computation of the vectors $\{\mathbf{X}_k^{(v)};\ k = 0, 1, 2\}$ (see (47)).

$\mathbf{T}_2$ - The computational cost of this task is mainly due to its main algorithm, i.e., to the STDREC algorithm. The cost $\mathcal{C}_{\text{T}_2}$ can be expressed as

$$\mathcal{C}_{\text{T}_2} \triangleq \mathcal{C}_{\text{CSFE}} + \mathcal{C}_{\mathbf{C}_{X_k}} + \mathcal{C}_E, \quad (193)$$

where: a) $\mathcal{C}_{\text{CSFE}} = 4N_{\text{CSFE}}I^2$ is the cost originating from the CSFE[19] employed in **STDREC-S1**; b) $\mathcal{C}_{\mathbf{C}_{X_k}} = 18N_0$ is the contribution due to the computation of the vectors $(\mathbf{C}_{X_0}^{(v_k)}[i], \mathbf{C}_{X_1}^{(v_k)}[i], \mathbf{C}_{X_2}^{(v_k)}[i])$ (see (140)–(142)); c) $\mathcal{C}_E = 8N_0 - 2$ is the contribution due to the computation of the residual energy (see (54)).

$\mathbf{T}_3$ - The cost $\mathcal{C}_{\text{T}_3}$ can be expressed as

$$\mathcal{C}_{\text{T}_3} \triangleq \mathcal{C}_{\text{CSFE}_\text{V}} + \mathcal{C}_{\mathbf{X}^{(\text{VF})}} + \mathcal{C}_{\text{CSFE}_\text{H}} + \mathcal{C}_{\mathbf{X}_{\text{OF}}} + \mathcal{C}_{\text{CSFE}_{\text{OF}}} + \mathcal{C}_E, \quad (194)$$

where: a) $\mathcal{C}_{\text{CSFE}_\text{V}} = 8\bar{N}_0\log_2(\bar{N}_0) + 4N_{\text{CSFE}}I^2$ is the cost originating from the CSFE employed in **STDAE-S1**; b) $\mathcal{C}_{\mathbf{X}^{(\text{VF})}} = 6N_{\text{VV}}N_{\text{VH}} + 2N_{\text{VV}}$ is the contribution due to the computation of the vertically folded spectrum $\mathbf{X}_i^{(\text{VF})}[l]$ (76) in **STDAE-S2**; c) $\mathcal{C}_{\text{CSFE}_\text{H}} = 8\bar{N}_0\log_2(\bar{N}_0) + 4N_{\text{CSFE}}I^2$ is the cost originating from the CSFE employed in **STDAE-S3**; d) $\mathcal{C}_{\mathbf{X}_{\text{OF}}} = 6N_{\text{VV}}N_{\text{VH}} + 18N_{\text{VV}}N_{\text{VH}}N_0$ is the contribution due to the computation of the overall folded spectrum $\{\mathbf{X}_{m,\text{OF}}[l];\ m = 0, 1, 2\}$ (see (78) and (83)); e) $\mathcal{C}_{\text{CSFE}_{\text{OF}}} = 4N_{\text{CSFE}}I^2$ is the cost due to the CSFE[20] in **STDAE-S4**; f) $\mathcal{C}_E = 6N_{\text{VV}}N_{\text{VH}}$ is the contribution due to the computation of the residual energy in **STDAEC-S3** (see (63)).

Finally, the cost $\mathcal{C}_{\text{T}_{\text{sc}}} = 5L$ is required to generate the overall point cloud.

Based on the results illustrated above, (191) can be rewritten as

$$\begin{aligned}\mathcal{C}_{\text{FC3}} = {} & N_{\text{VR}}(4N + 24N_0\log_2(N_0)) \\ & + N_{\text{T}_2}(4N_{\text{CSFE}}I^2 + 26N_0 - 2) \\ & + N_{\text{T}_3}(12N_{\text{CSFE}}I^2 + 2N_{\text{VV}} + 18N_{\text{VH}}N_{\text{VV}} \\ & + 18N_{\text{VH}}N_{\text{VV}}N_0 + 16\bar{N}_0\log_2(\bar{N}_0) + 5L, \quad (195)\end{aligned}$$

where $N_{\text{T}_2} \triangleq N_A\,K_{\text{T}_2}$ and $N_{\text{T}_3} \triangleq L_b\,K_{\text{T}_2}$.

ACKNOWLEDGMENT

The author would like to thank the anonymous Reviewers for their constructive comments, that really helped us to improve the quality of this manuscript.

REFERENCES

[1] A. M. Haimovich, R. S. Blum, and L. J. Cimini, "MIMO radar with widely separated antennas," *IEEE Signal Process. Mag.*, vol. 25, no. 1, pp. 116–129, Dec. 2008.
[2] E. Fishler, A. Haimovich, R. Blum, L. Cimini, D. Chizhik, and R. Valenzuela, "Performance of MIMO radar systems: Advantages of angular diversity," in *Proc. 38th Asilomar Conf. Signals, Syst., Comput.*, vol. 1, Nov. 2004, pp. 305–309.
[3] M. A. Richards, *Fundamentals Radar Signal Processing*. New York, NY, USA: McGraw-Hill, 2005.
[4] S. M. Patole, M. Torlak, D. Wang, and M. Ali, "Automotive radars: A review of signal processing techniques," *IEEE Signal Process. Mag.*, vol. 34, no. 2, pp. 22–35, Mar. 2017.
[5] S. Rao, "MIMO radar," Texas Instrum., Dallas, TX, USA, Tech. Rep. SWRA554A, Jul. 2018.
[6] L. Mihaylova, A. Y. Carmi, F. Septier, A. Gning, S. K. Pang, and S. Godsill, "Overview of Bayesian sequential Monte Carlo methods for group and extended object tracking," *Digit. Signal Process.*, vol. 25, pp. 1–16, Feb. 2014.
[7] D. Oh and J. Lee, "Low-complexity range-azimuth FMCW radar sensor using joint angle and delay estimation without SVD and EVD," *IEEE Sensors J.*, vol. 15, no. 9, pp. 4799–4811, Sep. 2015.
[8] J.-J. Lin, Y. Li, W. Hsu, and T. Lee, "Design of an FMCW radar baseband signal processing system for automotive application," *Springer Plus J.*, vol. 5, pp. 1–16, Jan. 2016.
[9] E. Sirignano, A. Davoli, G. M. Vitetta, and F. Viappiani, "A comparative analysis of deterministic detection and estimation techniques for MIMO SFCW radars," *IEEE Access*, vol. 7, pp. 129848–129861, 2019.
[10] P. Di Viesti, A. Davoli, G. Guerzoni, and G. M. Vitetta, "Novel methods for approximate maximum likelihood estimation of multiple superimposed undamped tones and their application to radar systems," Jul. 2021. [Online]. Available: https://www.techrxiv.org/articles/preprint/Novel_Methods_for_Approximate_Maximum_Likelihood_Estimation_of_Multiple_Superimposed_Undamped_Tones_and_Their_Application_to_Radar_Systems/15054321, doi: 10.36227/techrxiv.15054321.

[19]Note that, in this case, the cost of the CSFE does not account for the evaluation of three DFTs, since these have been already evaluated in **T1**.

[20]Note that, in this case, the cost of the CSFE does not account for the evaluation of three DFTs, since these are made available by overall folding.

[11] A. A. Gorji, R. Tharmarasa, W. D. Blair, and T. Kirubarajan, "Multiple unresolved target localization and tracking using colocated MIMO radars," *IEEE Trans. Aerosp. Electron. Syst.*, vol. 48, no. 3, pp. 2498–2517, Jul. 2012.
[12] J. Li and P. Stoica, "MIMO radar with colocated antennas," *IEEE Signal Process. Mag.*, vol. 24, no. 5, pp. 106–114, Sep. 2007.
[13] L. Xu, J. Li, and P. Stoica, "Target detection and parameter estimation for MIMO radar systems," *IEEE Trans. Aerosp. Electron. Syst.*, vol. 44, no. 3, pp. 927–939, Jul. 2008.
[14] S. Zuther, M. Biggel, M. M. Muntzinger, and K. Dietmayer, "Multi-target tracking for merged measurements of automotive narrow-band radar sensors," in *Proc. 12th Int. IEEE Conf. Intell. Transp. Syst.*, Oct. 2009, pp. 1–6.
[15] J. Li and P. Stoica, *MIMO Radar Signal Processing*. Hoboken, NJ, USA: Wiley, 2009.
[16] J. Gamba, *Radar Signal Processing for Autonomous Driving*. Singapore: Springer, 2020.
[17] M. A. Richards, *Fundamentals of Radar Signal Processing*. New York, NY, USA: McGraw-Hill, 2005.
[18] L. L. Scharf and C. Demeure, *Statistical Signal Processing: Detection, Estimation, and Time Series Analysis*. Reading, MA, USA: Addison-Wesley, 1991.
[19] I. Bilik, O. Longman, S. Villeval, and J. Tabrikian, "The rise of radar for autonomous vehicles: Signal processing solutions and future research directions," *IEEE Signal Process. Mag.*, vol. 36, no. 5, pp. 20–31, Sep. 2019.
[20] S. Sun, A. P. Petropulu, and H. V. Poor, "MIMO radar for advanced driver-assistance systems and autonomous driving: Advantages and challenges," *IEEE Signal Process. Mag.*, vol. 37, no. 4, pp. 98–117, Jul. 2020.
[21] I. Ziskind and M. Wax, "Maximum likelihood localization of multiple sources by alternating projection," *IEEE Trans. Acoust., Speech Signal Process.*, vol. 36, no. 10, pp. 1553–1560, Oct. 1988.
[22] A. Serbes and K. Qaraqe, "A fast method for estimating frequencies of multiple sinusoidals," *IEEE Signal Process. Lett.*, vol. 27, pp. 386–390, 2020.
[23] S. Ye and E. Aboutanios, "An algorithm for the parameter estimation of multiple superimposed exponentials in noise," in *Proc. IEEE Int. Conf. Acoust., Speech Signal Process. (ICASSP)*, Apr. 2015, pp. 3457–3461.
[24] S. Ye and E. Aboutanios, "Rapid accurate frequency estimation of multiple resolved exponentials in noise," *Signal Process.*, vol. 132, pp. 29–39, Mar. 2017.
[25] A. Serbes, "Fast and efficient estimation of frequencies," *IEEE Trans. Commun.*, vol. 69, no. 6, pp. 4054–4066, Jun. 2021.
[26] J. Selva, "Efficient wideband DOA estimation through function evaluation techniques," *IEEE Trans. Signal Process.*, vol. 66, no. 12, pp. 3112–3123, Jun. 2018.
[27] C. M. Bishop, *Pattern Recognition Machine Learning* (Information Science and Statistics). New York, NY, USA: Springer, 2006.
[28] O. Simeone, "A very brief introduction to machine learning with applications to communication systems," *IEEE Trans. Cogn. Commun. Netw.*, vol. 4, no. 4, pp. 648–664, Dec. 2018.
[29] N. Shlezinger, R. Fu, and Y. C. Eldar, "Deep soft interference cancellation for MIMO detection," in *Proc. IEEE Int. Conf. Acoust., Speech Signal Process. (ICASSP)*, May 2020, pp. 8881–8885.
[30] C. M. Schmid, S. Schuster, R. Feger, and A. Stelzer, "On the effects of calibration errors and mutual coupling on the beam pattern of an antenna array," *IEEE Trans. Antennas Propag.*, vol. 61, no. 8, pp. 4063–4072, Aug. 2013.
[31] C. M. Schmid, C. Pfeffer, R. Feger, and A. Stelzer, "An FMCW MIMO radar calibration and mutual coupling compensation approach," in *Proc. Eur. Radar Conf.*, Oct. 2013, pp. 13–16.
[32] R. O. Schmidt, "Multiple emitter location and signal parameter estimation," *IEEE Trans. Antennas Propag.*, vol. AP-34, no. 3, pp. 276–280, Mar. 1986.
[33] T.-T. V. Cao, J. Palmer, and P. E. Berry, "False alarm control of CFAR algorithms with experimental bistatic radar data," in *Proc. IEEE Radar Conf.*, Oct. 2010, pp. 156–161.
[34] *Imaging Radar Using Cascaded mmwave Sensor Reference Design-tidep-01012*. Accessed: Dec. 17, 2021. [Online]. Available: https://www.ti.com/tool/TIDEP-01012
[35] *INRAS RadarLog Device*. Accessed: Dec. 17, 2021. [Online]. Available: https://www.inras.at/en/products/radarlog
[36] *Vito-In-Car Radar*. Accessed: Dec. 17, 2021. [Online]. Available: https://vayyar.com/auto/
[37] *CamBoard Pico Flexx*. Accessed: Dec. 17, 2021. [Online]. Available: https://pmdtec.com/picofamily/
[38] G. H. Golub and C. F. Van Loan, *Matrix Computations* (Johns Hopkins Studies in the Mathematical Sciences). Baltimore, MD, USA: Johns Hopkins Univ. Press, 1996.

PASQUALE DI VIESTI (Graduate Student Member, IEEE) received the bachelor's and master's degrees *(cum laude)* in electronic engineering from the University of Modena and Reggio Emilia, Italy, in 2016 and 2018, respectively. He is currently a post-doctoral research fellow with the University of Modena and Reggio Emilia. His main research interests include statistical signal processing and MIMO radars.

ALESSANDRO DAVOLI (Graduate Student Member, IEEE) received the B.S. and M.S. degrees *(cum laude)* in electronic engineering from the University of Modena and Reggio Emilia, Italy, in 2016 and 2018, respectively. He is currently a post-doctoral research fellow with the University of Modena and Reggio Emilia. His main research interests include MIMO radars, with emphasis on the development of novel detection and estimation algorithms for automotive applications.

GIORGIO GUERZONI received the B.S. and M.S. degrees in electronic engineering from the University of Modena and Reggio Emilia, Italy, in 2016 and 2018, respectively, where he is currently pursuing the Ph.D. degree in information and communication technology. His main research interests include MIMO radars and machine learning, with emphasis on the development of novel detection and estimation algorithms.

GIORGIO M. VITETTA (Senior Member, IEEE) received the Dr.Ing. degree *(cum laude)* in electronic engineering and the Ph.D. degree from the University of Pisa, Italy, in 1990 and 1994, respectively. He has been holding the position of a full professor of telecommunications at the University of Modena and Reggio Emilia, since 2001. He has coauthored more than 100 papers published on international journals and the proceedings of international conferences. He has coauthored the book *Wireless Communications: Algorithmic Techniques* (John Wiley, 2013). His main research interests include wireless and wired data communications, localization systems, MIMO radars, and the smart grid. He has served as an Area Editor for the IEEE TRANSACTIONS ON COMMUNICATIONS and an Associate Editor for the IEEE WIRELESS COMMUNICATIONS LETTERS and the IEEE TRANSACTIONS ON WIRELESS COMMUNICATIONS.